ornl

ORNL/CON-253

OAK RIDGE NATIONAL LABORATORY

MARTIN MARIETTA

Laboratory Study of the Dynamic Losses of a Single Speed, Split System Air-to-Air Heat Pump Having Tube and Plate Fin Heat Exchangers

W. A. Miller

OPERATED BY
MARTIN MARIETTA ENERGY SYSTEMS, INC.
FOR THE UNITED STATES
DEPARTMENT OF ENERGY

ORNL/CON--253

DE90 000970

LABORATORY STUDY OF THE DYNAMIC LOSSES OF A SINGLE SPEED, SPLIT SYSTEM AIR-TO-AIR HEAT PUMP HAVING TUBE AND PLATE FIN HEAT EXCHANGERS

W. A. Miller

Energy Division

Date Published: August 1989

Data From: 1985-1986

Prepared by the
OAK RIDGE NATIONAL LABORATORY
Oak Ridge, Tennessee 37831
operated by
MARTIN MARIETTA ENERGY SYSTEMS, INC.
for the
U.S. DEPARTMENT OF ENERGY
under Contract DE-AC05-84OR21400

CONTENTS

CONTENTS (cont.)

CONTENTS (cont.)

LIST OF FIGURES

LIST OF FIGURES (cont.)

LIST OF FIGURES (cont.)

LIST OF FIGURES (cont.)

LIST OF FIGURES (cont.)

LIST OF FIGURES (cont.)

LIST OF TABLES

LIST OF TABLES

ACKNOWLEDGMENTS

My sincere appreciation is given to all those members of the Efficiency and Renewables Research Section of Oak Ridge National Laboratory's Energy Division who assisted in the completion and publication of this report. Special thanks must be given to Ray Ellison, Steve Fischer, C. K. Rice, Don Miller, Gene Holt, John Farmer, and LeRoy Gilliam (Graphics) for their assistance. Special thanks are given Wilbur Allin, Instrumentation and Controls Division, for his design and development of the refrigerant weighing system utilized in the study. Knowledge and wisdom were gleaned from each individual who has helped develop my personal character and professional career.

EXECUTIVE SUMMARY

The frosting, defrosting, and cycling operation of an air-to-air heat pump was investigated in the laboratory. A split-system residential unit of 9.7-kW (2 3/4-ton) capacity was instrumented and tested in environmental chambers for the measurement of the coefficient of performance, capacity, and component efficiencies during both steady state and dynamic operation. In the laboratory, control strategies that reduced defrosting and cycling losses were demonstrated. All test data were reduced and algorithms for calculating dynamic losses were developed and used in seasonal performance calculations for predicting the magnitude of losses and the potential energy and cost savings.

To better understand the physical processes affecting cycling, experiments were conducted with the unit fully instrumented. For these tests the unit held 2.3-kg (5-lb) excess of manufacturer charge [3.4-kg (7.5-lb)]. Additional tests were conducted with manufacturer nameplate charge, and these reduced data were used in seasonal analysis simulations.

The test heat pump operating with nameplate charge and a demand defrost control as compared with a 90-min time-temperature control reduced annual energy consumption by roughly 5% of annual heat pump energy for climates having a heating-load-to-annual-load ratio greater than 0.60.

Seasonal analysis results for various cities throughout the United States revealed the defrosting loss to predominate over frosting losses. Frosting losses are only 1 to 3% of the total annual heat pump energy usage. Results indicated that demand- or time-controlled defrost intervals could possibly be extended at the expense of greater frosting losses in order to lower seasonal losses due to frosting/defrosting, if system reliability would not be compromised.

Seasonal analysis results indicate that the annual operating energy consumed by the test heat pump can be reduced 5 to 6% through use of a restrictor that inhibits the migration of refrigerant when the heat pump cycles off. The no-bleed type restrictor would maintain refrigerant distributions in the condenser and evaporator when the unit was deenergized. At system start-up this temporary holding of the refrigerant in the condenser eliminates the surging of much of the refrigerant from evaporator to the accumulator that contributes to most of the cycling loss.

Sizing of a heat pump to the design cooling load yielded best annual performance factor and maintained building comfort conditions for those climates where cooling load predominated. However, seasonal analysis results indicated that the sizing of a heat pump to cooling design load was inadequate for climates that were predominantly heating load. In such cases, the heat pump was undersized for heating load, thus excess supplemental heat was required to satisfy the building

load. Doubling the size of a hypothetical heat pump from 1.75 tons (sized for cooling load) to 3.5 tons would save the homeowner in Syracuse, New York, roughly $100 a year due to a 67% reduction of back-up heat. Future research is needed to develop sizing criteria that have cooling mode comfort constraints and cost criteria for heat pumps, whether single or variable speed, operating in predominantly heating load climates.

LABORATORY STUDY OF THE DYNAMIC LOSSES OF A SINGLE SPEED, SPLIT SYSTEM AIR-TO-AIR HEAT PUMP HAVING TUBE AND PLATE FIN HEAT EXCHANGERS

W. A. Miller

ABSTRACT

An air-to-air split-system residential heat pump of nominal 9.7-kW (2 3/4-ton) capacity was instrumented and tested in the laboratory. The coefficient of performance, capacity, and component efficiencies were measured during cooling and heating mode steady state and cycling conditions and under frosting and defrosting conditions.

Improvement in cycling COP and capacity was observed by controlling off-cycle refrigerant migration. Best cycling COP and capacity performance occurred for cycling tests conducted with refrigerant isolated in the indoor heat exchanger during the off cycle, coupled with 2 min of extended indoor blower operating during the off-cycle.

The frosting-defrosting experiments were conducted at outdoor ambient temperatures of 4.4, 1.7, and -3.8°C (40, 35, and 25°F) and for discrete humidity levels ranging from 60 through 80%. Frosting and defrosting algorithms were developed from the data for use in seasonal analysis simulations.

Seasonal analysis calculations revealed that the reduction of frosting, defrosting, and cycling losses would result in a 3-year payback of roughly $150 to $300 to the consumer for most climatic regions in the United States.

INTRODUCTION

The dynamic losses of an air-to-air heat pump are caused by frosting and defrosting of the outdoor coil and by cycling operation of the heat pump. Results presented herein are from a series of laboratory experiments aimed at providing detailed characterization of frosting, defrosting, and cycling losses as well as steady state performance data. The work is a continuation of a planned program[1-3] of combined experimental and analytical studies to identify ways to improve heat pump efficiency. The objectives of this study are:

1. to determine the base-case efficiency of the selected heat pump operating under steady state conditions,

2. to measure the degradation of heat pump efficiency due to cycling, frosting, and defrosting losses,

3. to provide detailed system and component performance data usable in understanding dynamic loss processes, and

4. to develop and evaluate methods that could reduce these dynamic losses.

Cycling operation of a vapor compression heat pump results in degradation of the coefficient of performance (COP) and capacity. Cycling is responsible for the major losses in heat pump efficiency, yet detailed information on cycling is sparse. Studies conducted by Kelly and Parken,[4] Tanaka,[5] Mulroy and Didion,[6] and Murphy and Goldschmidt[7] have addressed qualitatively the refrigerant pressure, temperature, and efficiency trends observed during on and off cycling transients. Mulroy investigated the movement of refrigerant within a heat pump system during cooling mode tests with a 6-min-on and 24-min-off cycling rate. Tanaka analyzed the refrigerant dynamics of a heat pump system operating in two different modes: (1) heat pump energized to equilibrium after being off for 16 hours and (2) heat pump energized after previous history of a 60-min-on period and a 10-min-off period.

Frosting lowers the heat flow to the outdoor coil, which in turn degrades system COP and heating capacity. The accumulation of frost on the outdoor heat exchanger increases the resistance to the heat pump because of (1) the reduced airflow across the coil and (2) the insulating affect of the frost. Defrosting was initiated by either demand or time and temperature defrost controls. During the defrost operation the heat pump runs in the cooling mode, which necessitates the use of auxiliary heaters to temper chilled supply air. Both reverse cycle operation and use of resistance heat during defrosting caused degradation of COP.

This report presents an analysis of cycling as a function of heat pump on and off time and outdoor temperature. To better understand the physical processes affecting cycling, experiments were conducted with the unit fully instrumented. For these tests the unit held 2.3-kg (5-lb) excess of manufacturer charge [3.4-kg (7.5-lb)]. Additional tests were conducted with manufacturer nameplate charge, and these reduced data were used in seasonal analysis simulations. Frosting and defrosting are studied as functions of outdoor temperature and relative humidity. These results provide a data base for formulation and validation of analytical models of seasonal performance. The models can then be used to compile recommendations for candidate improvements in heat pump design.

Previous work in the laboratory was conducted on a split-system heat pump that had a one row spine fin outdoor heat exchanger.[3] The previous work was done in bootstrap air loops. The present experiments were conducted on a split-system, air-to-air heat pump having tube and plate fin heat exchangers, and the heat pump was installed in environmental chambers. In addition a refrigerant weighing system was developed to measure the weight of refrigerant in the outdoor unit during cycling operation.

2. CONCLUSIONS AND RESULTS

2.1 STEADY STATE PERFORMANCE

The heat pump tested in these experiments yielded heating- and cooling-mode steady state performance data that agreed well with the rated values published by the Air Conditioning and Refrigeration Institute (ARI). The ARI ratings and observed values of COP and are listed in Table 2.1. The observed heating mode values are from tests conducted at 21°C (70°F) indoor air temperature and 8.3°C (47°F) outdoor air temperature. Cooling mode tests were conducted with 27.8°C (82°F) outdoor air and indoor air conditions of 26.7°C (80°F) dry bulb and 19.4°C (67°F) wet bulb temperature. (See Appendix A for a detailed display of steady state system performance.)

Table 2.1. Observed steady state performance compared with ratings of the Air Conditioning and Refrigeration Institute

Organization	Supply air [m^3/s (cfm)]	Cooling mode		Heating[a] mode	
		Capacity [kW (kBtu/h)]	EER[b]	Capacity [kW (kBtu/h)]	COP[b]
ARI rating	1275 (36)	34.0 (9.9)	7.4	38.0 (11.1)	3.0
ORNL data	1275 (36)	34.2 (10.0)	7.8	35.0 (10.3)	3.0

[a]Outdoor dry bulb 8.3°C (47°F).

[b]EER, energy efficiency ratio; COP, coefficient of performance.

2.2 CYCLING LOSSES

The loss in heat pump efficiency due to on and off cycling is caused by a gradual rather than a step change in capacity at start-up. Seasonal analysis results have shown the portion of energy consumed during cycling operation, including off-cycle parasitics, is roughly 10% of the total annual heat pump operating energy. This loss in efficiency is due mainly to the migration of refrigerant from the high pressure side to the low pressure side when the heat pump cycles off. Upon start-up the compressor pumps this migrated refrigerant from the evaporator into the accumulator. With most of the refrigerant now in the accumulator rather than where it is needed in the heat exchangers, the heat exchangers become starved for refrigerant. Thus the time delay incurred to reestablish proper charge distribution in the condenser and evaporator at start-up results in most of the cycling loss.

The cycling efficiency of the test heat pump improved by control of the migration of refrigerant with swing-out ball valves. By simulating a no-bleed restrictor during cycling operation, the energy consumed by cycling operation was reduced roughly 5 to 6% of total annual heat pump operating energy. At the start of the on cycle, the majority of the refrigerant was already in the condenser because the ball valves inhibited migration of any refrigerant during the off cycle. Therefore the accumulator did not fill with refrigerant at start-up, the time required to establish proper charge distribution was less, and the heat pump reached steady state capacity more rapidly as compared with cycling tests of off-cycle refrigerant migration.

Cycling losses were shown to be directly related to the total refrigerant charge. The annual energy consumed by the test heat pump operating in Knoxville, Tennessee, with 2.3 kg (5 lb) of refrigerant overcharge, was increased by 7% over that consumed when operating with the nameplate charge of 3.4 kg (7.5 lb). Steady state capacity was reached within 5 min of compressor operation when the heat pump operated with the nameplate charge. However, with 5.7 kg (12.5 lb) of refrigerant charge the unit did not achieve steady state capacity until after 10 min of compressor operation. The larger mass of refrigerant increased the time required to establish proper charge distribution, and the result was an increase in energy consumed during cycling operation.

2.3 FROSTING OF THE OUTDOOR HEAT EXCHANGER

Frosting and defrosting tests conducted at 4.4, 1.7, and -3.8°C (40, 35, and 25°F) outdoor air temperatures for relative humidities ranging from 60 through 80% revealed little degradation in COP and capacity due to frosting of the tube and plate fin outdoor heat exchanger. The portion of energy attributed to frosting operation was no more than 3% of the total heat pump annual operating energy for the various climates investigated in this report.

Frost-defrost tests conducted at 1.7°C (35°F) outdoor air temperature and 80% relative humidity incurred only a 5% drop in average COP and integrated capacity over the 50-min frosting interval. Demand defrost controls then initiated the defrost cycle, because the air pressure drop across the outdoor coil was greater than 0.13 kPa (0.51 in. of water). The outdoor coil, although heavily laden with frost, was still able to maintain evaporator load. As a result, evaporator pressure and, therefore, density of refrigerant entering the compressor remained fairly constant over the 50-min frosting interval. These trends in turn caused only slight degradations in COP and capacity.

The above frosting trends for the test heat pump were much different than those previously observed for another heat pump with a one row spine fin outdoor heat exchanger. However, the differing efficiencies of the two heat pumps observed under frosting conditions are due primarily to the differing strengths of the outdoor fan motors. The outdoor fan of the test heat pump was able to draw 1180 liter/s (2500 cfm)

against 0.08-kPa pressure drop (0.30 in. of water), while the outdoor fan of the previously tested heat pump drew 1322 liter/s (2800 cfm) against 0.02 kPa (0.09 in. of water).

Seasonal analysis conducted for both heat pumps operating in Knoxville, Tennessee, revealed no more than 4% increase in annual operating energy due to frosting of either unit. However, the above comparison does reveal the need for future research in heat exchanger design and fan characteristics that would minimize frost accumulation, which has been proven to minimize seasonal defrost losses.

2.4 DEFROSTING LOSSES AND DEFROST CONTROLS

Demand as compared with time and temperature defrosting yielded the best annual performance for the test heat pump operating in the various climates investigated in this report. The demand defrost initiator improved system reliability by decreasing the defrost frequency during dry winter operation. It also protected the compressor by initiating defrost prior to severe frost buildup that occurred for outdoor ambient temperatures of 1.7 and -1.1°C (35 and 30°F) with relative humidities greater than 70%. The time and temperature defrost initiators, based on 90- and 45-min timed cycles, are unable to compensate for these various winter conditions.

The energy consumed during defrosting for the cities investigated (Table 2.2) increased as the control was changed from a demand control to a 45-min time and temperature control. Demand defrost simulations for Knoxville used 2.2% of the total annual operating energy, while the 45-min time temperature control caused defrost energy usage to increase to 11%. Similar results were seen for the more severe winter climates of Washington, D.C., and Syracuse, New York. These results again reveal the advantage of the demand defrost control. These seasonal analysis results also show the frosting-defrosting degradation to be due primarily to defrosting. Thus, demand- or time-controlled defrost intervals could be extended at the expense of greater frosting losses to lower combined frosting-defrosting seasonal losses.

Qualitative analysis of the defrost cycle revealed similar trends to cycling transients. During the defrost cycle a time lag is required to pump refrigerant from the accumulator, which protects the compressor but causes a delay in completing the defrost operation. At the start of the defrosting cycle, refrigerant in the indoor coil is pumped by the compressor and temporarily held in the accumulator. Negligible flow occurs across the indoor throttle, and the indoor coil becomes starved for refrigerant. The compressor power and the refrigerant mass flowrate drop; little defrosting is accomplished during the first 2 min of the defrosting cycle. As refrigerant is metered through the oil-return hole (at bottom of the U-tube within the accumulator), the compressor is able to supply the heat required to defrost the outdoor coil. Results indicate that the efficiency of the defrost cycle could be improved through

Table 2.2. Frosting and defrosting energy expressed as a percentage of total annual heat pump operating energy

Location	Defrost control[a]	Ratio of heating load to annual load	Frosting[b] (% of total)	Defrosting (% of total)	Total annual energy[c] (kWh)
Knoxville, Tenn.	demand	0.58	1.26	2.2	9,337.9
	90 min		1.16	6.9	9,799.4
	45 min		1.27	11.2	10,299.7
Washington, D. C.	demand	0.67	1.04	2.2	10,499.9
	90 min		1.35	7.8	11,173.8
	45 min		1.83	12.6	11,870.7
Syracuse, N. Y.	demand	0.84	2.47	3.69	15,411.9
	90 min		1.98	10.14	16,456.5
	45 min		1.74	16.41	17,668.2

[a]Demand defrost initiated by air pressure drop across the outdoor coil. Time-temperature defrost initiated by table specified time and liquid line temperature.

[b]Frosting includes recovery following defrost plus auxiliary heat used due to effect of frost on heat pump balance point.

[c]Heat pump yearly energy consumption includes back-up heat required to meet building load.

alteration of the defrost refrigerant circuit by use of a controllable indoor throttling device or bypass of the indoor throttle.

2.5 SEASONAL ANALYSIS FOR THE TEST HEAT PUMP

Annual operating energy for the test heat pump can be reduced 5 to 6% through use of a restrictor that prevents refrigerant migration when the heat pump cycles off (Table 2.3). An energy savings ($100 over a 3-year-period) through use of the no-bleed restrictor indicates that improvements in heat pump cycling efficiency can be met.

Seasonal analysis results also indicated that the test heat pump with a demand defrost control provided the best seasonal efficiency while still maintaining system reliability under severe frosting conditions. The energy savings for demand defrost as compared with a 90-min time-temperature defrost for the various cities listed in Table 2.2 was roughly 5% of the annual operating heat pump energy. For those climates having predominantly cooling loads, the use of a demand defrost control

Table 2.3. Payback for improvements in control of test heat pump dynamic operation

City and State	Cooling design factor[a]	Ratio of heating load[b] to annual load	Premium for 3-year payback ($)	
			demand defrost control	No-bleed restrictor
Fort Worth, Tex.	1.14	0.32	38	99
Atlanta, Ga.	1.41	0.51	63	105
Knoxville, Tenn.	1.43	0.58	76	86
Washington, D.C.	1.32	0.67	120	116
Portland, Ore.	1.43	0.76	62	90
Chicago, Ill.	1.44	0.83	165	113
Syracuse, N.Y.	1.65	0.84	198	87
Cheyenne, Wyo.	1.69	0.85	167	77

[a]Ratio of steady state capacity to ASHRAE design cooling load calculated at the 97.5% design day temperature.

[b]Loads calculated using U.S. Air Force Engineering Weather Data Base applied to 167-m^2 (1800-ft^2) ranch style house with HUD minimum insulation.

yielded only marginal cost savings. The test heat pump with demand defrost, operating in climates with predominantly heating load such as Chicago, Syracuse, and Cheyenne (Table 2.3), have roughly an $175 energy cost reduction over a 3-year period. Although payback for improved defrost control is not favorable for all U.S. cities investigated, the use of the demand defrost control yielded best seasonal performance across the country. The demand defrost control would also provide better system reliability as compared with that of time and temperature controls.

2.6 HEAT PUMP SIZING CRITERIA

By general practice a heat pump is sized to the cooling load. No set sizing criteria for heat pumps are established; however, the ASHRAE Equipment Handbook[8] does imply that the heat pump should be sized to the cooling load of the building.

Seasonal analysis simulations were made for the test heat pump scaled over a range of sizes which met minimum cooling load requirements for an 167-m^2 (1800-ft^2) ranch style house that had Department of Housing and Urban Development (HUD) minimum insulation. Maximum Annual Performance Factor (APF) occurred when the heat pump was sized to the

design cooling load for those climates of cities listed in Table 2.3 with a heating-load-to-annual-load ratio less than 0.60. However, for those North American climates with heating-load-to-annual-load ratios greater than 0.60, these sizing criteria resulted in the minimum APF. This result occurred because of the large seasonal heating load and the resulting supplemental heat required to satisfy the house heating load. For example, supplemental heat energy consumption was 20% of the total annual operating energy for the 9.7-kW (2 3/4-ton) test heat pump in Syracuse, New York. The total yearly operating energy for the test heat pump sized to the design cooling load (1.75 ton) for Syracuse, New York, was 10% greater than the yearly heat pump energy usage for the test unit sized to twice the cooling design load (3.5 ton). By doubling the size of the unit cooling capacity, the homeowner in Syracuse, New York, would save $104 per year due to a 67% reduction of supplemental heat. However, doubling the size of the unit roughly doubles the initial cost, which would increase payback of investment. Also the oversized cooling capacity can cause excessive cycling, which results in uncomfortable temperature and humidity levels. A heat pump having continuous or step-change capacity modulation would be an alternative solution for heat pump applications in predominantly heating load climates. In the heating season the unit would reduce back-up heat use by overspeeding the compressor. In the cooling mode, the near constant operation of the compressor would improve humidity control as compared with a single-speed unit.

3. EXPERIMENTAL FACILITY

3.1 THE TEST HEAT PUMP

The unit selected for the dynamic loss experiments was a split-system air-to-air heat pump. The refrigerant circuit of the heat pump was of conventional design except for a liquid-line-to-suction-line heat exchanger that was active only during heating mode operation and that heated the refrigerant just before its entry into the compressor housing. Liquid refrigerant was throttled by capillary tubes during both cooling and heating modes of operation. Both indoor and outdoor heat exchangers were of tube and plate fin construction. The indoor heat exchanger was an A-frame coil with a distributor that metered refrigerant between the two parallel heat exchanger circuits. The salient features of this heat pump are listed in Table 3.1.

The heat pump also had a suction line accumulator to protect the compressor against any sudden return of liquid refrigerant through the suction line. The accumulator temporarily stored the liquid refrigerant and metered it back to the compressor through an orifice located at the bottom of the U-tube within the accumulator. This orifice also served to return oil pumped out of the compressor due to foaming action of refrigerant and oil at start-up. A second orifice, located at top of the U-tube, served as a venturi to ensure that, at start-up, liquid within the U-tube was mixed with vapor within the accumulator to avoid compressor slugging.

Defrosting of the heat pump was initiated by a demand defrost sensor. If total pressure drop through the outdoor coil exceeded 0.13 kPa (0.51 in. of water), the four-way reversing valve was energized to provide reverse cycle defrosting (cooling mode) and the outdoor fan deenergized. Defrosting terminated when the liquid-line temperature leaving the outdoor heat exchanger exceeded 24°C (75°F) or after 11 min, whichever occurred first.

The heat pump was instrumented at the various locations shown in Fig. 3.1 for the measurement of refrigerant temperature, pressure, and flowrate. The description of each measurement, correlated to Fig. 3.1, is listed in Table 3.2.

Modifications were made to the electrical circuit of the heat pump for separate measurements of power supplied to the indoor blower motor, outdoor fan motor, and compressor motor. The indoor blower motor and compressor motor are three-phase, 3-wire induction motors having Y-connected stator windings. Power was supplied to these motors by an independent power source with a constant 60-Hz, 220-V ac, three-phase sinusoidal waveform.

The tested heat pump was controlled either manually or automatically through a data acquisition and control system.

Table 3.1. Features of the tested heat pump

Feature	Description
Refrigerant	R-22 (chlorodifluoromethane)
Compressor	Capacity, 10.7 kW (36,500 Btu/h)[a] Displacement, 59.6 cm^3 (3.64 $in.^3$) 3 ϕ, 3-wire "Y" connected motor Hermetically sealed Variable speed (850-5175 rpm) Drive frequency (15-90 Hz)
Outdoor heat exchanger	Aluminum plate fin, 13 fins per in., with 9.4-mm (0.37-in.) inner diameter copper tubing Three rows deep with three parallel refrigerant circuits 0.61-m^2 (6.6-ft^2) face area
Outdoor fan	Three-blade propeller 0.51-m (20-in.) diameter, 1/3-hp motor Direct drive, two-speed fan High speed: 1.23 m^3/s (2600 cfm) Low speed, 0.85 m^3/s (1800 cfm)
Indoor heat exchanger	Aluminum plate fin, 14 fins per in., with 9.4-mm (0.37-in.) inner diameter copper tubing Four rows deep with three parallel refrigerant circuits 0.45 m^2 (4.64 ft^2) face area
Indoor fan	Centrifugal, 0.25 m (10 in.) diameter by 0.2-m (8-in.) width Direct drive 3 ϕ, 3-wire "Y" connected motor 1/3-hp motor
Controls	Indoor capillary: 914.4-mm (36-in.) length, 2-mm (0.08-in.) bore Outdoor capillary: 939.8-mm (37-in.) length, 2.5-mm (0.10-in) bore Demand defrost control: 0.11 kPa (0.43 in. of water) across outdoor coil Four-way reversing valve (energized in cooling mode)

[a]Rated at 48.8°C (120°F) condenser, 7.2°C (45°F) evaporator; 21.1°C (70°F) suction; 8.3C° (15F°) subcooling.

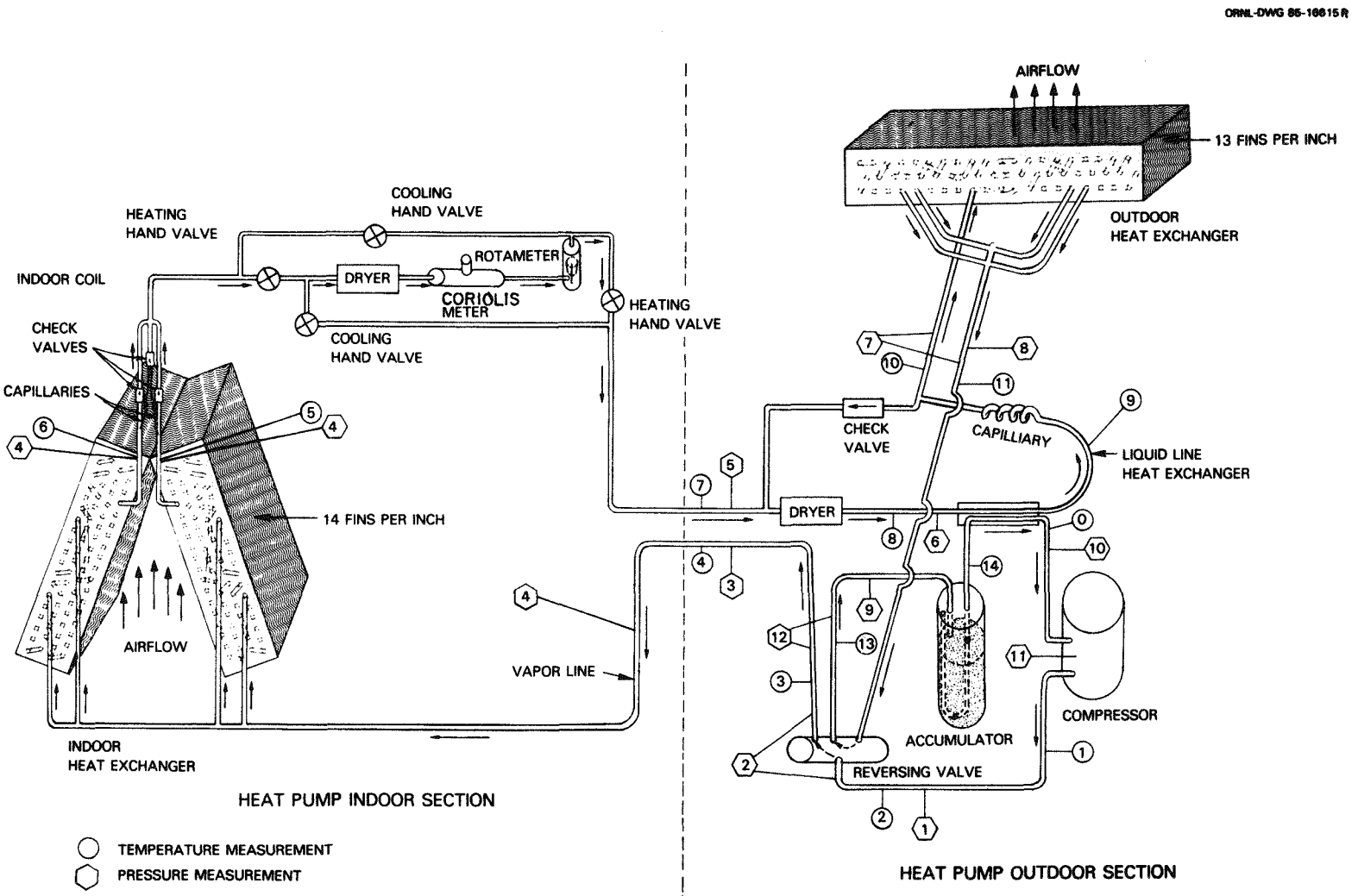

Fig. 3.1. Heat pump refrigerant sensor locations.

Table 3.2. Temperature, pressure, and flow measurements on the refrigerant circuit

Sensor		Description of data taken
Temperature	0	Compressor suction line
	1	Compressor discharge line
	2	Upstream reversing valve on discharge line
	3	Reversing valve vapor line
	4	Indoor heat exchanger vapor line
	5	Indoor throttle
	6	Indoor throttle
	7	Indoor heat exchanger liquid line
	8	Entering liquid/vapor heat exchanger
	9	Entering outdoor throttle
	10	Downstream outdoor throttle
	11	Outdoor heat exchanger unit
	12	Between outdoor heat exchanger and reversing valve
	13	Between reversing valve and accumulator
	14	Between accumulator and liquid/vapor heat exchanger
Pressure	1	Compressor discharge
	2	Between pressure drop and reversing valve
	3	Indoor heat exchanger vapor line
	4	Pressure drop across indoor heat exchanger
	5	Indoor heat exchanger liquid line
	6	Upstream liquid/vapor heat exchanger
	7	Pressure drop across outdoor heat exchanger
	8	Between outdoor heat exchanger and reversing valve
	9	Inlet to accumulator
	10	Compressor suction
	11	Compressor housing
	12	Pressure drop across reversing valve (cooling mode)
Rotameter		Refrigerant volume flow
Coriolis flowmeter		Refrigerant mass flow

3.2 ENVIRONMENTAL CHAMBERS

The split-system air-to-air heat pump used in the study was installed in environmental chambers (Fig. 3.2). Each chamber was capable of controlling both the dry bulb and dew point temperature. The range and accuracy of dry bulb and dew point temperature control for both chambers operating under a 3-ton load are listed in Table 3.3.

Table 3.3. Chamber temperature control ranges and accuracies

Chamber	Dry bulb °C (°F)		Dew point °C (°F)	
	Range	Tolerance	Range	Tolerance
Outdoor	-12 to 38 (10 to 100)	±1 (±2)	-15 to 32 (5 to 90)	±1 (±2)
Indoor	5 to 38 (40 to 100)	±1 (±2)	-4 to 32 (25 to 90)	±1 (±2)

Chamber air was conditioned by a vapor compression refrigeration system and also by resistance heaters. The refrigeration unit was a water-cooled condensing unit that incorporated a hot gas bypass for modulating compressor capacity. Once the chamber cooling load was met, a thermal-electric expansion device in the refrigeration circuit of the chamber was deenergized, causing compressor suction pressure to drop to a level that activated hot gas bypass. A portion of the discharge gas from the compressor bypassed the condenser and was redirected just downstream of the evaporator coil. The hot discharge gas was desuperheated prior to entering the accumulator by mixing with refrigerant throttled from the liquid line. The bypassing of condenser and evaporator allowed the compressor to idle and also maintained evaporator pressure, which will decrease the evaporator response time when cooling is again required.

Moisture was added to the chamber air when needed by injecting steam into the chamber airstream downstream of the evaporator. When required, selica-gel beds, with an automatic regenerative feature, removed moisture from the chambers and expelled the moisture to the surrounding environment.

3.3 DATA ACQUISITION SYSTEM

A PDP-11 host computer and data acquisition system (DAS) was used to monitor all temperatures, pressures, power levels, flows, and refrigerant weight measurements. The computer has a disk based, real-time

PHOTO 6572-84

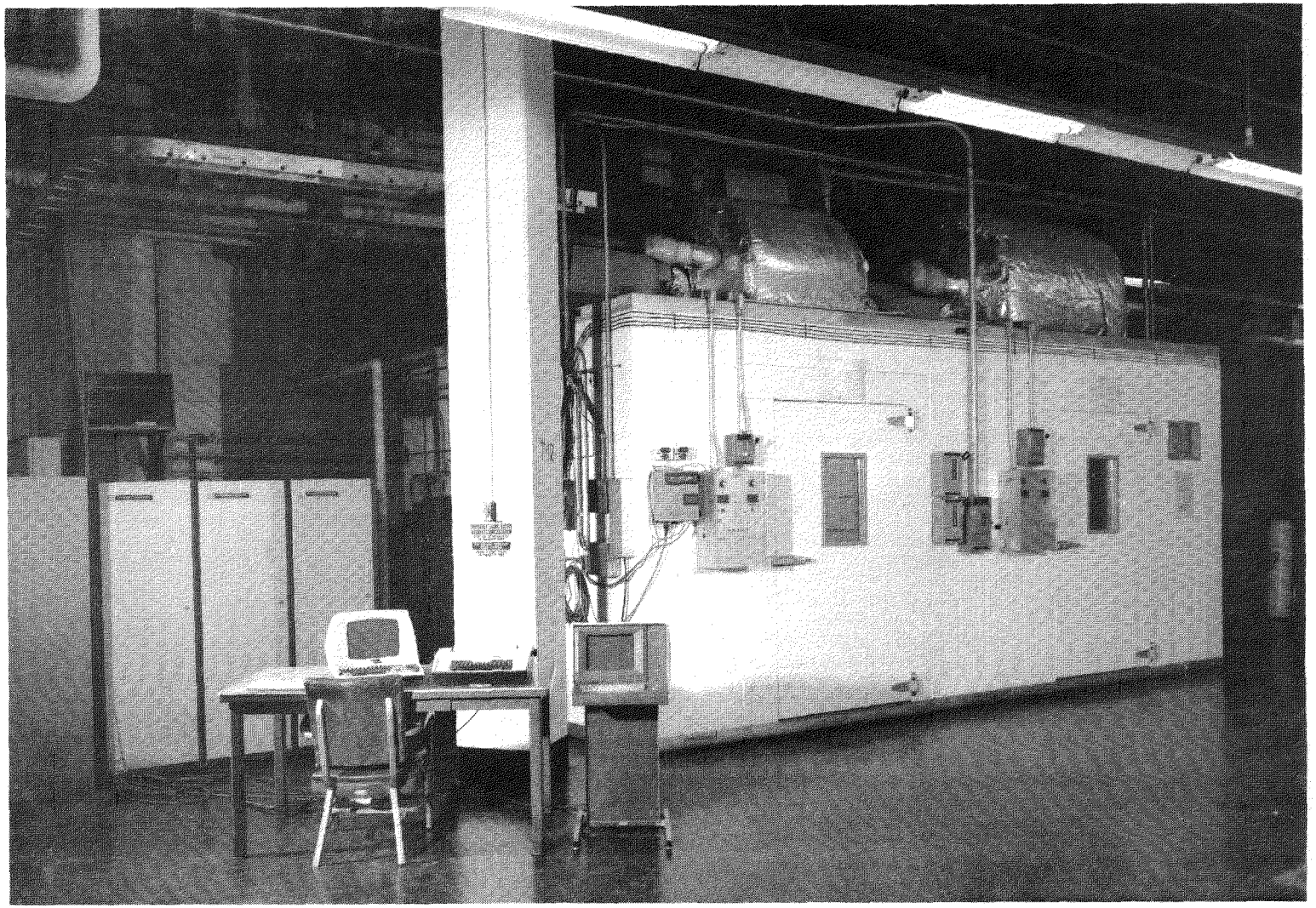

Fig. 3.2. Environmental chambers and data acquisition system.

operating system that provides an environment for the development and execution of multiple real-time tasks. Tasks are written in FORTRAN-77 computer language, which was modified locally to facilitate data acquisition. The DAS provides random access sampling and digitizing of up to 512 analog input signals in 13 program-selectable ranges. Input channels can be randomly sampled at rates of up to 200 samples per second under complete program control of the PDP-11. The DAS has provisions for the following types of inputs and outputs:

1. 3-wire resistance temperature detector (RTD) inputs,
2. digital and analog input and output,
3. thermocouple inputs to floating junction box having thermocouple to copper connectors,
4. frequency counter with user selectable time bases,
5. change of state interrupts that signal the host computer of a user preset condition,
6. isolated ac outputs using silicon controlled rectifier to output 115-V ac,
7. relay output contact closures, and
8. isolated ac and dc inputs.

3.4 INSTRUMENTATION

3.4.1 Airflow

Indoor and outdoor airflows were measured using ducted multipoint pitot tube averaging traverses. Total and static pressure taps were positioned in the duct system in accordance with Air Moving and Conditioning Association, Inc., Standard 210-67.[9] The averaging traverse was symmetrically arranged so that each pressure tap sensed air pressure over an equivalent area within the duct. A parallel cell, honeycomb grid was positioned upstream the multipoint pitot tube traverse for changing turbulent airflow into laminar airflow. The honeycomb grid eliminated the need for long straight runs of duct, which are usually required for accurate flow measurement, before and after the pitot tube traverse.

The average velocity pressure (the difference between the total pressure and the static pressure) was input to a differential pressure cell that output a proportional analog signal to the DAS. The velocity pressure was used in the following equation for calculation of indoor

airflow:

$$Q = -22.96A + 1132.4 \frac{\Delta P^{1/2}}{\rho} A ,$$

where Q = volumetric airflow (cfm),

A = duct cross-sectional area (ft^2),

ΔP = velocity pressure (in. of water),

ρ = density of air (lb/ft^3).

The equation was developed through calibrations of the multipoint pitot tube traverse using a laminar airflow meter as a standard. Accuracy of the indoor airflow device as compared to the standard is displayed in Fig. 3.3. Results showed the standard error of fit to the calibration standard to be $\pm$-0.35 m^3 /min ($\pm$12.5 cfm) over the range of tested airflow.

The airflow traverse device for outdoor airflow measurement was only checked in situ because of the excellent agreement between manufacturer's data and the calibration data observed with the indoor airflow device.

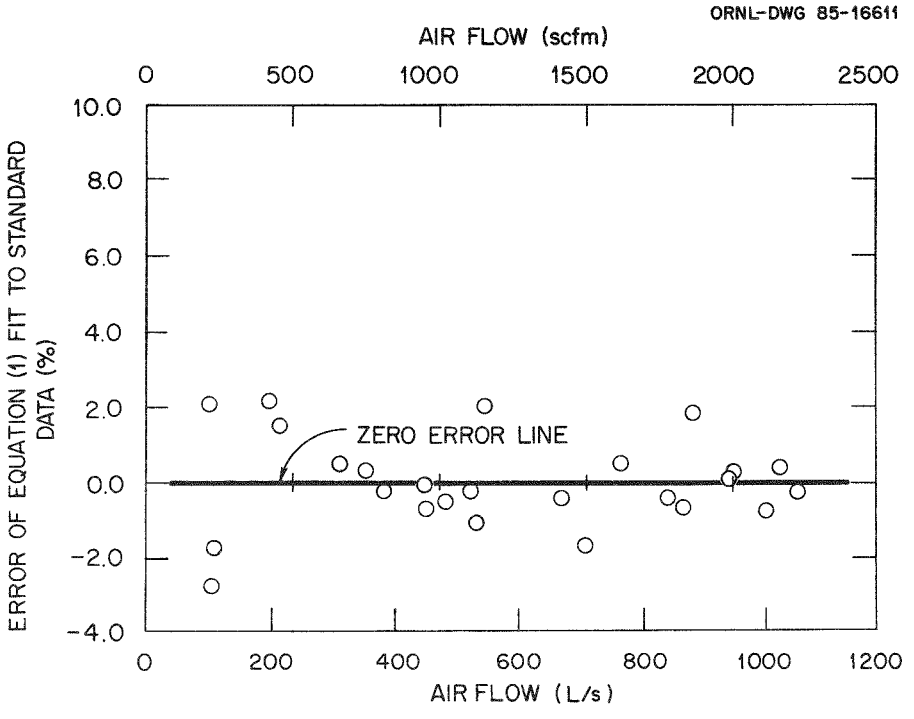

Fig. 3.3. Multipoint Pitot tube calibration data for indoor airflow.

3.4.2 Refrigerant Flowrate

Single-phase refrigerant flowrate was measured in the liquid line using a gyroscopic mass flow meter that was mounted to reduce surrounding vibrations. A variable-area rotameter was placed in series to the mass flow meter for visual checks of accuracy of measurements.

The gyroscopic mass flow meter measured the mass flowrate of subcooled refrigerant passing through the flow tube by detecting the coriolis force associated with the moving refrigerant. A moment, due to this coriolis force, caused an angular deflection of the flow tube about its central axis. This angular deflection was directly proportional to mass flow through the tube and was independent of density and viscosity effects.

The gyroscopic meter was able to accurately measure subcooled refrigerant mass flow; however, the meter was unable to measure two-phase slug flow typically observed in the liquid line during start-up of the heat pump. The accuracy of the flow meter was observed to be ±0.5% of reading for mass flowrates of water ranging from 45 to 272 kg/h (100 to 600 lb/h).

3.4.3 Temperature

The heat pump was instrumented with thermal ribbon platinum RTDs for measuring both heat exchanger wall temperature and refrigerant circuit temperatures. Each RTD was connected to a bridge output network through a 3-wire shielded cable. The 3-wire bridge connector allowed measurement of differential voltage that was proportional to RTD resistance.

The cable leads from the RTD were cut to equal lengths to ensure that lead resistances in opposite legs of the bridge network would cancel. Any discrepancies in lead length resistance and any nonlinear relationship between RTD resistance change and bridge output voltage were corrected by calibrating individual RTDs. Each RTD was immersed in an oil bath that was maintained at various temperature levels. Oil bath temperature was measured with National Bureau of Standards traceable precision thermometers. All RTDs were observed to have accuracies of 0.3°C (±0.5°F) for calibration temperatures ranging from -4 to 99°C (25 to 210°F). The response time of these RTDs was measured to be approximately 5 s for a 12°C (30°F) step change in temperature.

Inlet and exit air temperatures through the indoor unit were measured using thermopile grids comprised of 30 junctions connected in a series combination of 24-AWG copper-constantan wire. Thermopiles sensing average air temperature and average temperature difference were stationed upstream and downstream of the indoor unit. A thermopile sensing average temperature difference was installed across the outdoor coil. Floating reference junctions, previously described by Domingorena, were used for measurement of all thermopile temperatures.[1,2]

A comparison was made between the thermopiles measuring average inlet and exit indoor air temperatures and the thermopile measuring average temperature difference across the indoor unit. Results plotted in Fig. 3.4 show the temperature difference thermopile to be within 1.3% of temperature difference calculated, using the two averaging thermopiles. The thermopiles were constructed of 24-AWG copper-constantan wire because of its rapid response time of 2.5 s for an 8 C° (15 F°) step change in temperature of still air.

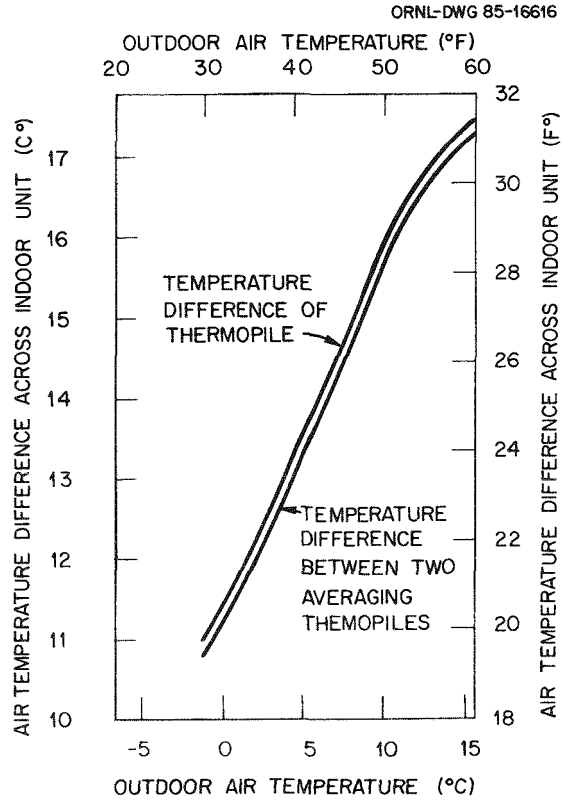

Fig. 3.4. Air temperature measurement comparison between two measuring techniques.

3.4.4 Pressure

The velocity pressure through the multipoint pitot tube airflow device and total pressure drop through the outdoor coil (usable for defrost initiator) were measured using variable inductance differential pressure transducers. These transducers have a diaphragm of magnetically permeable stainless steel. Embedded in each block on opposite sides of the diaphragm is an induction coil. The change in inductance in each coil is directly proportional to deflection of the diaphragm and is designed to be linear with applied differential pressure. This change

in inductance is aopnified and rectified through an ac bridge circuit and is monitored by the DAS as an analog signal for calculation of differential pressure.

These variable inductance cells were selected for measurement of low range [from 0 to 0.55 kPa (0 to 0.28 inches of water)] differential pressures. Accuracy of the transducers, determined by calibration with a micromanometer as a standard, was ±0.8% or better.

Refrigerant pressures were measured using bellows-actuated force-balance transducers. The pressure being measured was applied to the inside of a bellows that was enclosed in a capsule. The pressure exerted a force within the bellows and was balanced by an opposing force transmitted through a force bar linkage. The movement of the force bar resulted in a minute movement of a detector armature, which applied a current to a feedback coil. This current was also output to the DAS and was directly proportional to absolute pressure.

These force-actuated transducers were selected because of their proven performance in a study[10] conducted by the Instrumentation and Controls Division of Oak Ridge National Laboratory. The study revealed that the force-actuated cells were the best overall transducers in terms of hysteresis, linearity, temperature effects, noise generation, over-pressure effects, transient response, and zero drift. The accuracy of the refrigerant pressure transducers was observed to be ±1% of reading for pressures input by a dead weight test standard.

3.4.5 Electrical Power

Single-element and three-element watt transducers were used to measure the power consumption of the outdoor fan, indoor blower, and compressor. These transducers utilize electronic multiplier circuits that sample voltage, current, and power factor for measurement of true power. Both input voltage and current were isolated and ratioed down by precision transformers. The voltage signal was pulse-width modulated and was used to switch the current signal. This switching action produced a pulse train whose average value was proportional to true power. Calibrations conducted on the power transducers have shown them to be accurate to within ±2% of readings observed from a Weston Watthour meter.

3.4.6 Humidity

Moisture content of air in the environmental chambers was measured using dew point hygrometers that measure true dew point temperature. The sensors had thermoelectrically cooled mirrors that produce condensation that was optically detected and automatically controlled for indication of dew point temperature. A precision RTD was embedded within the mirror for measurement of the dew point temperature.

As dew formed on the mirror, less direct light from a light-emitting-diode was reflected from the mirror. A photodetector sensed the change in reflectance and compensated a bridge output that was used to control the direct current to the thermoelectric cooler. As condensate continued to form, less current was directed to the cooling element and the bridge output was driven to its balance point. A rate feedback loop was employed to ensure fast response so that the sensor quickly stabilized to a condition where water vapor condensed from the airstream sample onto the mirror.

The dew point hygrometer is a fundamental method for measuring water vapor. Accuracy of the device as certified through calibrations by the vendor is ±0.1°C (±0.5°F) over long-term usage. The response time of the hygrometer was affected by cooling and heating of the mirror, air sample flowrate, sample line length to the sensor, and the absolute value of dew point being measured. Response time of the sensor is typically 1.6 C° (3 F°) per second; however, sampling line lengths used in these experiments increased the time response to roughly 1.6 C° (3 F°) per 10 seconds.

3.4.7 Refrigerant Weighing System

The migration of refrigerant entering or leaving the outdoor unit was measured using a weighing system that is depicted in Fig. 3.5. The outdoor unit was suspended and counterbalanced through a beam mounted on a flexural pivot as shown in Fig. 3.5. A load cell was mounted on the pivoting beam and engaged a fixed micrometer.

Fine adjustments of the micrometer against the load cell were made to ensure that the counterweight would offset the weight of the outdoor unit without a refrigerant charge. Compensations for the downward thrusts of the outdoor fan were made by calibrating the weighing system with the outdoor fan off and with it operating at high and low speeds. Results of the calibrations reveal the effect of the outdoor fan thrust (Fig. 3.6). Vertical thrusts due to pressure in the liquid line and vapor line were eliminated by using flexible connections to the outdoor unit.

The refrigerant weighing system was designed so that its natural frequency of oscillation was higher than the frequency observed during weighing operation. Vibrations caused by the outdoor fan and compressor were damped both mechanically and electrically. The weighing system was designed so that the load cell was not directly connected to measured weight and therefore vibrations were not directly transmitted to the load cell. This design enabled some damping to occur in the aircraft wire rope cable used to suspend the outdoor unit. Isolation mounts, installed at the base of the weighing system, were also used to minimize any external disturbances. Finally, induced noise was filtered electrically by a low-pass filter that time averaged and damped the signal output from the indicator used in conjunction with the load cell. The time

ORNL--PHOTO 7015--83A

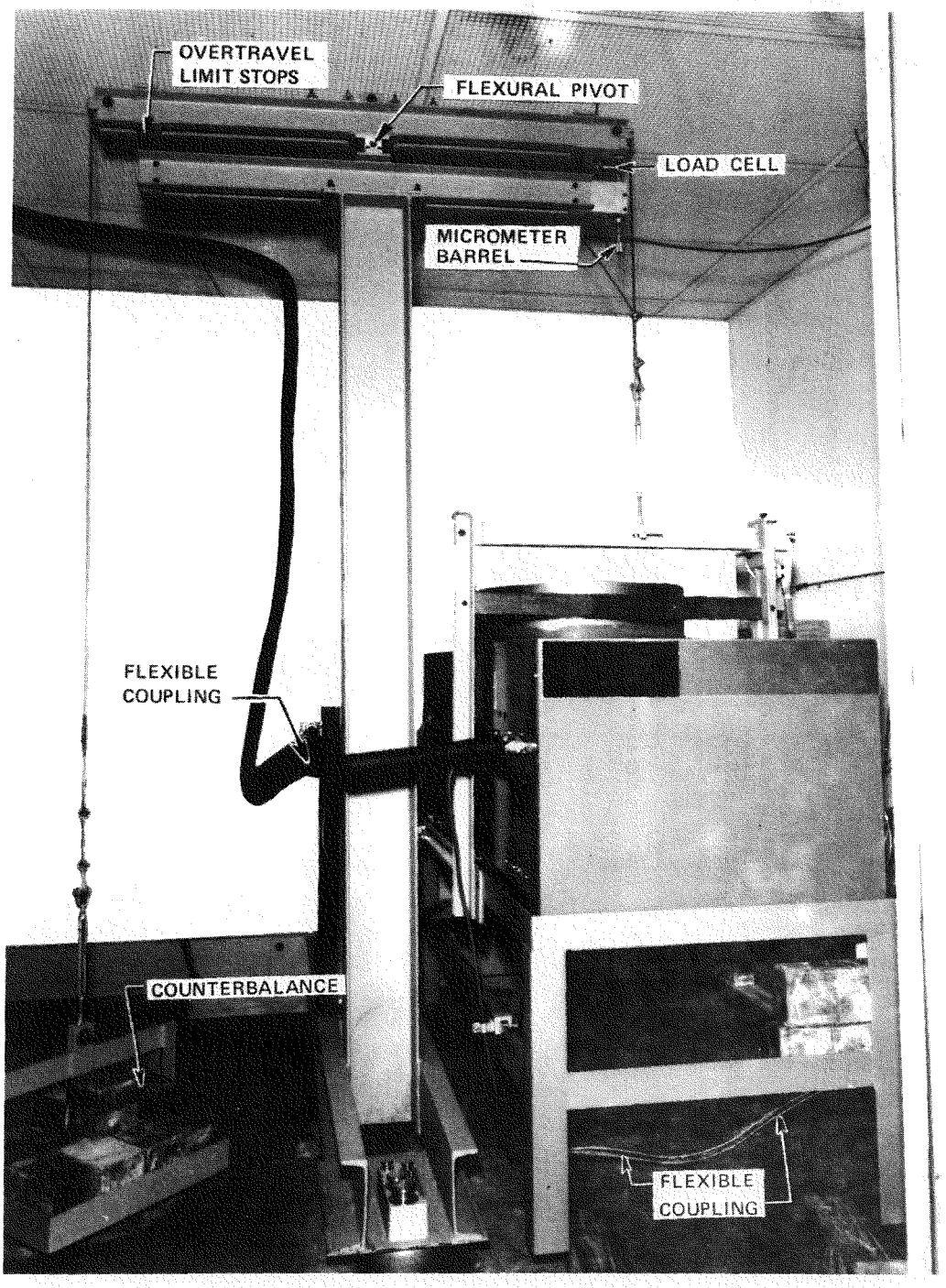

Fig. 3.5. Weighing system for measurement of refrigerant weight in the outdoor unit.

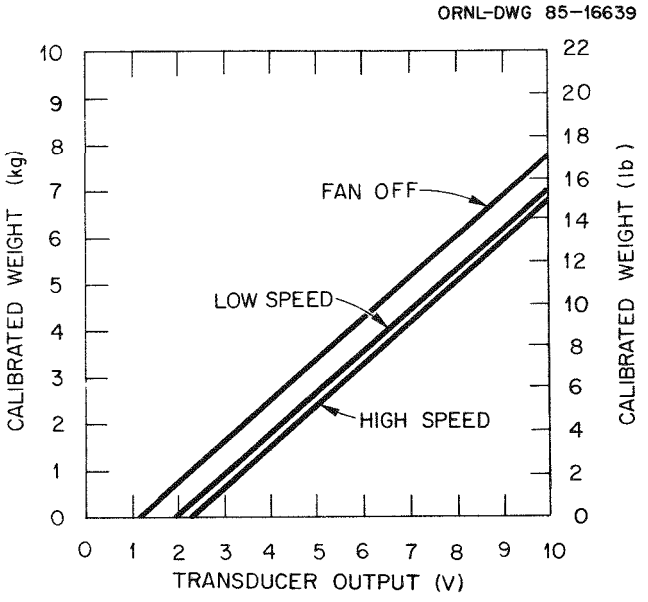

Fig. 3.6. Refrigerant weight scale calibration.

averaged signal was then monitored by the DAS for calculation of refrigerant weight.

Accuracy of the weighing system was checked while the heat pump operated in heating mode by adding precision weights to the outdoor unit, and accuracy was found to be 0.05 kg (±0.1 lb) of reading. Time response with the low-pass filter was approximately 20 s, when the weighing system was subjected to a 1-kg (2.2-lb) step change in weight.

4. EXPERIMENTAL PROCEDURE

4.1 STEADY STATE TESTS

The heat pump was operated for 2 hours inside the controlled ambient temperature and humidity conditions of the environmental chambers prior to steady state data collection. Temperatures and pressures in the refrigerant circuit, power consumption, and capacity of the heat pump were monitored for observation of established heat pump steady state operation. On command, the DAS and host computer then monitored refrigerant-side and air-side data at 10-s intervals for one-half hour to calculate the average COP and capacity. Calculated values of heating mode COP and capacity based on air-side measurements were within 3% of those based on refrigerant-side measurements.

The latent-heat portion of cooling mode capacity was calculated by using indoor unit inlet and exit psychrometric state points and also by measuring the condensate flowrate from the indoor coil. Performance calculations based on air-side cooling mode measurements were within 8% of those based on refrigerant-side measurements. Tests conducted under both heating mode and cooling mode steady state conditions are listed in Table 4.1.

Table 4.1. Steady state tests conducted in the environmental chambers

Test	Heat pump mode	Ambient Temperature °C (°F)	
		Indoor	Outdoor
Steady state	Heating	21.1 (70)	-6.7 (20)
			-3.8 (25)
			1.6 (35)
			4.4 (40)
			10.0 (50)
			15.5 (60)
	Cooling[a]	27.7 (82)	21.1 (70)
			27.7 (82)
			35.0 (95)

[a]Indoor wet bulb 19.4°C (67°F).

4.2 CYCLING TESTS

A series of cycling tests, listed in Table 4.2, were conducted by varying one of three parameters (on time, off time, or outdoor temperature) while holding the other two parameters fixed. The temperature and

Table 4.2. Cycling tests conducted in the environmental chamber

Test	Heat pump mode	Cycling rate		Outdoor temperature °C (°F)
		On-time min	Off-time min	
Cycling	Heating[a]	2,8,16,50	10,30	-1.1 (30) 10.0 (50)
	Cooling[b]	4,10,40,80	20,60	27.7 (82) 35.0 (95)

[a]Indoor dry bulb 21.1°C (70°F).

[b]Indoor wet bulb controlled to ensure no condensation on indoor coil. Dry bulb 27.7°C (82°F).

humidity of the environmental chambers were controlled to ensure sensible (dry coil) heat transfer for both indoor and outdoor heat exchangers. Control of the heat pump and data collection was performed automatically by the DAS and PDP-11 host computer system. Selections of heat pump on time, off time, cooling or heating mode, continuous indoor blower, and off-cycle refrigerant migration control were made interactively at the start of each cycling test. Repetitive cycling operation of the heat pump was established by automatically cycling the heat pump through three on and off cycles prior to data collection. The host computer collected and stored data on three to four cycles of heat pump operation and then cycled either on or off and allowed to establish equilibrium conditions.

Heat pump data were monitored at preset time intervals in each on- and off-period of a given cycle. During each on- and off-period, the scan rate was automatically adjusted according to the severity of the time-dependent transients. Heat exchanger wall temperatures, compressor housing temperatures, refrigerant pressures, and weight of the refrigerant in the outdoor unit were monitored for observation of system response in reaching steady state conditions.

Cycling tests were conducted in the following modes of operation:

1. Continuous indoor blower operation with compressor and outdoor fan cycling on and off,

2. Compressor, indoor blower, and outdoor fan cycling on and off simultaneously (termed normal cycling operation),

3. Indoor blower operation extended part way through the off cycle with compressor and outdoor fan cycling on and off,

4. Refrigerant isolated in indoor coil during off cycle with system operating in normal cycling mode,* and

5. Off-cycle refrigerant isolation in the indoor coil and extended indoor blower operation with compressor and outdoor fan cycling on and off.

This series of heating mode cycling tests were conducted at 10°C (50°F) outdoor temperature to observe any potential improvements in cycling efficiency.

4.3 FROSTING-DEFROSTING TESTS

Frosting and defrosting tests, listed in Table 4.3, were performed to observe the affect of relative humidity and outdoor temperature on heat pump COP and capacity. The control of the heat pump and data collection was performed automatically by the DAS and PDP-11 host computer system. Airflow across the outdoor coil was also monitored by the DAS. Induced air pressure drops through ducting from the outdoor fan to an airflow measuring device dictated the use of a booster fan. This fan was placed in series to the propeller fan of the outdoor unit and was automatically controlled by the DAS and host computer to ensure free-flow conditions across the outdoor unit.

Table 4.3. Frosting and defrosting recovery tests conducted in the environmental chamber

Outdoor ambient		Defrost initiator	
Dry bulb °C (°F)	Relative humidity (%)	Demand	Time and temp.[a] (min)
4.4 (40)	60,70,80	$\Delta P_{outdoor\ coil}$	90,45
1.6 (35)	60,70,80	$\Delta P_{outdoor\ coil}$	90,45
-3.8 (25)	60,70,80	$\Delta P_{outdoor\ coil}$	90,45

[a]Temperature initiator set for 3.8°C (39°F) on liquid line.

A defrost cycle was initiated following each frosting interval by use of differing defrost initiation schemes. A demand defrost logic, based on the total air pressure drop through the outdoor coil, was used to start the defrost cycle on command by the DAS. A time-temperature logic was also tested for comparison of frosting and defrosting losses

*Compressor, indoor blower, and outdoor fan cycle off during cycle.

as a function of defrost control. Following the defrost cycle, the heat pump was allowed to recover and the time required to achieve steady state operation was recorded, as were the refrigerant temperatures and pressures.

Heat pump frosting data, similar to cycling test data, were monitored at preset intervals into the frosting, defrosting, and recovery cycles. During the frosting and defrost cycles the scan rate was automatically adjusted according to the severity of the time-dependent transients. Upon completion of the test, heat pump data were recorded and stored by the PDP-11 host computer for further reduction and analysis.

4.4 UNCERTAINTY ANALYSIS OF COLLECTED DATA

An analysis of collected data was conducted to determine the experimental uncertainty of all measurements. (Since the true value of a given measurement is not directly known, it is more accurate to speak of experimental uncertainty rather than experimental error.) The calculation of uncertainty in measurement was presented by Kline and McClintock,[11] and this uncertainty in measurement is composed of two parts, random error and systematic error.

The random error of a measurement is typified in Fig. 4.1 by the distribution of the measurement population, about the true average. The scatter of data about this average is termed the precision of measurement, which can be represented by the standard deviation about the true average. Random errors are the result of fluctuations in the measuring instrumentation and also in the tested apparatus (i.e., heat pump).

The systematic or fixed error is characterized in Fig. 4.1 as a bias from the true value. This error will cause repeated readings to be inaccurate by roughly the same amount. Systematic errors can be minimized by calibrating a particular instrument to a given test standard. In this case there is little difference between the true value and the true average; therefore the uncertainty analysis would be based on a

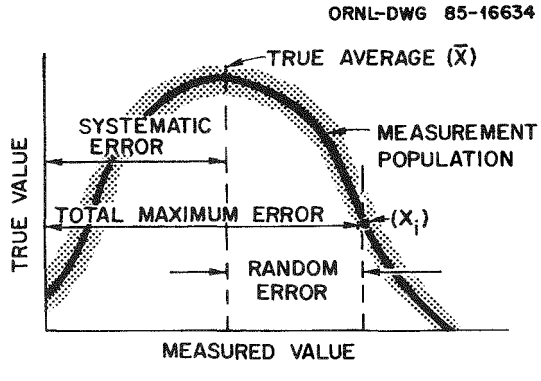

Fig. 4.1. Measurement errors.

statistical analysis of random error. However, when a combination of calibrated and uncalibrated instruments is used in an experiment, it is best to include both random and systematic error analysis.

If an experiment is carefully set up to minimize systematic error, then the uncertainty of measurement is given by

$$U_{random} = [(\frac{\partial R}{\partial X_1}\sigma 1)^2 + (\frac{\partial R}{\partial X_2}\sigma 2)^2 + \cdots, + (\frac{\partial R}{\partial X_N}\sigma N)^2\ ]^{1/2}\ , \qquad (1)$$

where

U_{random} = uncertainty of result due to random error,

X_i = measured independent variable,

σ_i = standard deviation about population average of X_i,

R = dependent variable.

The inclusion of systematic error in the above uncertainty interval requires estimating uncertainties in *each* variable. The estimates are not pure guesses, rather they are derived from calibration data or from in situ comparisons with another instrument and are used in the following equation:

$$U_{systematic} = [(\frac{\partial R}{\partial X_1}U_1)^2 + (\frac{\partial R}{\partial X_2}U_2)^2 + \cdots + (\frac{\partial R}{\partial X_N}U_N)^2]^{1/2}\ , \qquad (2)$$

where

$U_{systematic}$ = uncertainty of result due to systematic error,

U_i = best estimate of uncertainty in measured independent variable.

The total maximum uncertainty of a measurement is then the sum of uncertainties from Eqs. (1) and (2). However, a more realistic estimate of uncertainty, assuming some canceling of errors is as follows:

$$U_{overall} = [U_{systematic})^2 + [U_{random})^2]^{1/2}\ , \qquad (3)$$

where $U_{overall}$ = total probable uncertainty of the result.

This root mean square estimate of overall uncertainty was utilized in the test for uncertainty calculations of reduced data derived from measurements taken from both calibrated and uncalibrated instruments.

Assuming a normal distribution of data as seen in Fig. 4.1, the probability of all values falling within the uncertainty interval is approximated by the Gauss-Laplace normal distribution relation.[12] For

the normal distribution, to double the standard deviation about the population average implies that 95.46% of data will fall within the uncertainty interval. Thus plotted data within this report are represented by error bars having the following connotation:

$$\bar{X} \pm U \text{ (ODDS)} , \tag{4}$$

where

$\bar{X}$ = mean of given measurement population,

U = uncertainty interval equivalent to double the standard deviation estimate,

ODDS = 95.46% confidence that the true value falls within the given uncertainty interval.

5. EXPERIMENTAL RESULTS: HEATING

The COP and the heating capacity characterize the efficiency of a heat pump. These quantities are affected by the air temperature, frosting, and defrosting of the outdoor coil and also by the cycling rate of the heat pump. System efficiency will be examined to seek an understanding of the steady state operation of a heat pump as well as of dynamic operation observed during cycling and frosting and defrosting transients.

5.1 STEADY STATE EFFICIENCY

Steady state COP, heating capacity, and outdoor coil capacity under dry coil conditions were observed to vary linearly with outdoor ambient temperature (Fig. 5.1). The air-side measurement of COP at 15.5°C (60°F) outdoor temperature was 3.3 and the measured air-side heating capacity was 12.3 kW (42.0 kBtu/h). At the lower ambient temperature of -6.7°C (20°F), the COP and capacity were 2.23 and 6.4 kW (21.8 kBtu/h),

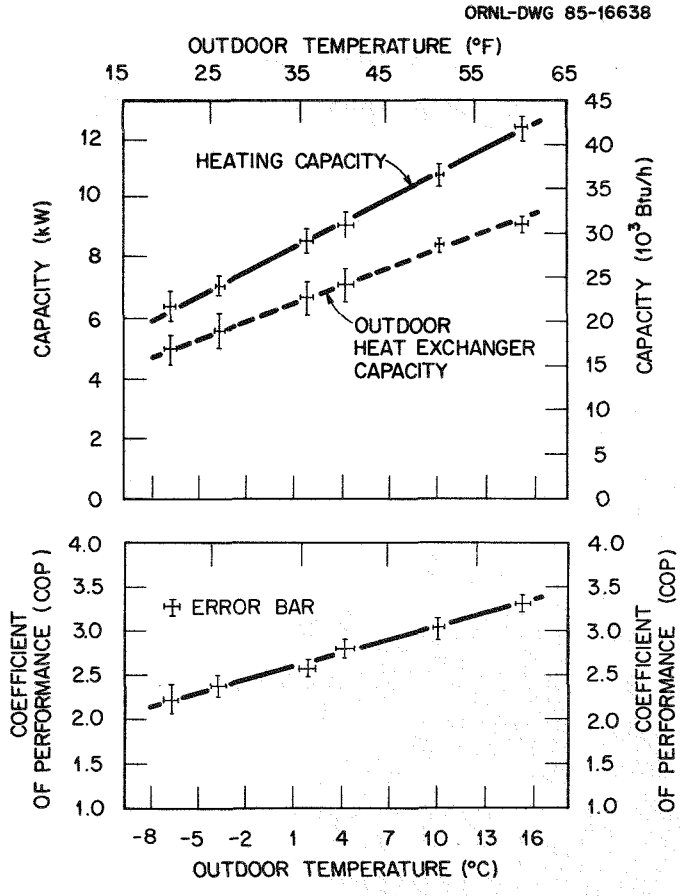

Fig. 5.1. Steady state system performance measured at a constant indoor temperature of 21.1°C (70°F).

respectively. The steady state performance data for the above tests are tabulated in Appendix A.

For these steady state tests, subcooled refrigerant was obtained and visually observed upstream of the outdoor throttle for outdoor air temperatures greater than 4.4°C (40°F). However, below 4.4°C (40°F), two-phase flow through the liquid line caused an increase in uncertainty of measurement of refrigerant mass flowrate. Under these conditions, to calculate the refrigerant mass flowrate, a quality of refrigerant exiting the indoor coil was calculated using the air-side measurement of capacity, and then the quality was applied to correct the measurements from the refrigerant flowmeter. The resulting increase in measurement uncertainty is reflected in Figs. 5.1 and 5.2 for calculations of outdoor coil capacity and compressor shell isentropic efficiency.

The compressor shell isentropic efficiency increased from 46.7 at -6.7°C (20°F) outdoor temperature to 53.1 at 15.5°C (60°F) (Fig. 5.2). The increase of outdoor temperature yielded nearly linear increases in

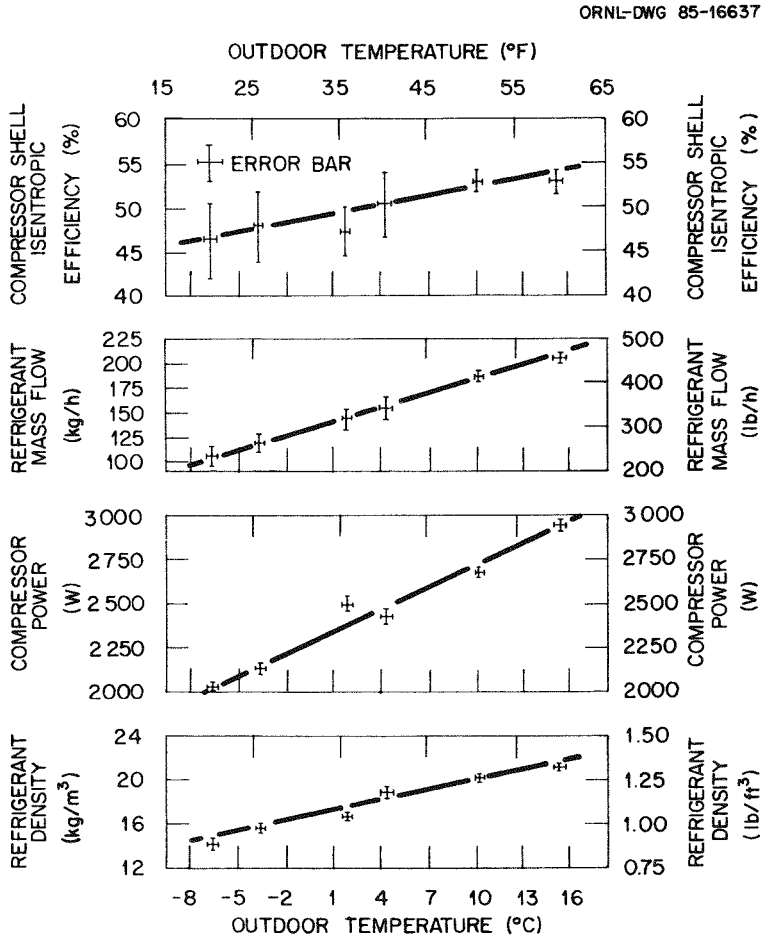

Fig. 5.2. Steady state performance traits.

refrigerant mass flowrate, compressor power consumption, and refrigerant density at the compressor inlet. These increases are the result of an increase in evaporator capacity as seen by the increase in refrigerant temperature within the outdoor coil as the outdoor temperature increased (Fig. 5.3). This increase of refrigerant temperature in the evaporator, and thus refrigerant pressure, caused an increase of refrigerant density entering the compressor. As a result the constant volume reciprocating compressor pumped a greater refrigerant mass flowrate. Since the reciprocating compressor operated at constant speed, the compressor motor drew more power to pump the increased refrigerant mass flowrate. The rate of increase in refrigerant mass flowrate was greater than the rate of increase in compressor power consumption and was reflected in the higher COP and compressor efficiencies at the higher ambient temperatures.

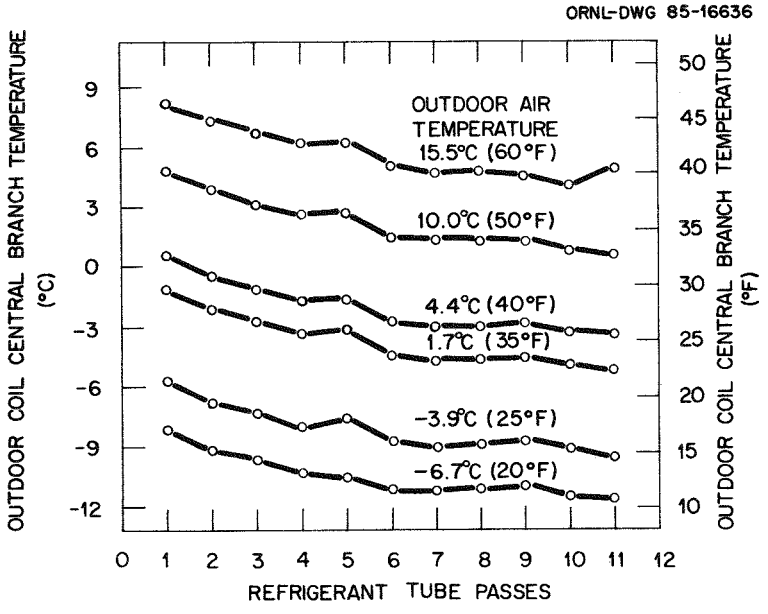

Fig. 5.3. Outdoor heat exchanger refrigerant temperature profile.

5.2 STEADY STATE REFRIGERANT CHARGE DISTRIBUTION

The refrigerant temperatures at various points within the outdoor coil (Fig. 5.3) show the coil to have predominantly two-phase refrigerant within its circuits. At the outdoor ambient temperature of 15.5°C (60°F), cool vapor was measured exiting the outdoor coil and was observable by the rise in refrigerant temperature in the last tube pass of the coil (Fig. 5.3). However, below 15.5°C (60°F) outdoor temperature saturated refrigerant exited the outdoor coil, and the vapor quality decreased with decreasing outdoor temperature. The saturated refrigerant entered the accumulator, where the liquid refrigerant that did not

either flash to vapor or become entrained within the vapor flow to the compressor was stored. Visual observations of refrigerant level in the accumulator, as plotted in Fig. 5.4, revealed a gradual filling of the accumulator with liquid refrigerant as outdoor temperature dropped. Figure 5.4 indicates a noticeable change in level of stored refrigerant within the accumulator that was due to the changing velocity characteristics within the U-tube. The change in level occurred when the refrigerant rose above a metering hole located 63.5 mm (2.5 in.) from the accumulator bottom. When refrigerant rose above this hole, the vapor velocity passing through the tube was reduced and thus less liquid refrigerant was entrained within the U-tube to be pumped by the compressor.

The storage of refrigerant in the accumulator resulted in a redistribution of refrigerant charge within the refrigerant circuit as depicted in Fig. 5.5. At 10°C (50°F) outdoor temperature, the outdoor unit contained 13.5% of the total refrigerant charge, while calculations showed that the indoor coil held 75% of the total charge. As the temperature decreased, more refrigerant was observed in the outdoor unit due to the storage of refrigerant in the accumulator. At the lower outdoor temperature of -6.7°C (20°F), both the outdoor and the indoor heat exchanger each held roughly 44% of the total refrigerant charge. The reduction of indoor coil charge coupled with the reduction of refrigerant mass flowrate decreased heat exchanger effectiveness and reduced COP and capacity as the outdoor temperature dropped.

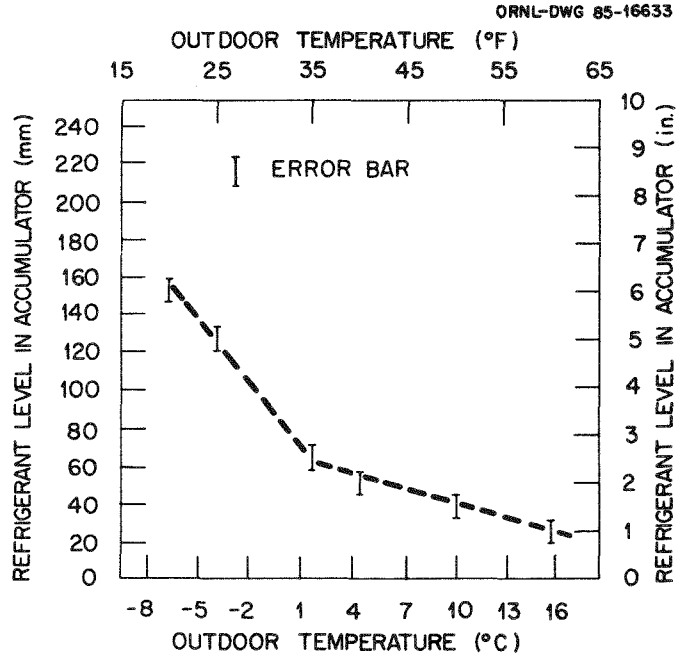

Fig. 5.4. Refrigerant level in accumulator.

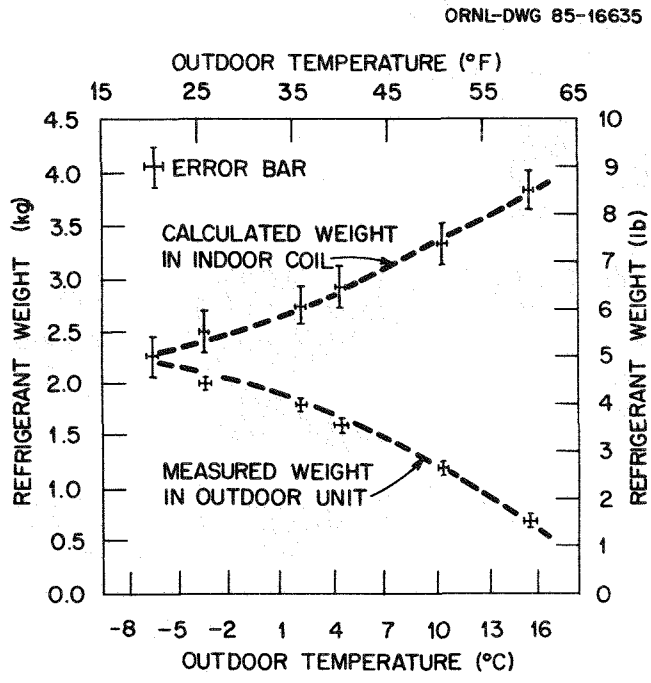

Fig. 5.5. Heat pump refrigerant charge distribution.

5.3 HEAT PUMP CYCLING OPERATION

The part-load operation of the single-speed, split-system, air-to-air heat pump was observed in the laboratory to gain an understanding of the driving forces resulting in the cycling loss. Heat pump cycling trends were analyzed to gain insight to the underlying causes of cycling that resulted in the degradation of COP. Off-cycle and on-cycle transients are discussed for cycling tests conducted at 10°C (50°F) outdoor temperature having an 8-min-on and 30-min-off (21% on-time) cycling rate. For this analysis the test heat pump operated with a refrigerant charge of 5.7 kg (12.5 lb), which was 2.3 kg (5 lb) more than nameplate charge. The overage of refrigerant charge affected cycling efficiency, as reviewed in Appendix B; however the cycling trends were similar. Cycling tests were later repeated with the nameplate charge of 3.4 kg (7.5 lb) to better quantify cycling losses for seasonal analyses.

5.3.1 Heat Pump-Off Cycle Refrigerant Migration

At the start of the 30-min off cycle, subcooled refrigerant was observed flowing through the liquid line for 45 s during which 1.1 kg (2.5 lb) of refrigerant migrated to the outdoor unit. Refrigerant flashed to vapor as it discharged from the indoor coil during the first 5 min, while roughly 94% of the total refrigerant migration occurred. The migration of refrigerant caused indoor and outdoor heat exchanger temperatures to change roughly 11C° (20F°) within this 5-min interval (Fig. 5.6). The rapid increase in outdoor coil wall temperature was the

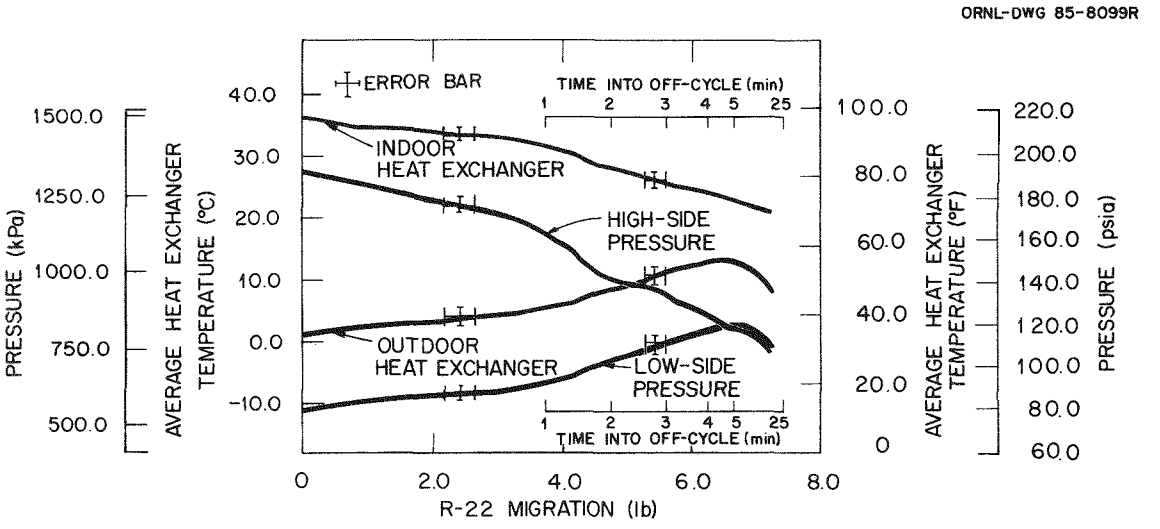

Fig. 5.6. Average heat exchanger temperature and refrigerant pressure plotted as a function of refrigerant migration to the outdoor unit during the off cycle of an 8-min-on and 30-min-off cycling test conducted at 10°C (50°F) outdoor temperature.

result of latent heat transfer from condensing refrigerant that migrated to the outdoor coil. Throughout the first 5 min of the off cycle, the refrigerant saturation temperature was greater than outdoor coil wall temperature, and the refrigerant vapor that accumulated in the outdoor coil had to condense to allow further migration. Thus the rate of migration was governed by the heat exchanger wall temperature. Similar results were also observed by Murphy and Goldschmidt.[7] Both outdoor coil temperature and refrigerant pressure reached a maximum off-cycle level that coincided in time with the majority of refrigerant migration (Fig. 5.6). When migration stopped, system high-side and low-side pressures (Fig. 5.6) had equalized; however, both these pressures continued to drop as the outdoor coil temperature continued to equilibrate with the surrounding ambient temperature.

The accumulator wall temperature as a function of time into the off cycle is plotted in Fig. 5.7. The figure shows that refrigerant migration continued through the outdoor coil and into the accumulator and possibly into the compressor. Little variation in the wall temperature of the accumulator was seen during the on cycle; however, a definite temperature variation was observed along the height of the accumulator during the off cycle. A maximum temperature variation occurred at roughly 6 min into the off cycle and revealed the accumulator to be half filled with liquid refrigerant. During the off cycle, refrigerant vapor condensed, as seen by the decrease in wall temperature for the upper half of the accumulator. This refrigerant vapor migration to the accumulator and compressor is implied from temperature measurements; however, the exact amount of off-cycle migration to the individual components of the outdoor unit cannot be determined from the data.

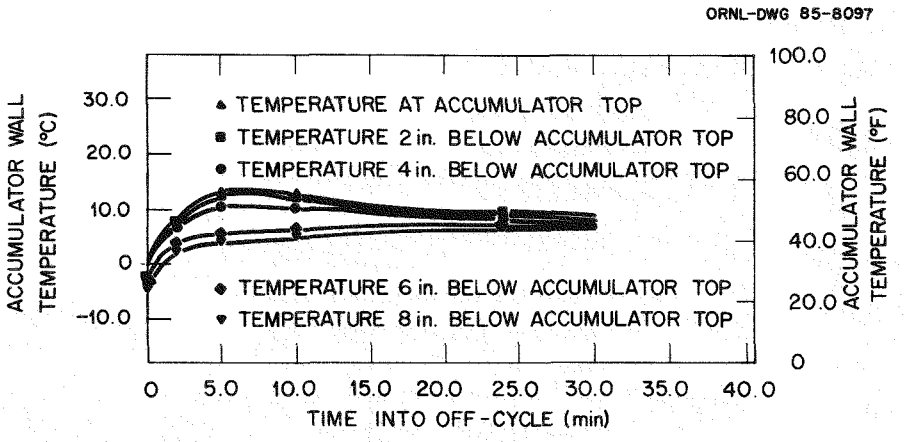

Fig. 5.7. Accumulator wall temperatures observed during the off cycle of an 8-min-on and 30-min-off cycling test conducted at 10°C (50°C) outdoor temperature [uncertainty in wall temperature ±0.3°C (0.5°F) at 20:1 odds].

5.3.2 Heat Pump Start-Up Transients

The migration of refrigerant during the off cycle resulted in start-up refrigerant dynamics that are crucial in terms of the cycling loss. The outdoor heat exchanger and accumulator hold most of the migrated refrigerant in the outdoor unit just before system start-up. Within one minute, the compressor pumped approximately 1.8 kg (4.0 lb) of refrigerant from system low-side to high-side (Fig. 5.8). A peak in compressor power is also indicated in Fig. 5.8 at approximately 30 s of operation. This peak occurred because of a high density of saturated

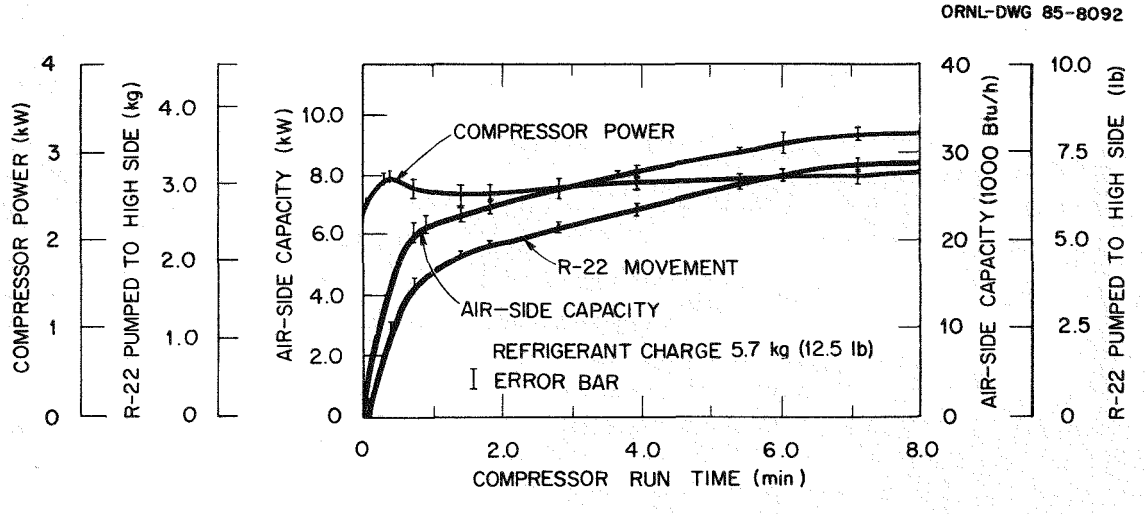

Fig. 5.8. Capacity, compressor power, and refrigerant pumped to the high side during the on period of an 8-min-on and 30-min-off cycling test conducted at 10°C (50°F) outdoor temperature.

refrigerant vapor being pumped by the compressor. The saturated refrigerant conditions within the compressor housing are implied from a sharp drop in housing temperature measured at the compressor oil level.

As time progressed into the on cycle, the evaporator pressure decreased as the compressor continued to pump refrigerant to the high-side. This drop in pressure caused a flashing of refrigerant in the evaporator, which dropped the outdoor coil wall temperature by 8.3°C (15°F) (Fig. 5.9). The indoor coil was calculated to hold only 0.22 kg (0.5 lb) of refrigerant vapor at start-up; therefore infering that a high quality of saturated mixture was throttled by the outdoor capillary for approximately 2 min of compressor operation. The mass flowrate through the liquid line was well below steady state levels because the majority of refrigerant was still in the outdoor unit. The evaporator coil became starved for refrigerant and the accumulator, serving to protect the compressor, filled with liquid refrigerant.[13] These refrigerant dynamics around the accumulator and compressor caused the heat exchangers to be undercharged and to result in the change in slope of cycling heat output (Fig. 5.8). The development of steady state charge distribution was gradual after 2 min of compressor operation (Fig. 5.8) because liquid refrigerant in the accumulator must be pumped through the orifice at the bottom of the accumulator U-tube (i.e., liquid refrigerant and oil return hole).

High-side refrigerant pressure and average indoor heat exchanger temperature (Fig. 5.9) continued to increase until a steady state refrigerant distribution was established after 10 min of heat pump operation. Steady state COP and capacity were established at roughly 15 min of operation. However, steady state COP and capacity for the test unit operating with nameplate charge was established within 5 min (Appendix B).

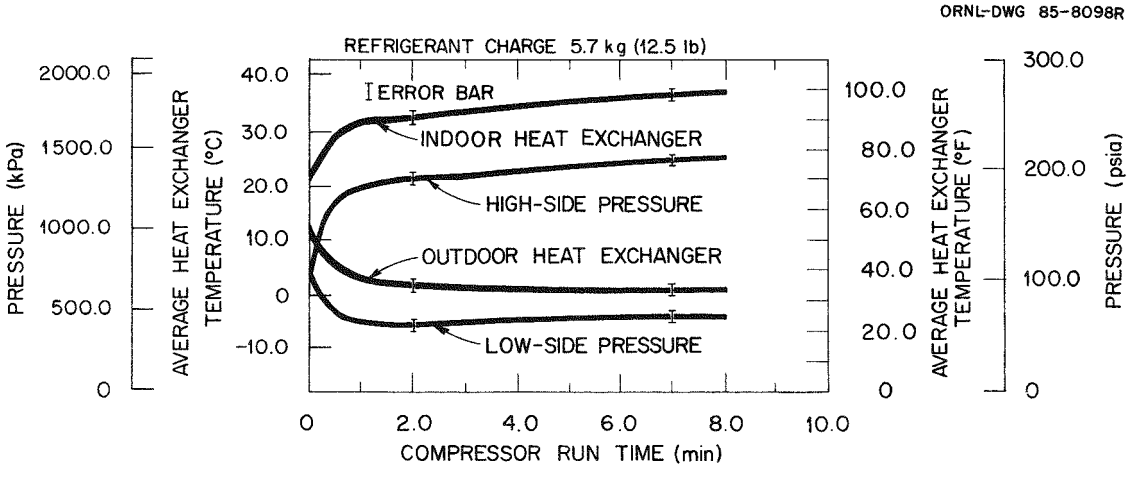

Fig. 5.9. Average heat exchanger temperature and refrigerant pressure measured during the on period of an 8-min-on and 30-min-off cycling test conducted at 10°C (50°F) outdoor temperature.

5.3.3 Affect of Outdoor Ambient Temperature on Cycling

The COP and heating capacity of a heat pump were affected by outdoor heat exchanger capacity, which was a function of outdoor temperature. Steady state and cycling COP decreased as outdoor temperature decreased; however, the ratio of cycling COP to steady state COP increased with decreasing outdoor temperature. This inverse relationship of cycling COP ratio and outdoor temperature was caused by refrigerant density affects.

The curves of Fig. 5.10, representing heat pump performance as related to load and cycling rate, displayed improvement in the ratio of cycling to steady state COP as outdoor ambient temperature decreased from 10°C (50°F) to -1°C (30°F).* The COP observed at 10°C (50°F) outdoor temperature and 90% on-time degraded 6.6% of steady state value, while at -1°C (30°F) outdoor temperature and 90% on-time COP degraded 4%. Cycling COP observed for both temperatures at 20% on-time were degraded by roughly 30% of steady state COP and capacity.

Capacity, normalized to steady state capacity, improved for cycling tests conducted at 21% on-time (8-min-on and 30-min-off) as the outdoor

*Heat pump cycling would not be expected for outdoor temperatures such as -1.1°C (30°F) that would be below the house balance point. However, a broad temperature range was selected in these experiments to observe its affect on cycling dynamics.

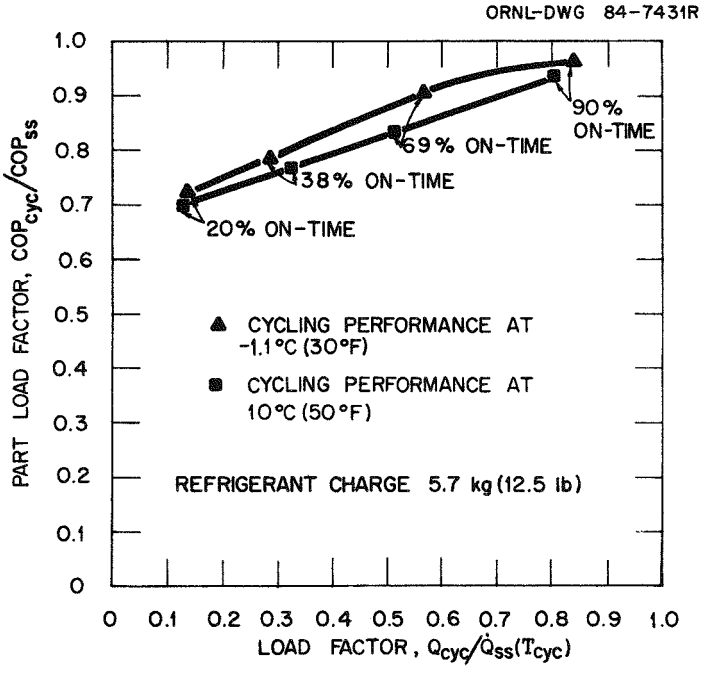

Fig. 5.10. Outdoor temperature affect on heat pump part-load factor.

temperature decreased from 10°C (50°F) to -1°C (30°F) (Fig. 5.11). Normalized compressor power trends were similar for the two outdoor temperature cycling tests; however, compressor start-up transients were less severe for the lower temperature test (Fig. 5.11). Also steady state compressor operation was established more rapidly at the lower temperature test.

Refrigerant weight as a function of compressor run time (Fig. 5.12) reveals that 3.4 kg (7.4 lb) of refrigerant was pumped to the indoor coil and liquid line during the 8-min-on period of the 10°C (50°F) cycling test.* At -1°C (30°C) outdoor temperature, 2.3 kg (5 lb) of refrigerant was pumped from the outdoor unit during the 8-min-on period. The decrease in outdoor temperature caused evaporator pressure to decrease and thus lowered refrigerant density at the compressor inlet. These reductions of refrigerant properties, in turn, decreased the pumping ability of the compressor and resulted in the 1.1 kg (2.4 lb) differential of refrigerant movement as a function of outdoor temperature. More refrigerant was circulating throughout the system at 10°C (50°F) outdoor temperature, so the cycling losses were greater due to the time required to boil off refrigerant within the accumulator. A time lag of 12 min was observed in establishing near steady state condensing and evaporating temperature and pressure for the 10°C (50°F), 21% on-time cycling test. However, only 6 min were required to establish quasi-steady state condensing and evaporating conditions for the -1°C (30°F) cycling test. Thus cycling losses decreased with decreasing outdoor temperature because less time was required to achieve proper system charge distribution as temperature decreased.

*System allowed to cycle on to equilibrium after three previous 8-min-on and 30 min-off cycles.

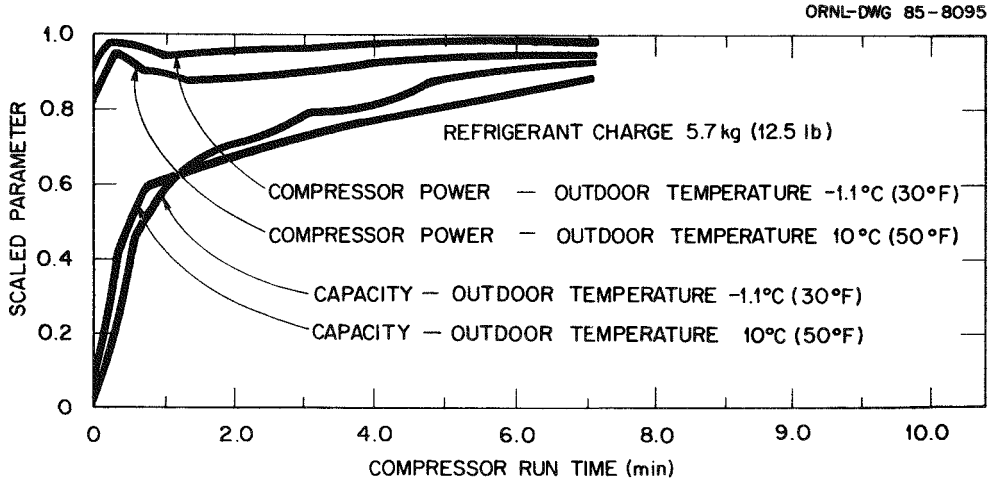

Fig. 5.11. Capacity and compressor power, normalized to steady state value, for the on period of 8-min-on and 30-min-off cycling tests.

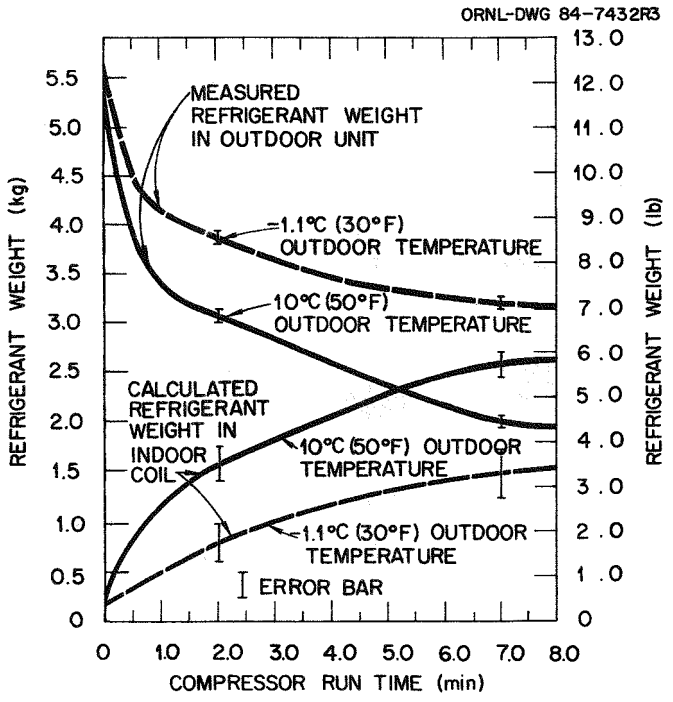

Fig. 5.12. On period refrigerant charge distribution as affected by outdoor temperature for cycling tests have 8-min-on and 30-min-off cycling rate.

The dependence of part-load COP on outdoor temperature revealed that both duty-cycle and refrigerant dynamics caused more severe COP cycling degradations in the warmer months of the heating season as compared with those of the colder portion of the heating season. The result also showed that the load factor (as related to heating load and cycling rate) was dependent on outdoor temperature.

5.3.4 Cycling Control Strategies

A series of heating mode cycling tests were conducted at 10°C (50°F) outdoor temperature to measure system improvements resulting from the control strategies listed in the introduction. The part-load factor (PLF) is plotted in Fig. 5.13 as a function of load factor for an indication of cycling efficiency resulting from these control strategies.

Best part-load efficiency was obtained by combining off-cycle refrigerant migration control with a 2-min delay in indoor blower shutdown. At 68% on-time, COP and capacity degradations for this strategy were 3.9 and 9.6% of steady state value, while for normal mode cycling degradations they were 16.9 and 28%, respectively. At 20% on-time, the PLF for only off-cycle migration control dropped slightly below the PLF observed with 2 min of extended indoor blower operation only (Fig. 5.13). During the off cycle of the refrigerant migration control cycling test, the isolation valves leaked ~2 lb (0.9 kg) of refrigerant.

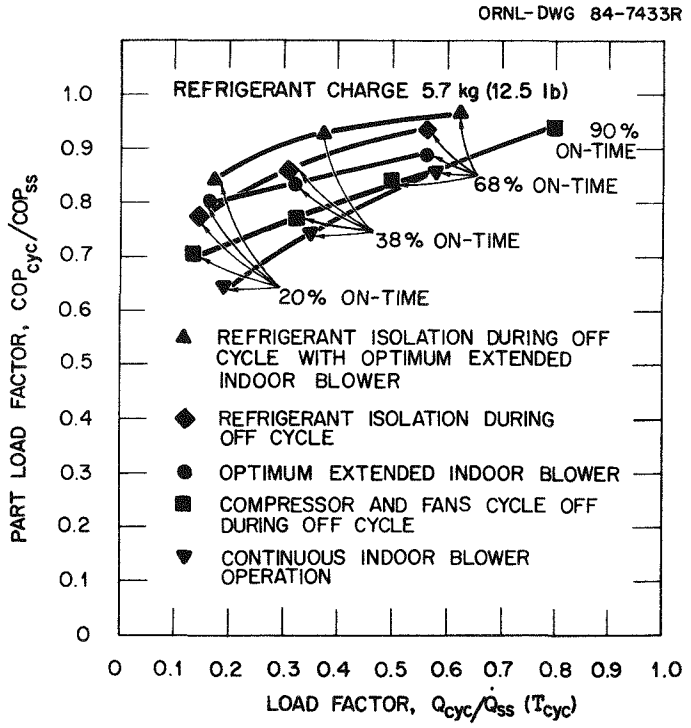

Fig. 5.13. Heat pump heating mode cycling COP observed at 10°C (50°F) outdoor temperature for various cycling control strategies.

The off-cycle refrigerant leakage coupled with decreasing on-time apparently caused the PLF to drop below PLF levels observed for extended indoor blower operation. However, at 68% on-time, off-cycle refrigerant migration control yielded greater cycling COP improvements than those observed with extended indoor blower operation.

5.3.5 Losses per Cycle

Normal mode cycling losses were compared with losses observed for cycling tests with off-cycle isolation of refrigerant in the indoor coil to reveal the underlying effects of refrigerant migration. Comparison of cycling transients was made for cycling tests having an 8-min-on and 30-min-off cycling rate conducted at an outdoor temperature of 10°C (50°F).

Normalized capacity and compressor power typify the improvement in part-load efficiency that results from isolating refrigerant within the condenser during the off cycle (Fig. 5.14). Air-side cycling capacity for the off-cycle refrigerant isolation test approached steady state output; normal mode cycling operation capacity increased more gradually as discussed in Sect. 5.3. No surge in compressor power was observed for the off-cycle refrigerant isolation test (Fig. 5.14). Power consumption, after the initial starting spike, increased steadily to near steady state power levels; however, during normal mode cycling operation, the compressor power surged due to the high density of refrigerant entering the compressor at start-up. Also, the majority of refrigerant

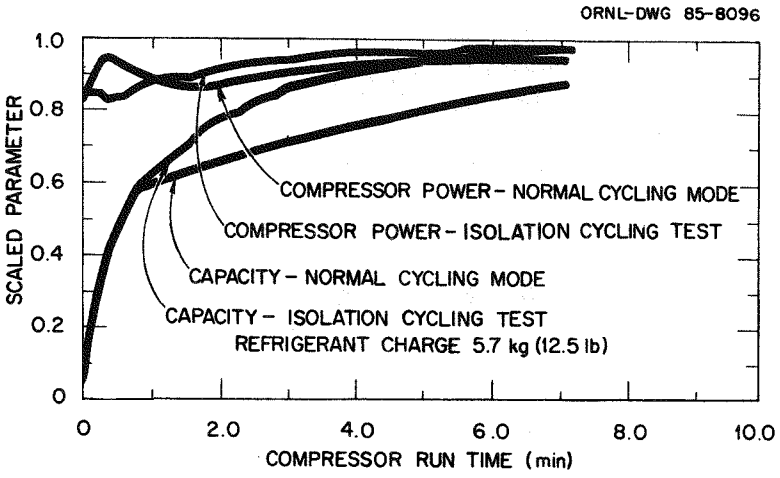

Fig. 5.14. Capacity and compressor power, normalized to steady state, for comparison of normal mode cycling to cycling with off-cycle isolation of refrigerant in the indoor coil.

was initially in the condenser, so the evaporator did not become starved for refrigerant, as occurs for normal mode cycling operation. A liquid seal, indicating subcooling at the outdoor throttle, was visually observed after 1 min of operation, in contrast to 3 min of operation in normal cycling operation. The differences in trends are again the result of start-up refrigerant dynamics that drastically affect compressor performance. Compressor housing temperature, measured at the compressor oil level, dropped 11 C° (20 F°) within 45 s for normal mode cycling as compared with the gradual increase in housing temperature for the off-cycle refrigerant isolation cycling test. The trends of compressor housing temperature in Fig. 5.15 and compressor power in Fig. 5.14 revealed the affects of start-up refrigerant dynamics on part-load COP and capacity.

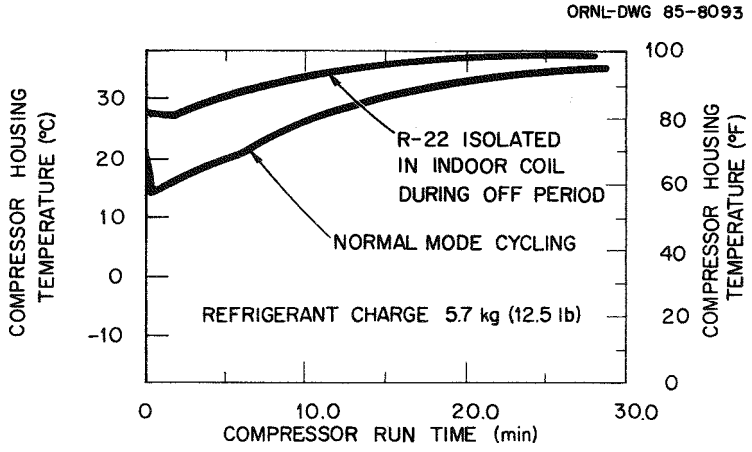

Fig. 5.15. Compressor housing temperature, measured at compressor oil level, for cycling tests having off-cycle refrigerant migration control and normal mode control [uncertainty in housing temperature ±0.3°C (0.5°F) at 20:1 odds].

6. LABORATORY TEST RESULTS: FROSTING AND DEFROSTING

Frosting and defrosting tests were conducted at outdoor ambient conditions of 4.4, 1.7, and -3.9°C (40, 35, and 25°F) with relative humidities ranging from 60 to 80%. The defrosting tests, following each frosting test, were initiated using either time and temperature control, based on a 90- or 45-min interval, or demand control, based on the total air pressure drop through the outdoor coil. Testing was conducted at the nameplate change of 3.4 kg (7.5 lb).

The frosting test results revealed the affect of temperature and humidity on the efficiency of a test heat pump having a tube and plate fin outdoor heat exchanger. Also defrost data obtained from tests using the different defrost initiators are presented in Sect. 8 for comparison on a seasonal basis of the magnitude of frosting and defrosting losses.

6.1 HEAT PUMP EFFICIENCY UNDER FROSTING CONDITIONS AT VARIOUS HUMIDITY LEVELS

Frosting tests conducted at 1.7°C (35°F) outdoor temperature revealed little degradation in COP and heating capacity as outdoor relative humidity ranged from 60 to 80%. The plots of COP and capacity in Figs. 6.1 and 6.2, respectively, reveal only marginal drops in efficiency over time despite the accumulation of frost on the outdoor heat exchanger. However, the duration of each frosting test decreased due to the accumulation of frost on the outdoor coil. A defrost cycle was initiated on demand once the total air pressure drop through the outdoor coil exceeded 0.13 kPa (0.51 in. of water) as seen in Fig. 6.3. These trends plus the decrease in outdoor airflow (Fig. 6.4) give an indication of the rate of frost accumulation on the outdoor coil. At an outdoor ambient condition of 1.7°C (35°F) and 60% relative humidity, the airflow dropped from 1180 to 850 liter/s (2500 to 1800 cfm) in ~5 hours of frosting operation. Similar drops in outdoor airflow took 2 hours for the 1.7°C (35°F) frosting test conducted at 70% outdoor relative humidity and only 50 min for the test conducted at 80% outdoor relative humidity. Thus, at the start of the respective defrost cycle for each frosting test, the outdoor coil was heavily laden with frost and had marginal free-flow area through the coil. Despite the frost accumulations and reduced outdoor airflow, the outdoor heat exchanger load decreased only marginally as reflected by the plots (Fig. 6.5) of refrigerant temperature in the outdoor coil. As a result, the density of refrigerant entering the compressor remained fairly constant over time for the respective tests conducted at 60, 70, and 80% outdoor relative humidity. These trends, in turn, caused the refrigerant mass flowrate and compressor power (Fig. 6.6) to be only slightly affected by frosting of the outdoor coil.

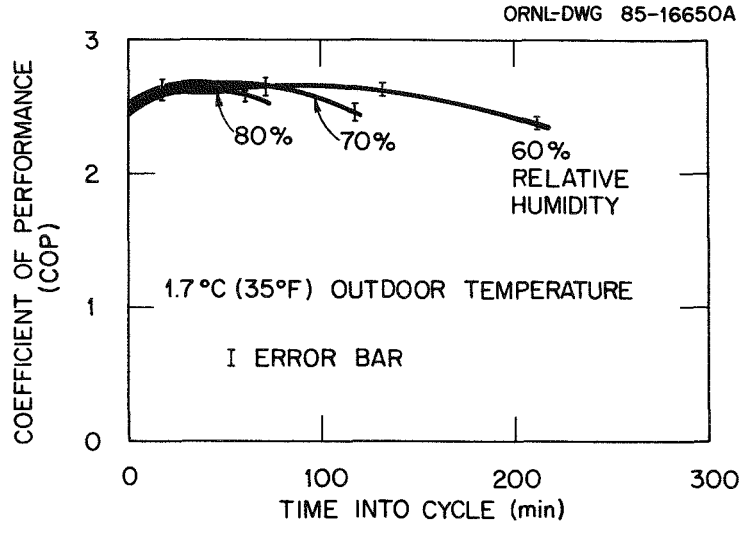

Fig. 6.1. The COP observed for frosting tests conducted at an outdoor air temperature of 1.7°C (35°F).

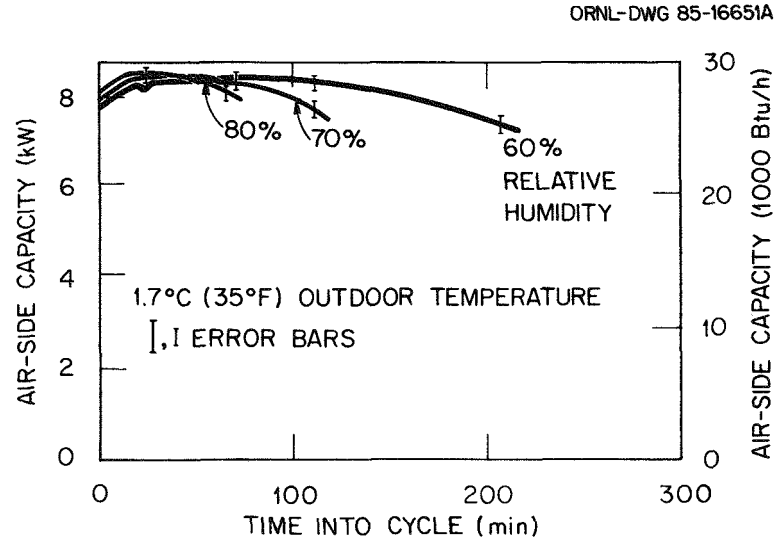

Fig. 6.2. Air-side capacity measured during frosting tests conducted at 1.7°C (35°F) outdoor air temperature.

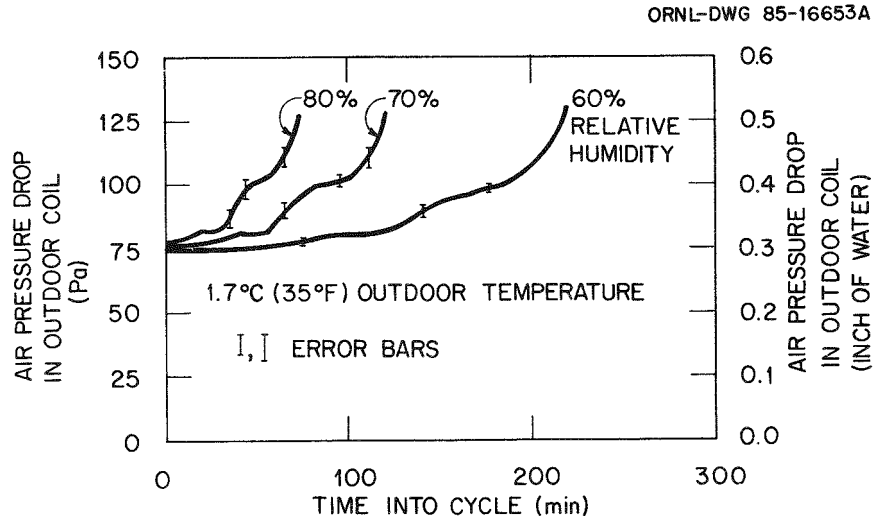

Fig. 6.3. Air total pressure drop measured across the outdoor coil under frosting conditions at 1.7°C (35°F) outdoor air temperature.

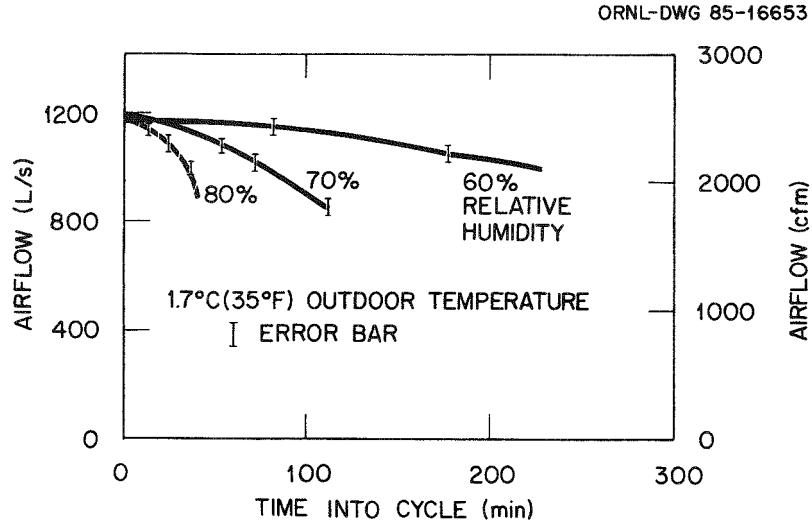

Fig. 6.4. Outdoor airflow measured under frosting conditions at 1.7°C (35°F) outdoor air temperature.

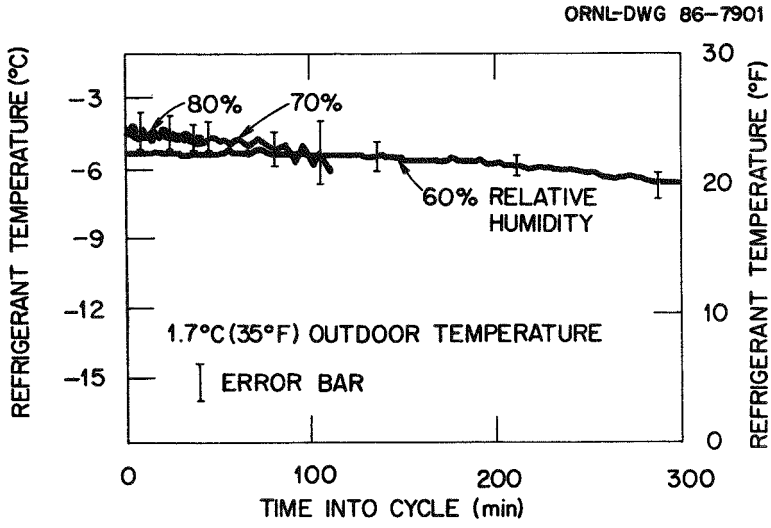

Fig. 6.5. Saturated refrigerant temperature in the outdoor coil for frosting tests conducted at 1.7°C (35°F) outdoor air temperature.

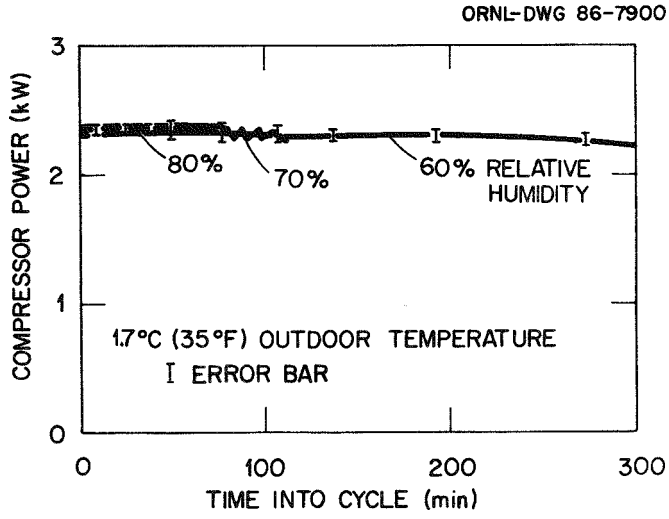

Fig. 6.6. Compressor power consumption observed for frosting tests conducted at 1.7°C (35°F) outdoor air temperature.

6.1.1 Heat Pump Frosting: Spine Fin vs Tube and Plate Fin

The above frosting trends on heat pump efficiency are much different from those previously observed for a heat pump having a one-row spine fin outdoor heat exchanger.[13] In the previous lab work by Miller, frosting of the one-row spine fin outdoor coil caused slight seasonal losses.

The COP, normalized to respective steady state value, is plotted in Fig. 6.7 for two different heat pumps that were tested in ambient outdoor conditions at 1.7°C (35°F) and 80% relative humidity. Results plotted in Fig. 6.7 indicate about a 20% degradation in COP for the heat pump with the spine fin outdoor coil, while the heat pump with a tube and plate fin outdoor coil had only a 5% drop in COP. Similarly shown in Fig. 6.8, the instantaneous capacity dropped 25% for the unit with the spine fin coil; only a 5% drop in capacity was observed for the unit with a tube and plate fin outdoor coil.

The outdoor heat exchangers of both heat pumps operated under similar loads as seen by the initial refrigerant temperatures in the outdoor coil of each unit (Fig. 6.9). During the frosting test, frost accumulation on the spine fin coil reduced coil temperature drastically as compared with temperature drops in the tube and plate fin outdoor coil. The airflow through the spine fin coil dropped 70% of its free-flow value [1322 liter/s (2800 cfm)] as compared with a 25% drop in free-flow value [1180 liter/s (2500 cfm)] for the unit having the tube and plate fin outdoor coil (Fig. 6.10).

Probably the differing efficiencies of the two heat pumps under frosting conditions resulted from the larger thermal mass of the tube and plate fin heat exchanger, differing coil geometries and fin spacing, and also differing strengths of the outdoor fan motors. The outdoor propeller fan used with the tube and plate fin heat exchanger has a 0.25-kW (1/3-hp) motor, and the propeller fan used with the spine fin coil has a 0.12-kW (1/6-hp) motor. The stronger of the two fans was able to draw 1180 liter/s (2500 cfm) against 0.08 kPa (0.30 in. of water) drop, while the other fan drew 1322 liter/s (2800 cfm) against 0.02 kPa (0.09 in. of water). The combined fan and fan motor mechanical efficiency for the fan used with the tube and plate fin outdoor coil is shown in Fig. 6.11 to have remained fairly constant at 35% efficiency. The fan used with the spine fin coil had an efficiency of only 10% and degraded slightly with time due to frosting of the outdoor coil.

Previous seasonal analysis of frosting losses for the unit with the spine fin outdoor heat exchanger had shown only a 5% degradation in heating seasonal performance factor (HSPF) due to frosting.[14] On a seasonal basis the losses are marginal, despite the affect of frosting on heat pump efficiency at an ambient temperature of 1.7° (35°F). The comparison does reveal the need for future research in heat exchanger design and fan characteristics; these factors would minimize frost accumulation, which would minimize seasonal defrost losses.

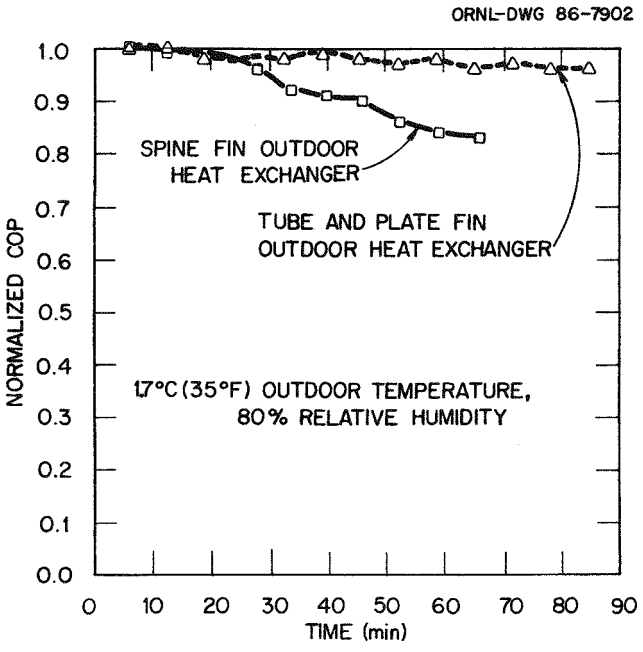

Fig. 6.7. Normalized COP for two heat pumps, one having a spine fin outdoor coil and the other having a tube and plate fin outdoor coil.

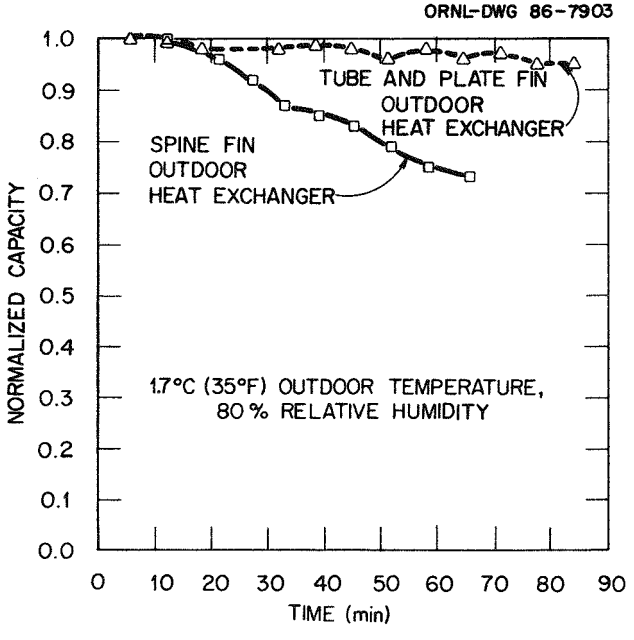

Fig. 6.8. Normalized capacity for two heat pumps, one having a spine fin outdoor coil and the other having tube and plate fin outdoor coil.

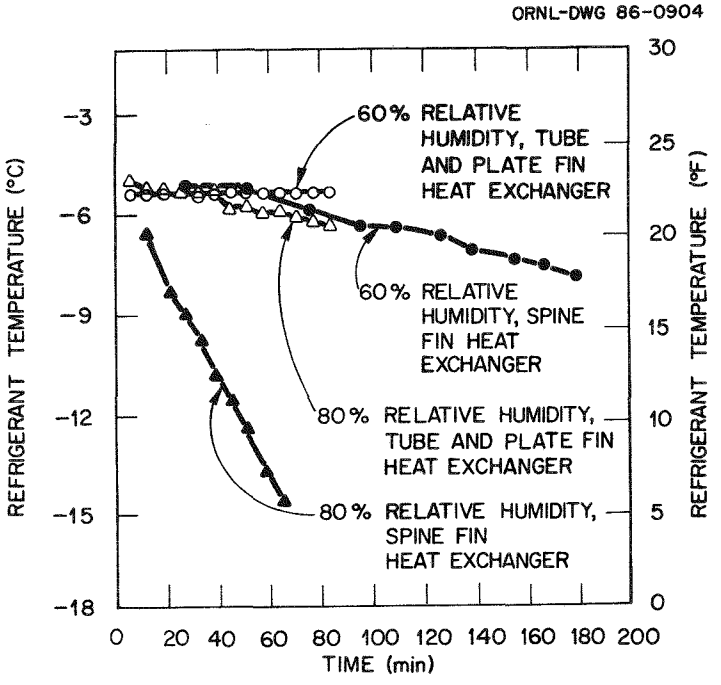

Fig. 6.9. Refrigerant temperature measured within the outdoor coils of the spine fin and the tube and plate fin heat exchangers for tests conducted at 1.7°C (35°F) outdoor temperature with 60 and 80% relative humidity.

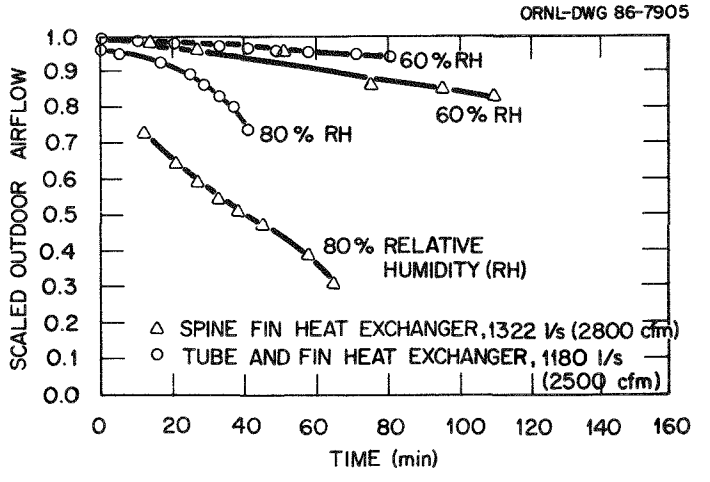

Fig. 6.10. Outdoor airflow, scaled to respective freeflow value for each heat pump for tests conducted at 1.7°C (35°F) outdoor temperature with 60 and 80% relative humidity.

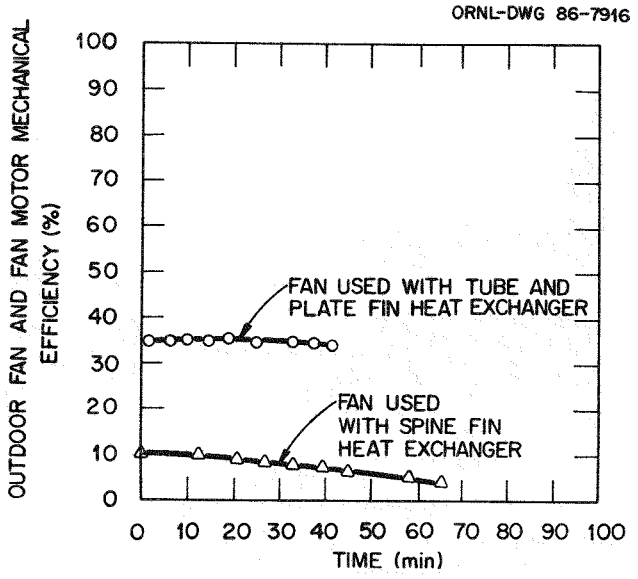

Fig. 6.11. Outdoor fan and motor efficiency measured for the two heat pumps operating under 1.7°C (35°F) outdoor temperature with 80% relative humidity.

6.1.2 Outdoor Fan Characteristics Observed Under Frosting Conditions

The characteristic curves for the outdoor fan are plotted in Fig. 6.12 as a function of outdoor airflow. Results observed under the ambient conditions of 1.7°C (35°F) and 70% relative humidity reveal that the fan operated through a region of unstable performance from roughly

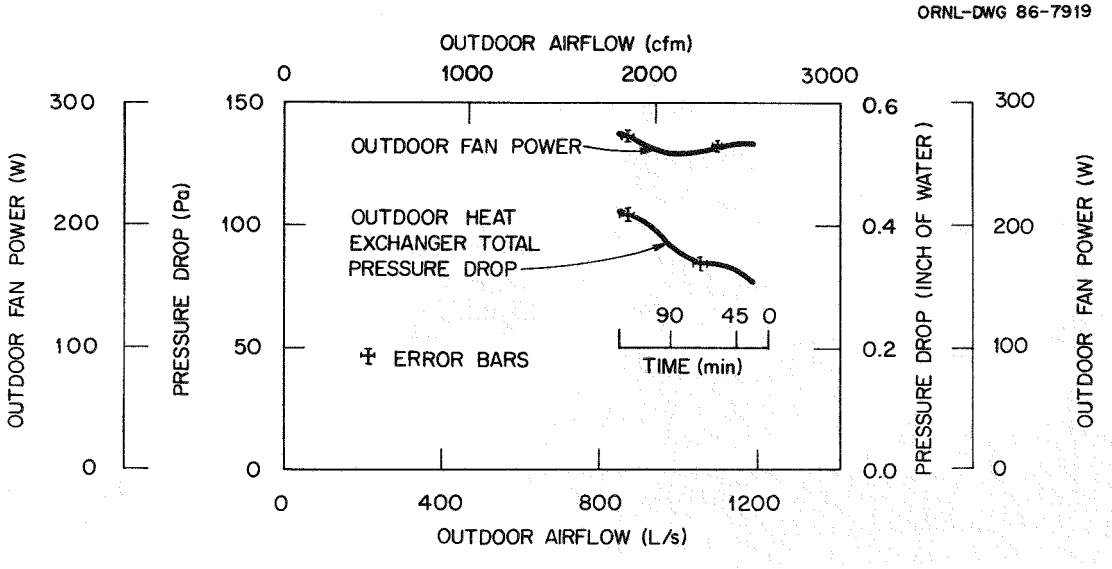

Fig. 6.12. Outdoor propeller fan characteristics observed during frosting test conducted at 1.7°C (35°F) outdoor temperature and 70% relative humidity.

50 to 100 min of heat pump frosting operation. This region of unstable performance, seen by the slight dip in total air-pressure drop through the outdoor coil, is characteristic of all propeller fans and is caused by stalling* of some part of the fan blades. This performance results in an instability and oscillation of air pressure, which is termed "surging."[15]

Frosting increased the resistance to airflow through the outdoor coil and that caused a change of operating point for the fan and coil combination. After 90 min the airflow was reduced by 15% of its free-flow airflow of 1180 liter/s (2500 cfm). Outdoor fan power dropped slightly from 45 to 90 min due to the fan operating through its surge and stall region; as frosting continued and outdoor coil pressure drop increased, the outdoor fan power increased (Fig. 6.12). The combination fan and fan motor mechanical efficiency dropped from 34.5% at near free-flow delivery to 33% after 100 min of coil frosting. At termination of the frosting test, the coil was visually observed to be heavily frosted, with the majority of frost on the lower windward portion of the coil. The frost was fluffy, indicating a porous structure through which air could still pass across the coil.

Stalling of the fan blades had little affect on the total efficiency of the outdoor fan. However, the results suggest that the outdoor fan of a heat pump should be selected to operate through a range of air pressure drops that are below pressure drops in the region that the fan would stall. The result would be in maximum fan efficiency, reduction of noise level, and less reduction in outdoor airflow, thereby prolonging time between defrosts.

6.2 HEAT PUMP EFFICIENCY UNDER FROSTING CONDITIONS AT VARIOUS TEMPERATURE LEVELS

The efficiency of the test heat pump was only slightly affected by frosting of the outdoor coil for tests conducted at outdoor temperatures of 4.4, 1.7, and -3.9°C (40, 35 and 25°F), with the outdoor relative humidity held constant at 70%. The COP and capacity, plotted in Figs. 6.13 and 6.14, respectively, reveal only marginal degradations due to frost accumulating on the outdoor coil. For these tests, defrosting was initiated when the air pressure drop through the coil exceeded 0.13 kPa (0.52 in. of water). As a result of this coil frosting, the airflow dropped from 1180 to 850 liter/s (2500 to 1800 cfm) per respective test as seen in Fig. 6.15. It should be noted (Fig. 6.15) that the rate of airflow degradation is not indicative of the rate of frost build-up on the outdoor coil. As the outdoor temperature dropped, the moisture content of the air decreased, and frosting rate therefore decreased as temperature decreased. However, for this series of frosting tests the heat pump was run through preliminary frosting and defrosting cycles at each ambient test condition prior to data collection. In Fig. 6.16 the initial air pressure drop through the outdoor

*Separation of flow occurs over a large part of the blade, resulting in disordered flow and a loss of lift and an increase of drag.

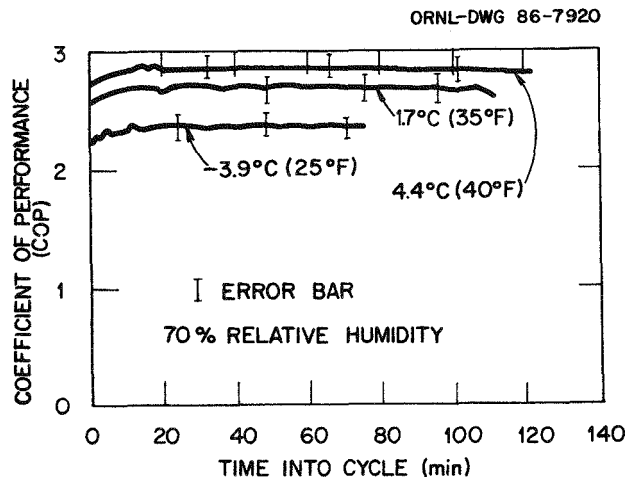

Fig. 6.13. The COP observed for various outdoor temperatures with relative humidity fixed at 70%.

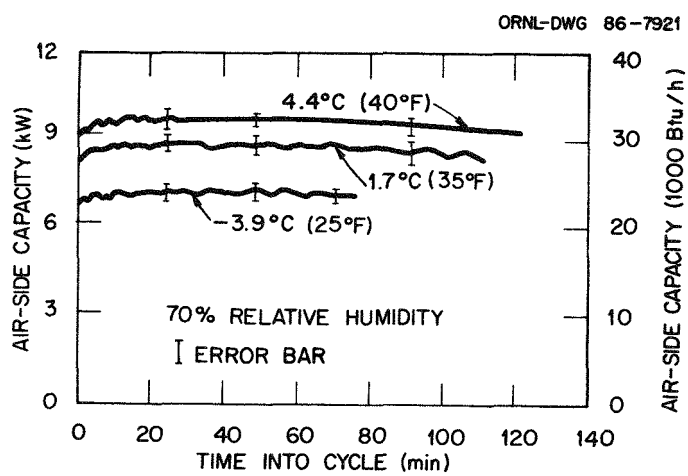

Fig. 6.14. Air-side capacity measured under frosting conditions at various outdoor temperatures with relative humidity fixed at 70%.

coil was higher for the test conducted at -3.9°C (25°F) outdoor temperature as compared with coil air pressure drops observed for the 4.4 and 1.7°C (40 and 35°F) outdoor temperature tests. Due to the lower wall temperature of the outdoor coil at -3.9°C (25°F) outdoor temperature, molten frost that did not run off the coil refroze, yielding the initially higher air restriction through the coil as seen in Fig. 6.16. This restriction possibly caused a more rapid degradation in airflow at the lower outdoor ambient temperature.

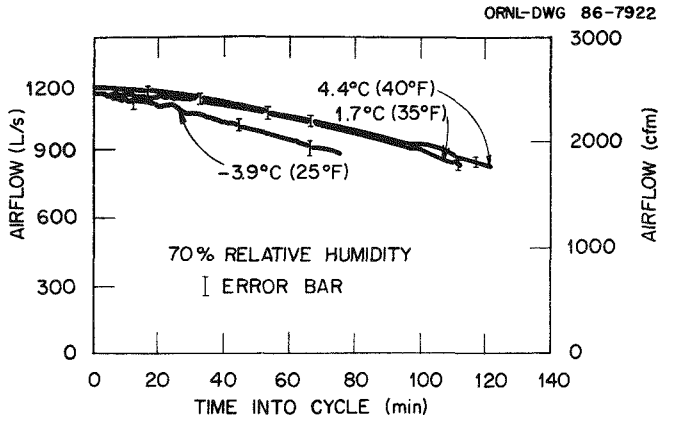

Fig. 6.15. Outdoor airflow measured under frosting conditions with relative humidity fixed at 70%.

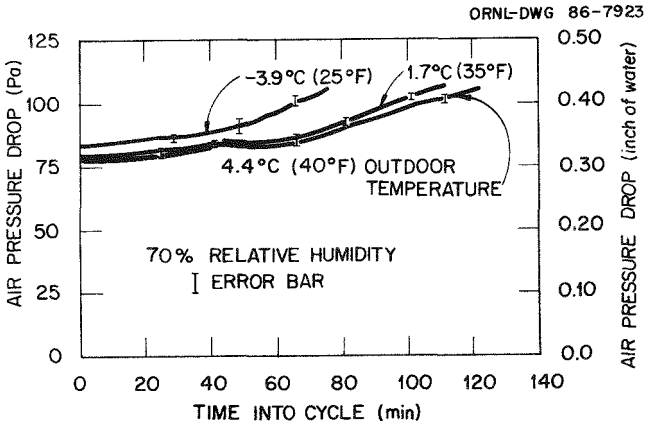

Fig. 6.16. Air total pressure drop measured across the outdoor coil for frosting tests with 70% outdoor relative humidity.

Similar drops in efficiency were also observed for tests conducted at outdoor ambient temperatures of 4.4, 1.7, and -3.9°C (40, 35, and 25°F) outdoor relative humidity of 80%. Both the COP and heating capacity showed negligible drops (Figs. 6.17 and 6.18, respectively). However, for the test conducted at 4.4°C (40°F) temperature and 80% relative humidity, defrosting was manually initiated after 90 min of compressor operation. Previously the heat pump had been run for 7 hours at that ambient condition with no frosting observed on the outdoor coil.

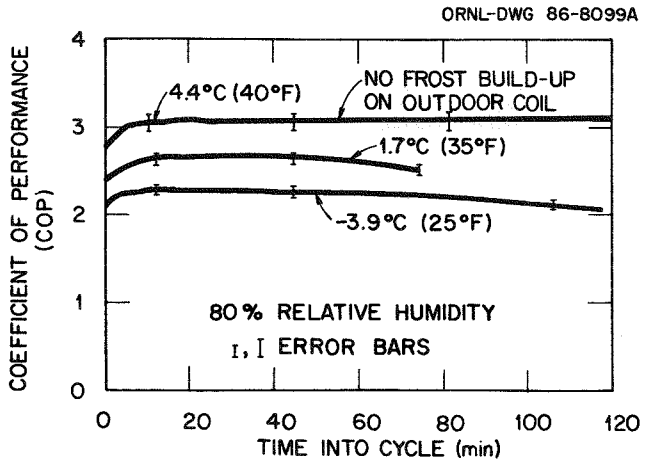

Fig. 6.17. COP observed for various outdoor temperature frosting tests with 80% outdoor relative humidity.

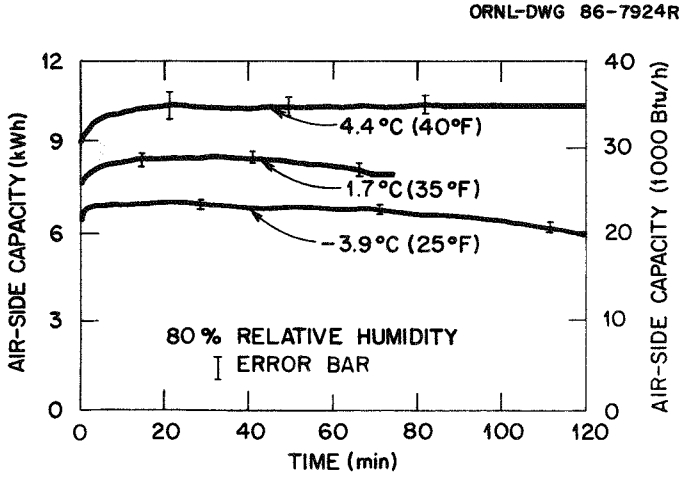

Fig. 6.18. Air-side capacity measured during frosting tests with 80% outdoor relative humidity.

6.3 REVERSE CYCLE DEFROSTING AND RECOVERY

Several defrosting methods have previously been developed for removal of frost from the evaporator of a vapor-compression system. Some of the more common defrosting methods developed use external heat such as electric heat or water sprays, natural frost melting by sublimation, hot gas by pass that uses sensible or latent heat, and reverse cycle defrosting. The reverse cycle defrosting is used extensively on air-to-air heat pumps because this method applies internal heat directly to the frost, which usually becomes loose and falls off the coil without completely melting. This defrosting method is rapid, although it does result in efficiency losses.

Capacity and compressor power trends are depicted in Fig. 6.19 for a frosting-defrosting-recovery test conducted at an outdoor air temperature of 1.7°C (35°F) with 70% relative humidity. The reverse cycle defrosting causes a chilling of the indoor return air that must be tempered to maintain comfort conditions in the residence. The power draw of both the compressor and the auxiliary heaters during defrosting will increase the energy consumption of the heat pump and degrade efficiency.

The operation of the reverse cycle defrosting and the following recovery will be analyzed to gain understanding of the affects of defrosting on heat pump components. This qualitative analysis, including refrigerant dynamics, will provide a data base for candidate improvements in defrosting efficiency.

6.3.1 The Dynamics of Heat Pump Defrosting

Defrosting for the test conducted at 1.7°C (35°F) outdoor temperature and 70% relative humidity was initiated by a demand defroster when the air total pressure drop across the outdoor coil exceeded 0.13 kPa (0.51 in. of water). Although, as previously discussed and seen in Fig. 6.19, there is little degradation in capacity caused by coil frosting even after 110 min of compressor operation.

At the start of the defrosting cycle the four-way reversing valve was energized for cooling mode operation and the outdoor fan was deenergized. The indoor coil, previously the condenser, held approximately 50% of the total charge, with the remainder of the charge distributed between the accumulator and outdoor coil as depicted in Fig. 6.20(a).

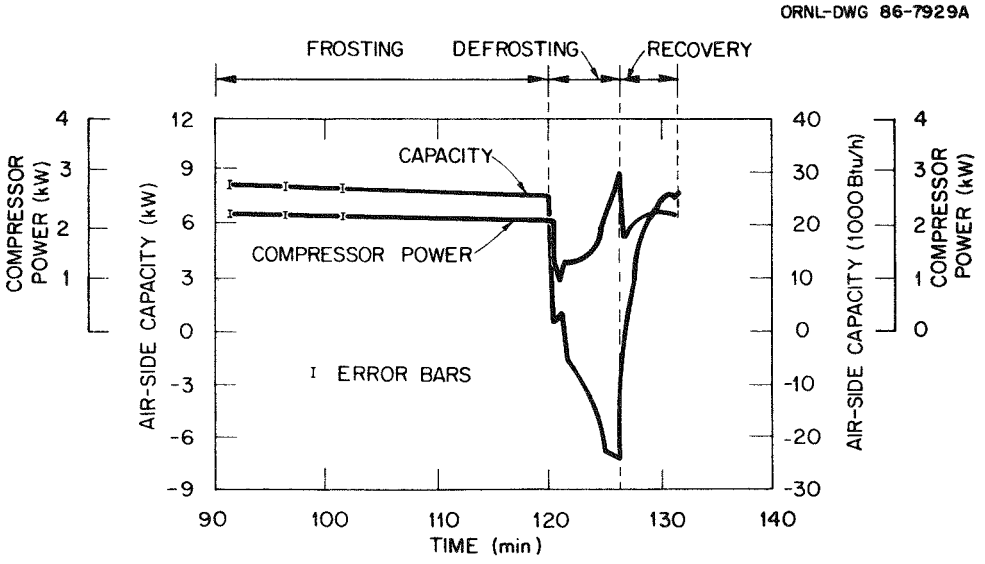

Fig. 6.19. Frosting-defrosting-recovery test conducted at 1.7°C (35°F) outdoor air temperature and 70% relative humidity.

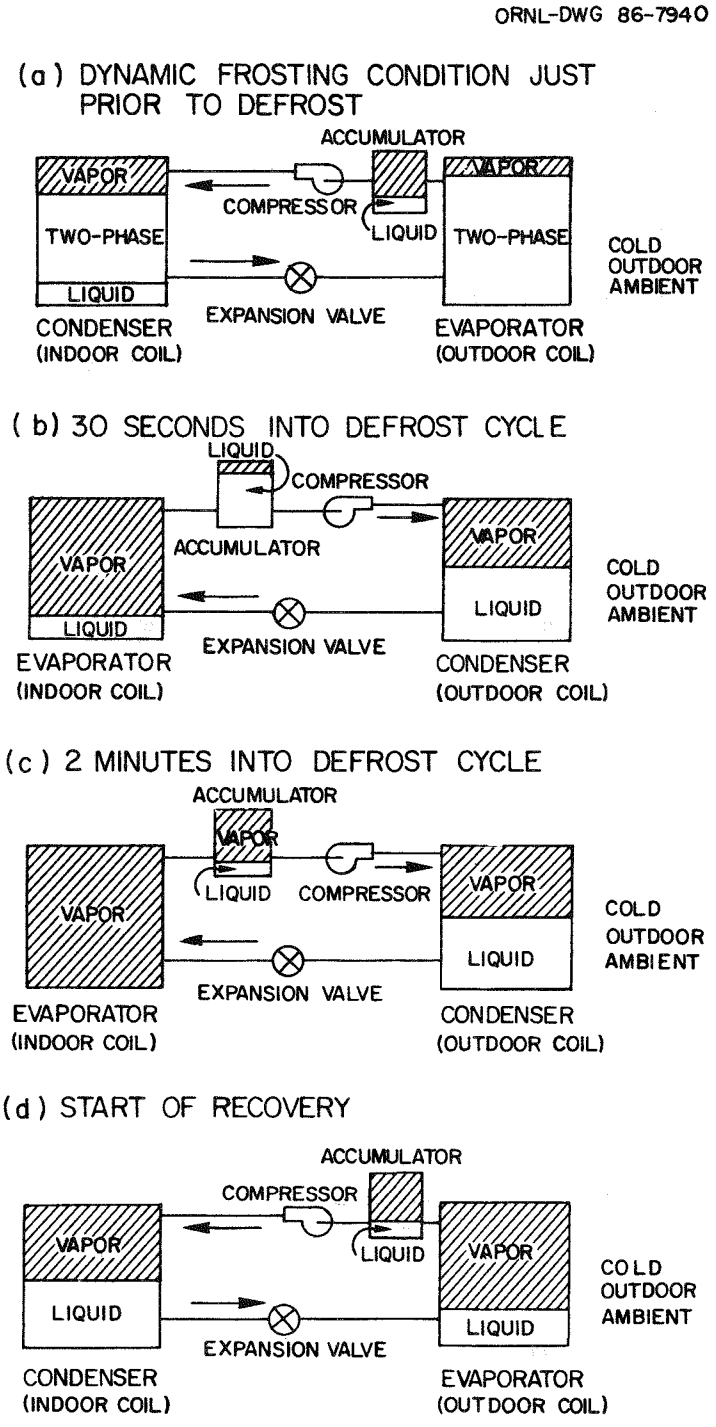

Fig. 6.20. Refrigerant inventory during defrost and recovery.

a. Dynamic frosting condition just prior to defrost
b. 30 s into defrost cycle
c. 2 min into defrost cycle
d. Start of recovery

The capacity dropped to near zero after only 30 s of defrosting (as seen in Fig. 6.19) due to the redirecting of superheated refrigerant to the outdoor coil.

The refrigerant pressures measured at the outdoor coil inlet, indoor coil exit, and compressor shell suction and discharge give an indication of the time required to develop the proper charge distribution between the cooling mode condenser and evaporator (Fig. 6.21). During the initial 1.75 min of defrosting, the pressure drop measured across the indoor capillary tube indicated a negligible flow of refrigerant through the throttle (Fig. 6.22). The indoor coil pressure fell

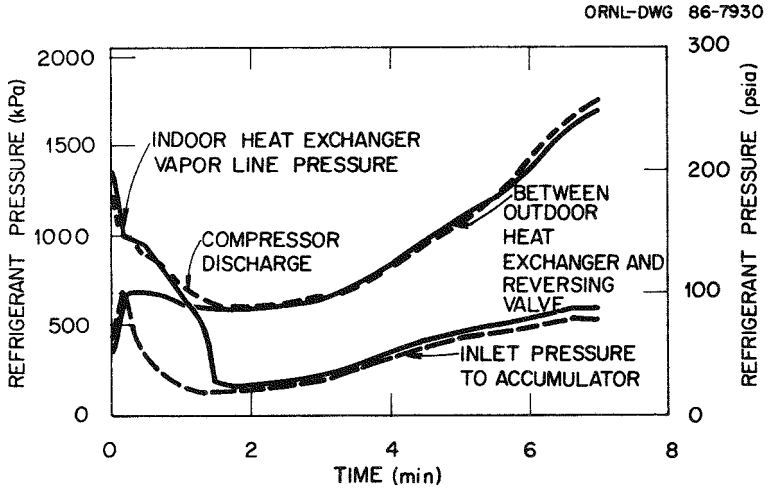

Fig. 6.21. High-side and low-side refrigerant pressures and and temperatures measured during defrost with 1.7°C (35°F) outdoor air temperature and 70% relative humidity.

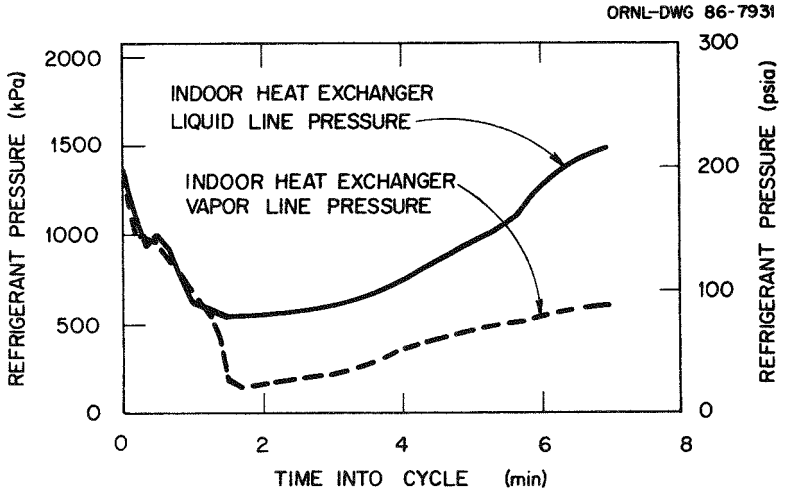

Fig. 6.22. Refrigerant pressures measured across the indoor capillary tubes during defrost with 1.7°C (35°F) outdoor air temperature and 70% relative humidity.

from 1378 to 1723 kPa (200 to 25 psia) as the compressor pumped refrigerant from the indoor coil. The refrigerant distribution after only 30 s of defrosting is depicted in Fig. 6.20(b). The refrigerant was pumped from the indoor coil and temporarily held in the accumulator; the indoor coil held primarily low pressure vapor. Since the indoor coil was starved for refrigerant, the compressor power draw fell during the first 2 min of defrosting (Fig. 6.19). As in the situation observed during dry coil cycling, the refrigerant had to be pumped through the small metering hole at the bottom of the U-tube within the accumulator. The time required to pump the refrigerant from the accumulator is reflected by the trends observed in Figs. 6.23 and 6.24. The accumulator wall temperatures (plotted in Fig. 6.23) began to increase and converge, indicating that the accumulator was emptying of refrigerant. The temperature difference between the accumulator wall (measured 3 in. from the bottom of the accumulator) and the saturated temperature of refrigerant at compressor inlet (plotted along with indoor coil capacity) (Fig. 6.24) indicated the affects of refrigerant dynamics on the time required to defrost. Little defrosting was accomplished during the first 2 min because of the refrigerant dynamics around the accumulator and compressor that result in efficiency losses. With present heat pump design, these refrigerant dynamics are unavoidable as the accumulator protects the compressor during the defrosting cycle. Plots of compressor housing temperature (Fig. 6.25) show that some refrigerant liquid returned to the compressor; however, visual observations showed that the amount of refrigerant liquid entering the compressor shell was small, again due to the protection provided by the accumulator.

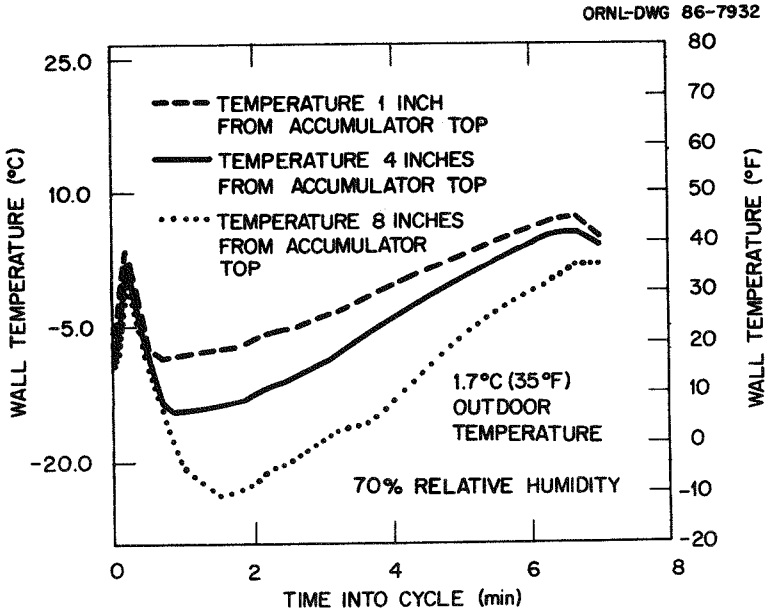

Fig. 6.23. Accumulator wall temperatures measured during defrost with 1.7°C (35°F) outdoor air temperature and 70% relative humidity.

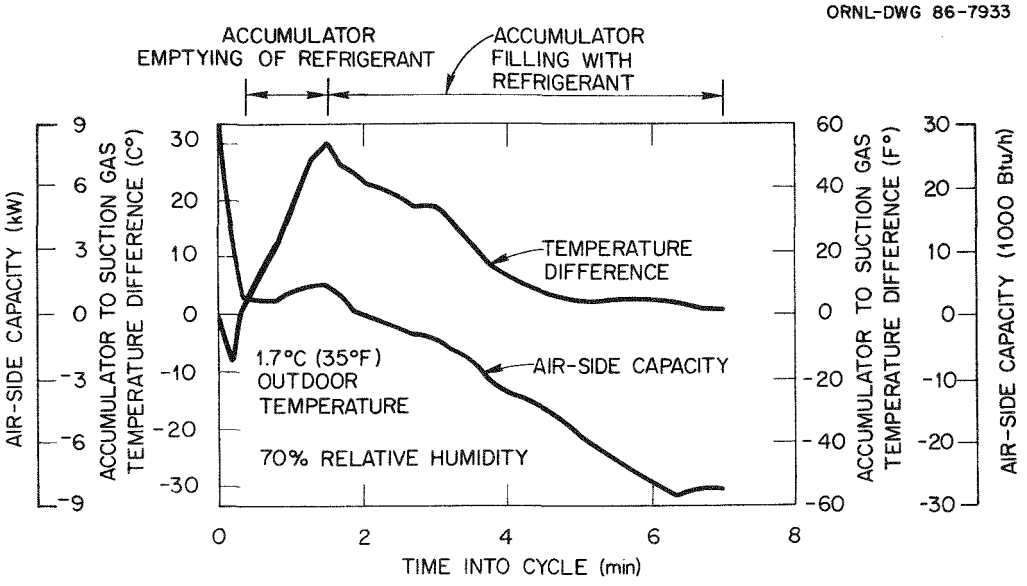

Fig. 6.24. Air-side capacity during defrost as affected by the time required to pump refrigerant from the accumulator.

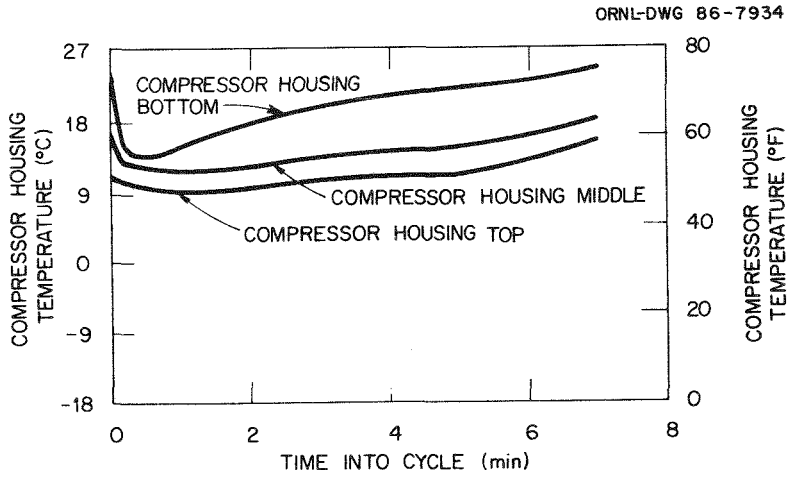

Fig. 6.25. Compressor housing temperature measured during defrost with 1.7°C (35°F) outdoor air temperature and 70% relative humidity.

The outdoor coil refrigerant pressure began to increase after 2 min of defrosting as refrigerant was pumped from the accumulator and made active within the refrigerant circuit. Refrigerant distribution within the system was characterized by Fig. 6.20(c), with the majority of refrigerant in the outdoor coil. Refrigerant temperature at exit of the outdoor coil (signal used for defrost termination) remained fairly constant through 4 min of defrosting (Fig. 6.26). Increased refrigerant subcooling indicated both sensible and latent heat transfer from the

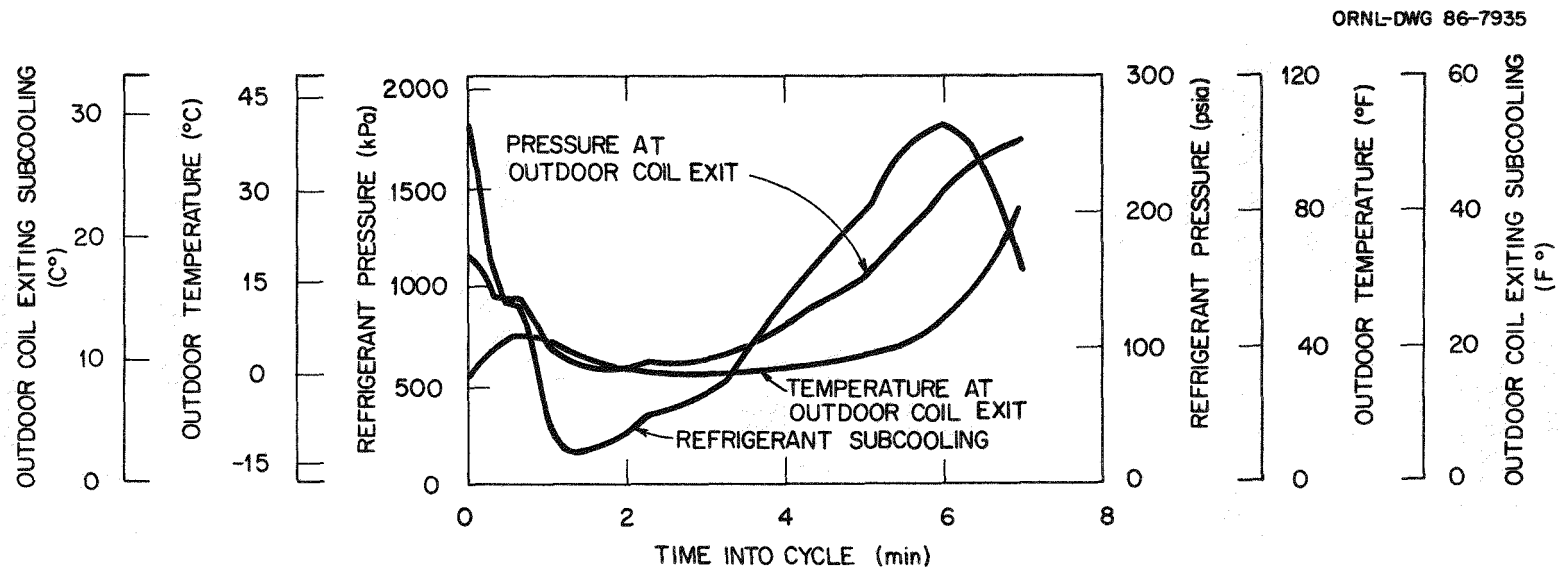

Fig. 6.26. The state point of refrigerant exiting the outdoor coil during defrost conducted at 1.7°C (35°F) outdoor air temperature and 70% relative humidity.

condenser to the frost layer on the coil. The pressure drop across the indoor throttle also began to increase, resulting in a refrigerant mass flow toward the indoor coil and back to the accumulator and compressor. The return of two-phase refrigerant to the accumulator decreased temperature difference between accumlator wall and suction saturated temperature as the accumulator wall was cooled by the entering saturated refrigerant. The refrigerant suction pressure began to increase as did the refrigerant density entering the compressor. These increases increased the compressor power (Fig. 6.19) from 2 min into defrosting until defrost termination.

As time progressed from 4 to 6 min into defrosting, there was an increase in refrigerant pressure, temperature, and subcooling at exit from the outdoor coil (Fig. 6.26). After 6 min the subcooling at exit of the outdoor coil began to drop. This drop indicated that the subcooled region in the indoor coil was decreasing as defrosting neared completion. The instantaneous capacity approached 7.3 kW (2.5 tons) cooling, indicating a minimum requirement of 4 kW of auxiliary heat from 2 min into defrost until defrost termination to negate the chilling of the indoor return air. The frost on the outdoor coil after 6 min of defrosting either had melted or fallen off the coil; as a result outdoor coil temperature and pressure continued to increase. This increase occurred because the outdoor coil was overloaded in terms of condenser capacity because the frost, acting as heat sink, had been removed. When the refrigerant temperature at the outdoor coil exit exceeded 24°C (75°F), defrosting was terminated. For the test discussed above, this condition occurred after 7 min. At this point in the defrosting cycle, most of the refrigerant was distributed between the indoor and outdoor coils, as characterized by Fig. 6.20(d). Only a 15.7-mm (4-in.) level of refrigerant was visually observed in the accumulator. Due to the declining subcooling and increasing temperature in the outdoor coil, the indoor coil probably held the greater portion of refrigerant at the termination of defrosting.

6.3.2 Recovery Cycle Following Heat Pump Defrost

Upon completion of the defrosting cycle, the four-way reversing valve was deenergized and the outdoor fan was again energized for heating mode operation. A recovery period resulted due to the time required for the indoor coil to reverse operation from evaporator to condenser. The trends of compressor power and indoor coil capacity showed this recovery to occur rapidly (Fig. 6.27). The compressor power was observed to drop slightly for 30 s and then to increase to steady state operation within 1 min. The plot of capacity in Fig. 6.27 shows near steady state operation within 5 min despite the start of recovery with an instantaneous indoor capacity of roughly 7.3-kW (2.5-tons) cooling. Each refrigerant temperature and pressure for the indoor coil, outdoor coil, condenser, and evaporator, respectively, changed rapidly and reached steady state values within 2 min, except that the refrigerant temperature at inlet to the indoor coil required roughly 4 min (Fig. 6.28).

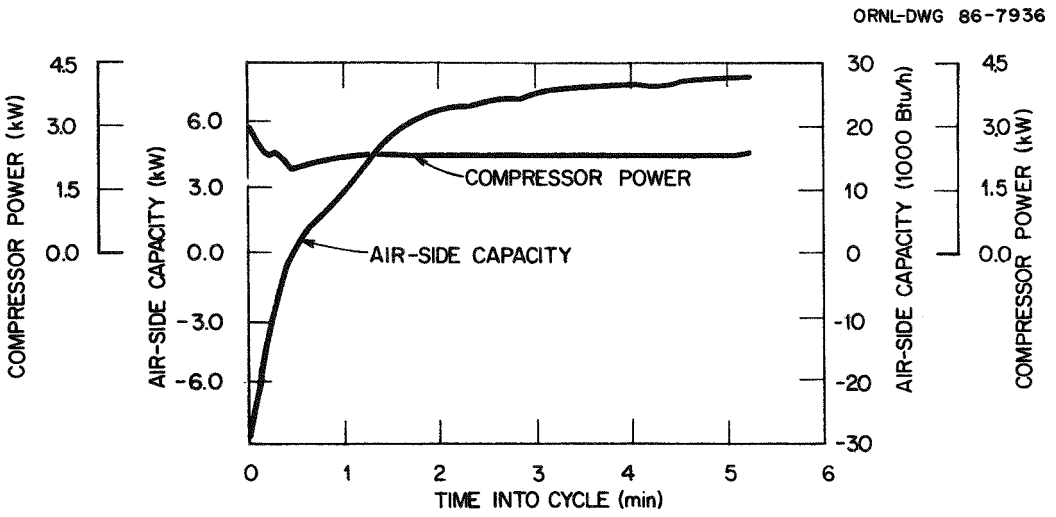

Fig. 6.27. Recovery following defrosting conducted at 1.7°C (35°F) outdoor temperature and 70% relative humidity.

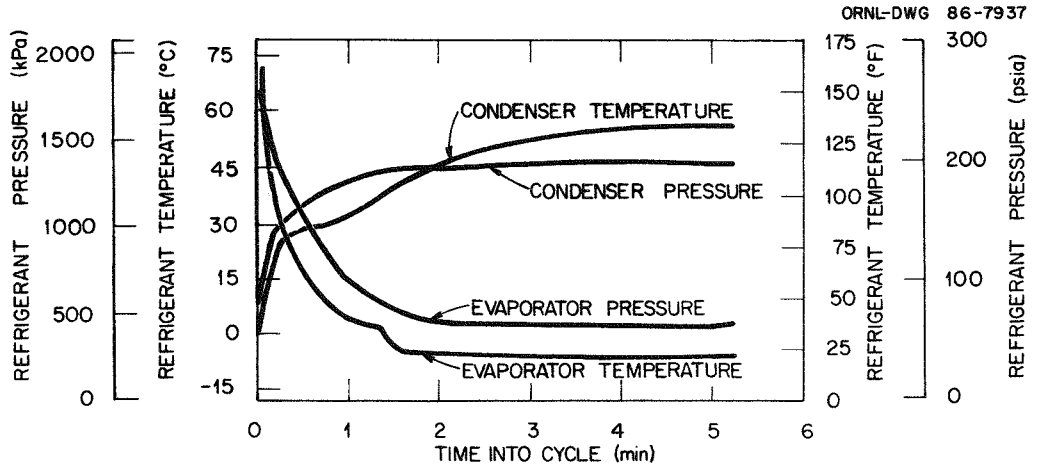

Fig. 6.28. High-side and low-side refrigerant pressures and temperatures measured during recovery with 1.7°C (35°F) outdoor air temperature and 70% relative humidity.

The rapid recovery from defrost occurred because the heat pump had close to the proper charge distribution at the start of recovery. The increasing pressure and temperature within the outdoor coil which occurred near defrost termination when little if any frost remained on the outdoor coil caused the compressor literally to push most of the refrigerant to the indoor coil. This change resulted in a refrigerant distribution as previously characterized in Fig. 6.20(d). At the start of recovery most of the refrigerant was already on the system high side and no appreciable flooding of the accumulator or the compressor was observed. As a result, the indoor air-side capacity increased rapidly having only to reestablish the temperature and pressure of the indoor coil. As compared to cycling operation there were no observed major effects due to refrigerant dynamics during the recovery period.

7. EXPERIMENTAL TEST RESULTS: COOLING

In the cooling mode the COP and capacity of an air-to-air heat pump are affected by the moisture content of the air and also by the cycling rate of the heat pump. System efficiency was examined to seek an understanding of the steady state cooling mode operation of the heat pump that had a wet indoor coil. Cooling mode cycling dynamics observed during dry indoor coil tests were addressed to gain insight into the affects of refrigerant migration on cycling efficiency of the heat pump.

7.1 STEADY STATE EFFICIENCY

Steady state cooling mode tests were conducted at indoor ambient conditions of 27°C (80°F) dry bulb and 19°C (67°F) wet bulb for outdoor dry bulb temperatures of 21, 28, and 35°C (70, 82, and 95°F), respectively. The COP, plotted in Fig. 7.1, was observed to decrease as the outdoor temperature increased. The COP at 21°C (70°F) outdoor air temperature was 2.79; at 35°C (95°F) outdoor air temperature the COP dropped to 2.29. In contrast, the air-side capacity measured at 21°C (70°F) outdoor air temperature was 9.5 kW (32 kBtu/h); at 35°C (95°F) outdoor air temperature, the capacity increased slightly to 10 kW (34.2 kBtu/h).

The sensible heat ratio (SHR) was roughly 0.82 for the above cooling mode tests. The near constancy of SHR is reflected in the constancy

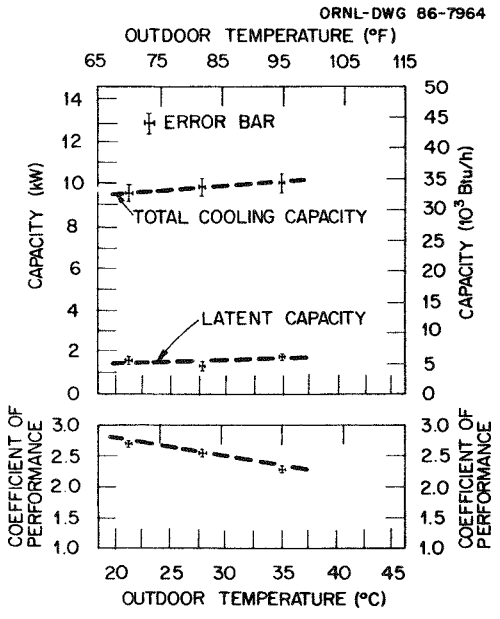

Fig. 7.1. Steady state cooling mode performance.

of latent capacity as a function of outdoor temperature plotted in Fig. 7.1. At the lower outdoor temperature, a noticeable increase occurred in the cool vapor region within the indoor coil (Fig. 7.2). This increase occurred due to the drop in suction pressure as the outdoor temperature fell from 35 to 21°C (95 to 70°F). As a result of this evaporator unloading, the refrigerant superheat at compressor inlet increased as the outdoor air temperature dropped.

The refrigerant density at compressor inlet increased as the outdoor air temperature increased due to an increase in suction pressure. The compressor is a constant volume pump, so the refrigerant mass flowrate and the compressor power increased with the increasing of outdoor air temperature. However, the compressor isentropic efficiency remained roughly 56% over the range of outdoor temperature test conditions shown in Fig. 7.3. The efficiency did not increase; the refrigerant flow per unit compressor power dropped 10% as the outdoor air temperature increased from 21 to 35°C (70 to 95°F). This trend in refrigerant mass flow per unit compressor power also helps explain the drop in COP previously shown in Fig. 7.1.

The distribution of refrigerant charge is depicted in Fig. 7.4 for the cooling mode tests conducted at 21, 28, and 35°C (70, 82, and 95°F) outdoor air temperature. At 28 and 35°C (82 and 95°F) outdoor temperature, the outdoor unit held 46.5% of the total charge, while the indoor coil held 42% of the total charge. For both of these cooling mode tests the accumulator was visually observed to be dry. As the outdoor temperature dropped to 21°C (70°F), the accumulator remained dry because the

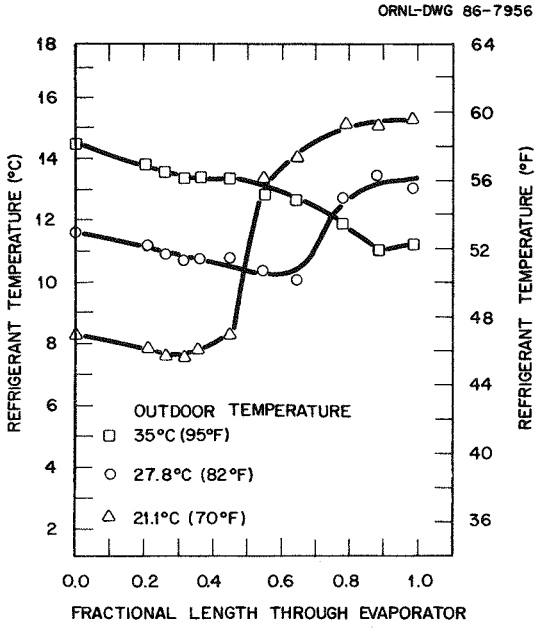

Fig. 7.2. Refrigerant temperature profile through the evaporator.

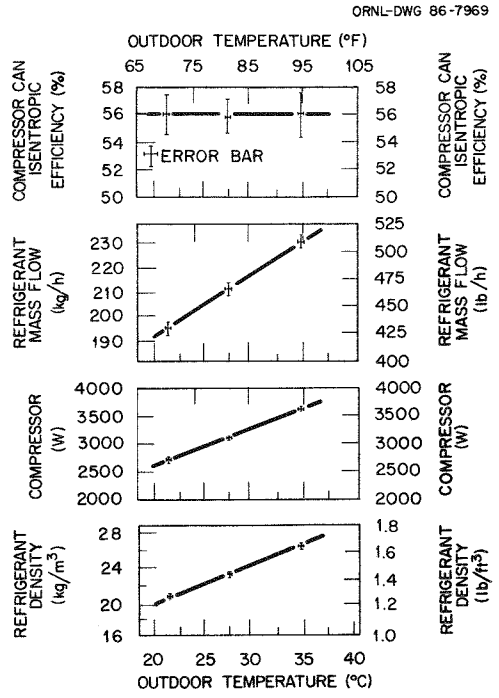

Fig. 7.3. Steady state performance traits.

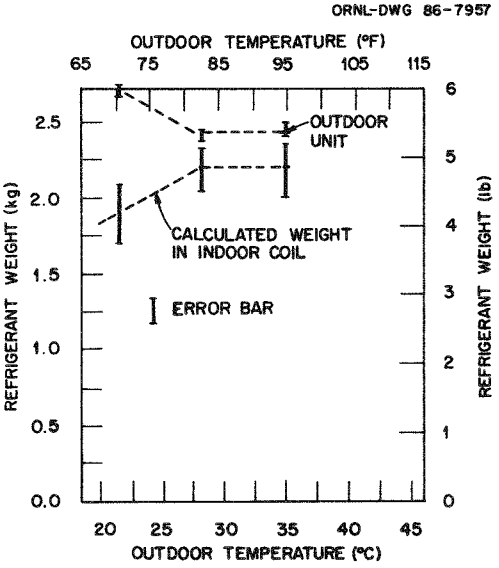

Fig. 7.4. Refrigerant weight distribution during steady state cooling mode operation.

superheat of refrigerant entering the compressor increased (as previously discussed). However, a redistribution of refrigerant did take place between the indoor and outdoor heat exchangers. At the lower outdoor air temperature of 21°C (70°F), the outdoor unit held 51% of the total charge and the indoor coil held 36.5%. With the accumulator dry, the redistribution of refrigerant likely was directed to the outdoor heat exchanger from the indoor coil. This result is reasonable as seen by the increased percentage of cool vapor in the indoor coil when there was lower outdoor air temperature.

7.2 HEAT PUMP DRY INDOOR COIL CYCLING OPERATION

The heat pump cooling mode cycling trends are analyzed to gain insight to the underlying causes of cycling that differ from those previously discussed in Sect. 5.3. Off- and on-cycle transients are reviewed for cycling tests conducted at 28°C (82°F) outdoor air temperature that have a 10-min-on and 20-min-off cycling rate. As in Sect. 5.3 the test heat pump had a refrigerant charge of 5.7 kg (12.5 lb) due to added instrumentation. The affect of refrigerant overchange on cycling efficiency is discussed in Appendix B.

7.2.1 Review of Cycling Transients during Heat Pump Off Cycle

At the start of the 20-min-off cycle, subcooled refrigerant was visually observed flowing for 48 s from outdoor unit to indoor unit through the liquid line. During this period 1.6 kg (3.5 lb) of refrigerant migrated to the indoor coil. The total time required to complete the off-cycle refrigerant migration was roughly 4 min. As previously discussed in Sect. 5.3, the rate of migration was observed to be directly related to wall temperatures of both heat exchangers. The indoor and outdoor heat exchanger wall temperatures changed roughly 14 C° (25F°) after only 2 min of shut down. The rapid increase in indoor coil temperature as viewed in Fig. 7.5 was due to latent heat

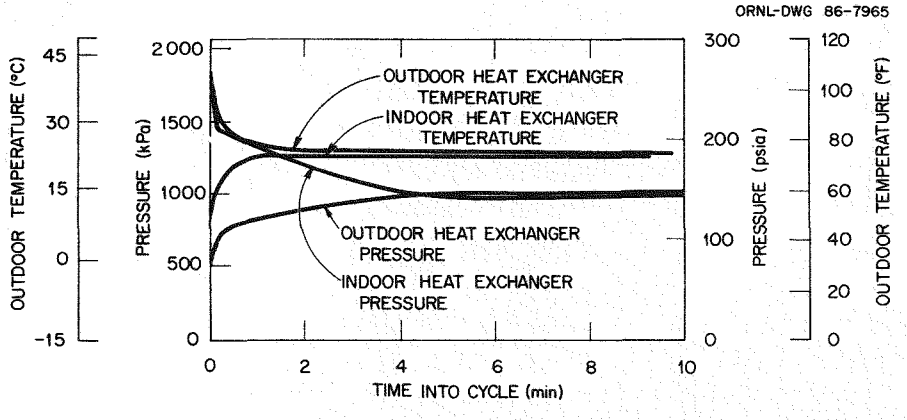

Fig. 7.5. Condenser and evaporator refrigerant temperatures and pressures observed during the off cycle of a 10-min-on and 20-min-off cooling mode cycling test conducted at 28°C (82°F) outdoor air temperature.

transfer from refrigerant migrating from the outdoor coil. High-side and low-side pressures (Fig. 7.5) equalized in 4 min, when refrigerant migration ceased (Fig. 7.6). During the off cycle (Fig. 7.6), a slight increase in weight of refrigerant was observed in the outdoor unit. The extra refrigerant was probably held in the accumulator; at the start of the off cycle, the accumulator was void of liquid refrigerant and then was visually observed to contain a 50.8-mm (2-in.) level of liquid refrigerant at the end of the off cycle.

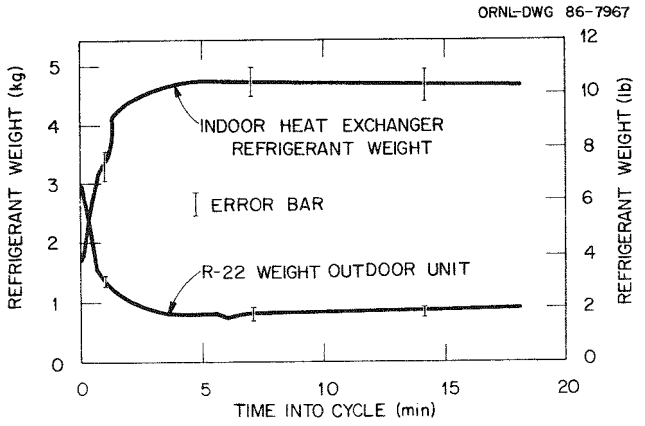

Fig. 7.6. Refrigerant weight distribution observed during the off cycle of a 10-min-on and 20-min-off cooling mode cycling test conducted at 28°C (82°F) outdoor air temperature.

7.2.2 Heat Pump Start-Up Transients

At the start of the on cycle, roughly 80% of the total refrigerant charge was in the indoor heat exchanger. Within 30 s of start-up, 2.86 kg (6.3 lb) of refrigerant was pumped by the compressor from the indoor to the outdoor coil. Observations of the accumulator show it to have filled with liquid refrigerant to within 76 mm (3 in.) of the accumulator top. The sharp increase in compressor power shown in Fig. 7.7 at 30 s into the on cycle indicates a high density of saturated refrigerant was being pumped by the compressor. However, as time progressed into the on cycle to 2 min of operation, the compressor power dropped due to a drop in evaporator pressure. This trend in pressure occurred because most of the refrigerant was still in the accumulator and was being metered to the compressor through the small oil return hole located at the bottom of the U-tube within the accumulator. As a result of these refrigerant dynamics at start-up, the cooling capacity gradually increased and did not reach steady state capacity until roughly 8 min of compressor operation.

With most of the refrigerant held in the accumulator during the first 2 min of start-up, both the indoor and outdoor heat exchangers were undercharged. This is seen in Fig. 7.8 by the drop in evaporator

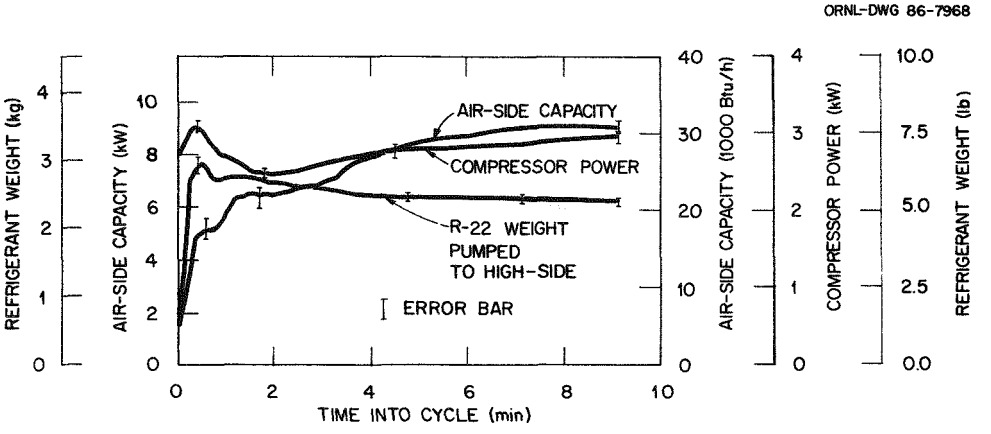

Fig. 7.7. Capacity, compressor power, and refrigerant pumped to high side during the on cycle of a 10-min-on and 20-min-off cooling mode cycling test conducted at 28°C (82°F) outdoor air temperature.

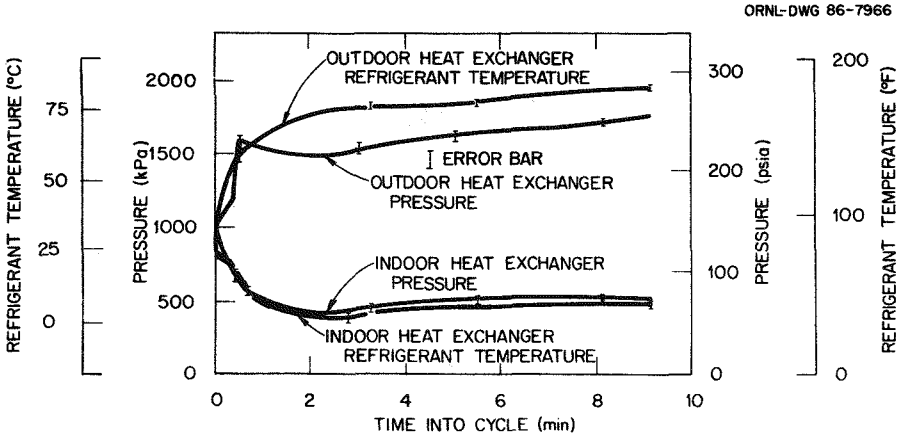

Fig. 7.8. Condenser and evaporator refrigerant temperatures and pressures observed during the on cycle of a 10-min-on and 20-min-off cooling mode cycling test conducted at 28°C (82°F) outdoor air temperature.

pressure and temperature as the compressor became starved for refrigerant. As a result, refrigerant mass flow decreased as evaporator pressure dropped and the refrigerant flow per unit work increased, causing the pronounced rise in condenser temperature (Fig. 7.8). As operating time progressed from 2 to 8 min, condensing pressure continued to increase as refrigerant was pumped from the accumulator. The accumulator was visually observed to be purged of liquid refrigerant after 7 min of compressor operation, with most of this refrigerant transferred to the outdoor coil. The distribution of refrigerant reveals that after the initial surge of 2.86 kg (6.3 lb) of refrigerant to the outdoor unit, roughly 0.91 kg (2 lb) of refrigerant returned to the indoor coil for establishment of steady state charge distribution (Fig. 7.9). Thus

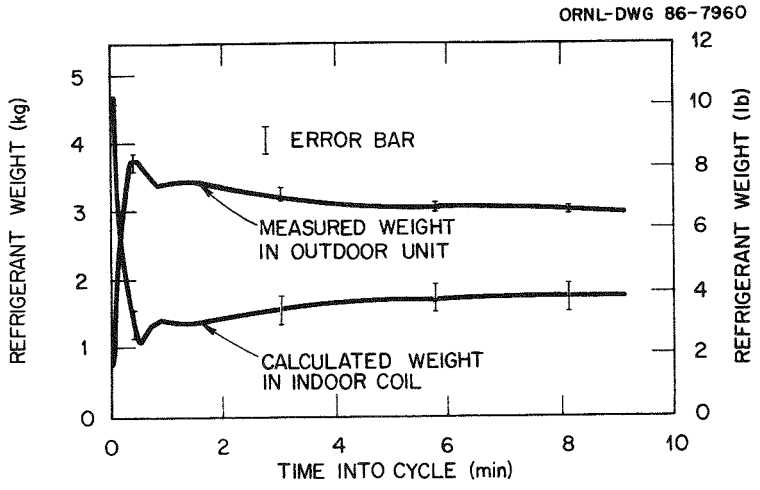

Fig. 7.9. Refrigerant weight distribution observed during the on cycle of a 10-min-on and 20-min-off cooling mode cycling test conducted at 28°C (82°F) outdoor air temperature.

roughly 1.8 kg (4 lb) of refrigerant was redistributed within the outdoor unit from the accumulator to the outdoor heat exchanger. With the refrigerant charge properly distributed, the discharge and suction refrigerant pressures gradually increased until steady state operation was reached.

7.2.3 Cycling as Affected by Outdoor Air Temperature

The cooling mode cycling efficiency was observed to improve as outdoor air temperature dropped for cycling rates of 25% on-time (10-min-on, 30-min-off). Over the range of load factors (Fig. 7.10), the difference in cycling efficiency is small.

Cooling mode cycling tests conducted at 28°C (82°F) outdoor air temperature with a cycling rate of 10-min-on and 20-min-off, revealed an increase in cycling efficiency as compared with similar cycling tests conducted at 35°C (95°F) outdoor air temperature. As outdoor air temperature increased, compressor suction pressure increased, resulting in a slight increase in refrigerant dynamic losses at start-up. As seen in Fig. 7.11, roughly an additional 0.45 kg (1 lb) of refrigerant was pumped from the indoor coil to the outdoor unit at the higher outdoor temperature of 35°C (95°F). As a result there was a further delay in reestablishing proper charge distribution to the outdoor and indoor heat exchangers. These trends occurred during the first 2 min of start-up (Fig. 7.11); however, after 2 min the total weight of refrigerant measured in the outdoor unit was the same for both outdoor air temperature cycling tests. Yet the distribution of refrigerant between the outdoor heat exchanger and accumulator varied for these tests. Observations revealed that the accumulator had a greater amount of liquid refrigerant just after start-up for the higher outdoor temperature cycling test.

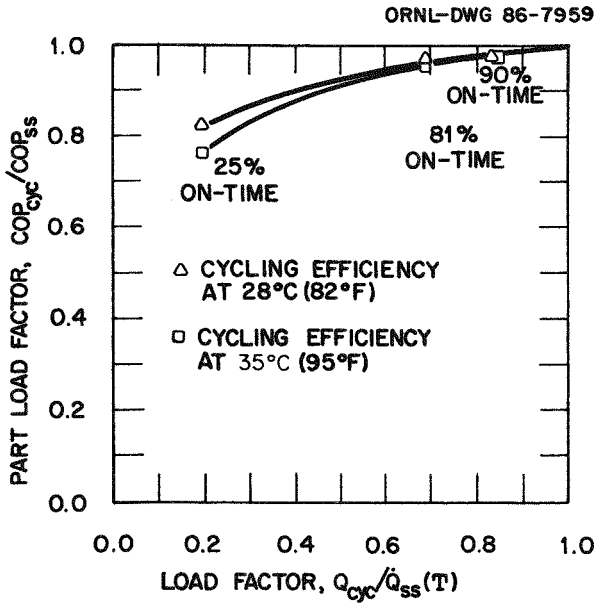

Fig. 7.10. Cooling mode cycling efficiency as affected by outdoor air temperature.

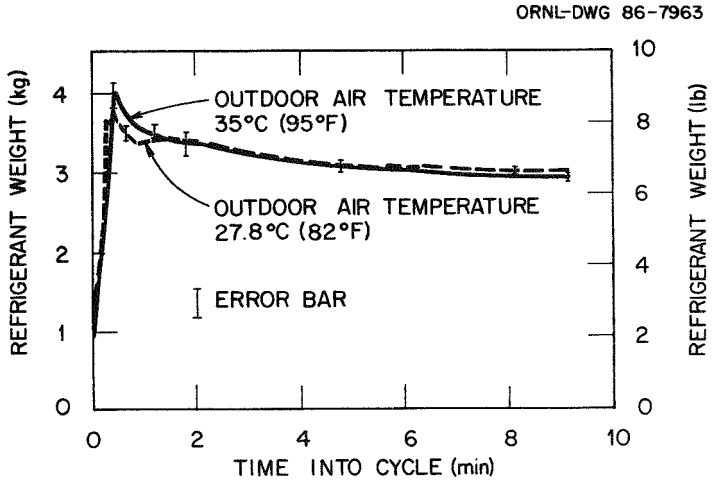

Fig. 7.11. Refrigerant weight measured in the outdoor unit for cycling tests conducted at 28°C (82°F) and 35°C (95°F) outdoor temperatures.

The results, although not severe in cooling mode operation, show similar trends to heating mode cycling test results. Duty cycle and refrigerant dynamics cause increased COP cycling degradation at the higher temperatures for a given mode of heat pump operation.

8. SEASONAL PERFORMANCE ANALYSIS

8.1 DEFINITION OF DYNAMIC LOSSES

The frosting of the tube and plate fin outdoor heat exchanger was observed to degrade heat pump efficiency only marginally, as previously discussed in Sect. 6.1. The test results indicate that cycling and defrosting losses are the major losses to efficient heat pump operation. However, frosting and defrosting are interdependent and are thus considered separately in the seasonal analysis, even though frosting losses are small.

The reductions in COP and capacity due to frosting, defrosting, and subsequent recovery from defrosting are defined by the shaded areas in Fig. 8.1. The frosting data used in seasonal analysis will include the recovery from reverse cycle defrosting. Defrosting will be defined as the interval from energizing to deenergizing of the reversing valve.

The cycling loss, as discussed in Sects. 5.3 and 7.2, results from a gradual rather than an instanteous rise in capacity as the heat pump cycles on. Separate from frosting and defrosting, cycling can be represented similarly to defrost recovery, which is the shaded area designated for recovery in Fig. 8.1. It should be noted here that the seasonal analysis of the cycling loss is based on performance data obtained

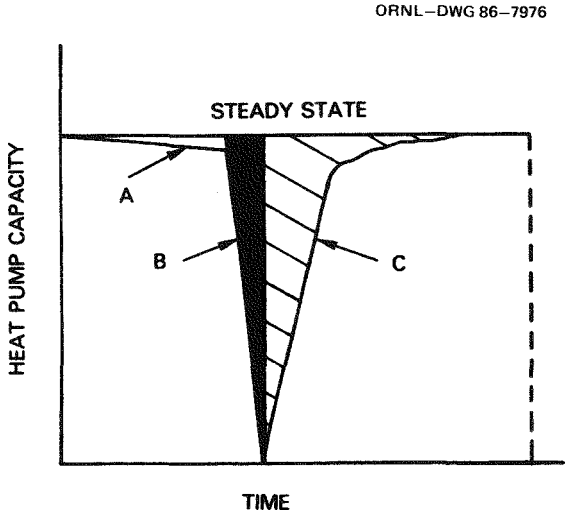

Fig. 8.1. Example of defined cumulative frosting-defrosting-recovery losses.

when the test heat pump is operating with the nameplate refrigerant charge of 3.40 kg (7.5 lb).

8.1.1 Seasonal Performance Code

The seasonal analyses were conducted using a seasonal performance computer code developed by Rice et al.[12] The computer model is currently available in FORTRAN IV and can be run on an IBM compatible personal computer. A complete documentation of the computer code is given in Oak Ridge National Laboratory Conservation Technology Report.[16]

For purposes of this study the model was used to evaluate the following:

1. A breakdown of heat pump energy consumption and operating cost on an annual basis,

2. The affect of climate on the magnitude of dynamic losses,

3. The affect of defrosting controls on frosting and defrosting yearly energy consumption,

4. The affect of heat pump sizing on the dynamic losses for various climatic regions, and

5. Energy and cost savings realized by minimizing the heat pump dynamic losses.

The nominal 9.7-kW (2 3/4-ton) air-to-air heat pump steady state and dynamic loss test data were incorporated into the seasonal performance model and applied to a "standard house" for various cities in the United States (Fig. 8.2). The standard house used for the analysis was a single-family detached residence, 167-m^2 (1800-ft^2) ranch style home that has a crawl space. Major axis of the house was oriented East-West. One air-change per hour at 24.2 km/h (15 mph) outdoor wind speed and 39°C (70°F) inside-outside temperature difference was assumed. Nominally 15% of the exterior surface area was single-glazed window. The ceilings were insulated to an R-19 level, the walls to an R-11 level, and the floors to an R-9 level. Using the above standard house, the heating and cooling loads were calculated for each of the cities listed in Fig. 8.2, with a weather data base obtained from the U.S. Air Force Engineering Weather Data manual.[17]

8.1.2 Frosting-Defrosting-Recovery Algorithms

The average COP and capacity, integrated over the frosting and recovery intervals, are plotted for the test heat pump operated with a demand defrost control (Fig. 8.3). These averaged values of COP and capacity were used to develop frosting loss coefficients that express

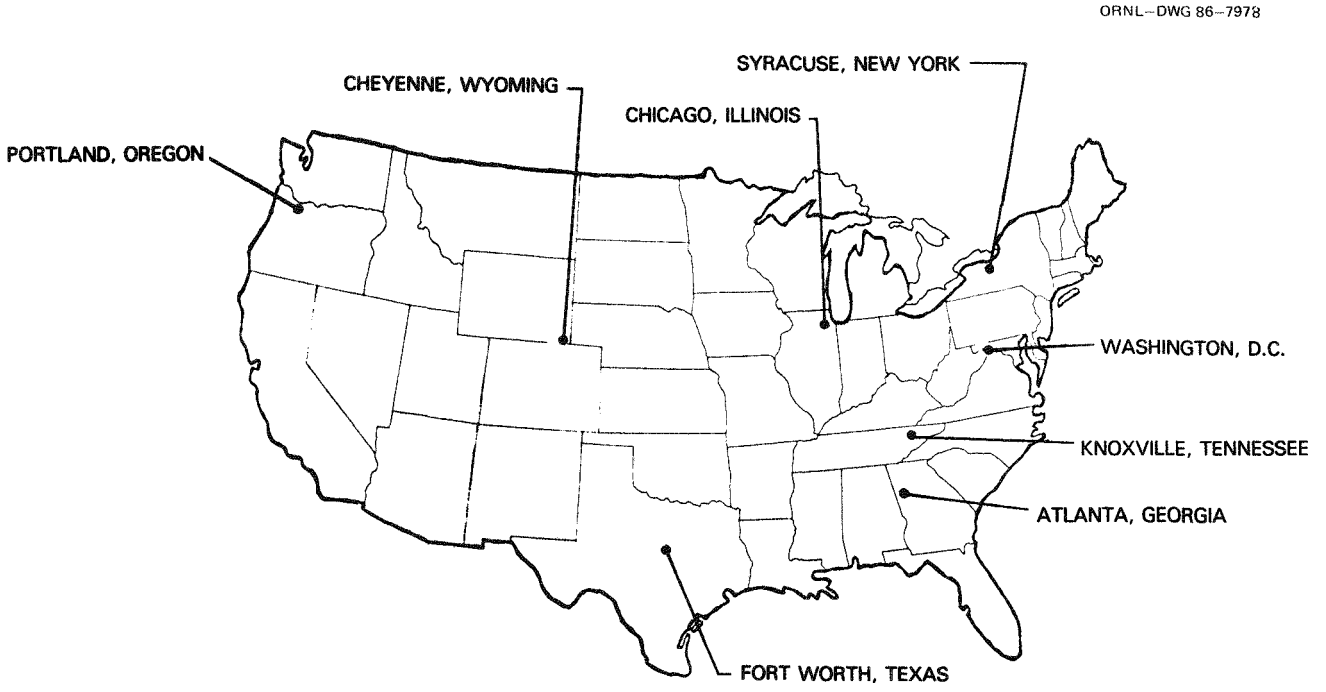

CITY, STATE	COOLING LOAD DESIGN CONDITIONS	
	97.5% DESIGN DAY TEMPERATURE (°F)	DESIGN LOAD (kBtu/h)
Fort Worth, Tex.	101.0	30.05
Atlanta, Ga.	92.0	24.44
Knoxville, Tenn.	92.0	24.04
Washington, D.C.	95.0	26.15
Portland, Oreg.	89.0	23.75
Chicago, Ill.	92.0	23.85
Syracuse, N.Y.	87.0	20.62
Cheyenne, Wyo.	86.0	20.11

Fig. 8.2. United States cities selected for the seasonal analysis of a 9.7-kW (2 3/4 ton) air-to-air heat pump installed in an 167-m^2 (1800-ft^2) house with HUD minimum insulation.

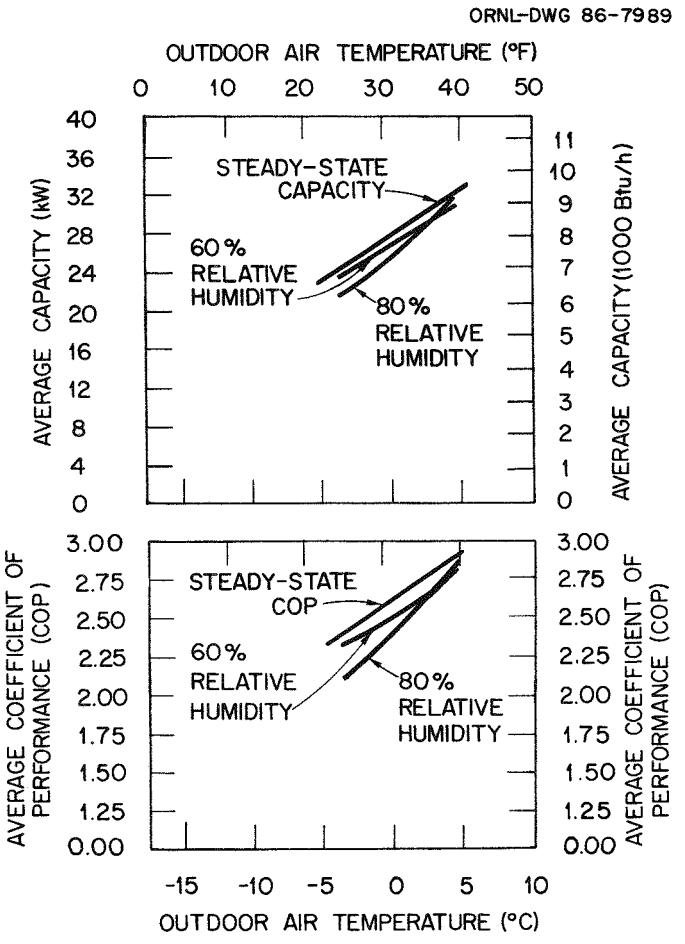

Fig. 8.3. Average frosting COP and capacity integrated over the frosting and recovery intervals.

the percentage loss in cumulative steady state capacity and COP. A complete listing of the averaged values of COP and capacity for the frosting, defrosting, and recovery intervals is tabulated in Appendix C for the heat pump operating with a demand defrost control and a time and temperature defrost control and is based on a 90- and 45-min timed cycle.

The averaged frosting COP and capacity (Fig. 8.3) for the test heat pump operating with a demand defrost control is lower than steady state values due primarily to the recovery cycle following defrost operation. For the range of outdoor air temperatures and 60% relative humidity (Fig. 8.3), the degradation due to frost accumulating on the outdoor coil was nominally 0.5%. However, the recovery from defrost further degraded the frosting loss by roughly 1.5%. This degradation, incurred due to recovery, increased for frost-defrost tests conducted at 70 and 80% outdoor relative humidity. As an example, for frost demand defrost tests conducted at -4.0°C (25°F) outdoor air temperature and 80%

relative humidity, the average frosting COP and capacity degraded 10.5 and 11%, respectively; however, the degradation due only to frost accumulating on the outdoor coil was 1% of steady state value.

The frosting loss coefficients, measured defrost average COP and capacity, frosting time, and defrost time (all listed in Appendix C) were incorporated in the seasonal performance computer code as functions of outdoor ambient temperature, relative humidity, and style of defrost control. Algorithms were developed from the frosting and defrosting data and they were coupled to a quadratic interpolation routine for use in calculating the breakdown of annual energy consumption.

8.1.3 Cycling Algorithms

Sections 5.3 and 7.2 addressed the cycling transients and the underlying causes of the cycling loss. For those tests the heat pump charge was 5.7 kg (12.5 lb), which is 2.3 kg (5.0 lb) more than nameplate charge, because of added line lengths for instrumentation. However the reduced cycling data, if used in the seasonal performance code, would overstate cycling losses because of the refrigerant overcharge (Appendix B). Heating and cooling mode cycling tests were repeated when the heat pump was operating with the nameplate charge of 7.5 lb (3.4kg).

These tests were conducted according to the DOE Test Procedures.[18] The multipoint reduced data were then used for the seasonal analysis breakdown of cycling losses according to methods developed by Kelly and Parkin.[4] It should be noted that this method selects on- and off-times that are implied for a thermostat model having a maximum of 3 cycles per hour at 50% on-time. Also an off-cycle parasitic, 40-W crankcase heater is included in the seasonal analysis breakdown of cycling losses.

8.2 ANNUAL HEAT PUMP ENERGY CONSUMPTION

The portions of total annual energy due to frosting,* defrosting,† cycling, off-cycle parasitics,‡ and back-up resistance heat** were calculated for the 9.7-kW (2 3/4-ton) test heat pump using weather data per

---

*Frosting losses include the indirect loss of auxiliary heat required to meet house load as caused by the increase of balance point due to frosting.

†Reverse cycle defrost losses include 5 kW of auxiliary heat used to temper chilled indoor air during defrost.

‡A 40-W crankcase heater is designated for off-cycle parasitics.

**Back-up resistance beat required to meet house load using steady state capacity as base.

respective U.S. city listed in Fig. 8.2. The portions of energy, expressed as a percentage of total annual heat pump operating energy, are listed in Table 8.1 for the test heat pump operating with demand and time-temperature defrost controls. Results in Table 8.1 reveal the magnitude of the dynamic losses to be roughly 15-20% of yearly energy used for various specified climatic regions in the United States. The breakdowns of frosting and defrosting energy consumption for the various defrost controls also reveal the advantage of the demand defrost logic.

8.2.1 Climate Affect on Heat Pump Energy Use

The portions of total energy used by frosting, defrosting, cycling, off-cycle parasitics, and supplemental resistance heat (Fig. 8.4 and Table 8.1) reveal for Fort Worth, Texas, the cycling loss as the major dynamic loss. These portions of energy (Fig. 8.4) were calculated for the test heat pump operating with a demand defrost control. For this city, the test heat pump is nominally 14% oversized, having a 1.14 cooling design factor (CDF), ratio of steady state cooling capacity to cooling load at the 97.5% design day temperature. Thus the total cycling losses including off-cycle parasitics are not overstated due to oversizing of the heat pump. The frosting-defrosting losses are 1.8% of total annual energy, while back-up resistance heat is only 0.9% of the total

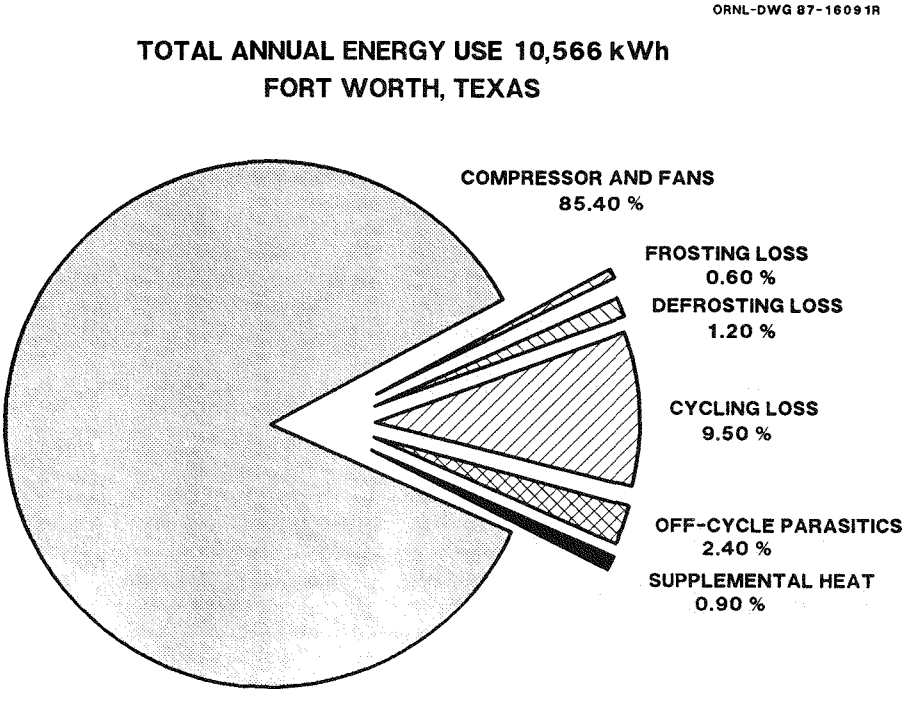

Fig. 8.4. Portions of energy as a percentage of total yearly energy for the test heat pump (with demand defrost initiator) operating in Fort Worth, Texas.

Table 8.1. Portion of energy expressed as a percentage of total annual heat pump operating energy

City and State	Defrost Control[a]	Ratio of Heating Load to Annual Load	Annual Back-up Heat[b] Usage (% of total)	Annual Energy Usage (% of total)					Total Annual Energy[e] (kWh)	Defrosts
				Frosting[c]	Defrosting	Cycling[d]	Off-cycle Parasitics	Dynamic Loss Total		
Fort Worth, Tex.	Demand	0.32	0.90	0.55	1.16	9.5	2.40	13.61	10566.0	183
	90 min		0.90	0.57	3.47	9.3	2.30	15.60	10822.0	519
	45 min		0.90	0.70	5.74	9.0	2.30	17.74	11098.5	1150
Atlanta, Ga.	Demand	0.51	2.40	1.10	1.96	10.20	2.80	16.06	9301.1	271
	90 min		2.30	1.06	5.92	9.80	2.70	19.48	9692.7	776
	45 min		2.20	1.15	9.73	9.40	2.60	22.88	10117.1	1708
Knoxville, Tenn.	Demand	0.58	2.50	1.26	2.20	10.90	2.80	17.16	9337.9	303
	90 min		2.40	1.16	6.85	10.40	2.70	21.11	9799.4	911
	45 min		2.30	1.27	11.20	9.90	2.50	24.87	10299.7	2013
Washington, D.C.	Demand	0.67	5.16	1.04	2.24	9.23	2.38	14.89	10499.9	350
	90 min		4.85	1.35	7.76	8.66	2.23	20.00	11173.8	1256
	45 min		4.56	1.83	12.62	8.15	2.10	24.70	11870.7	2783
Portland, Ore.	Demand	0.76	0.77	0.74	1.80	12.99	3.18	18.71	8467.4	236
	90 min		0.74	0.82	6.03	12.42	3.04	22.31	8858.5	928
	45 min		0.70	0.86	10.68	11.79	2.88	26.21	9328.4	2056
Chicago, Ill.	Demand	0.83	19.25	2.30	3.85	6.18	1.39	13.72	15546.4	855
	90 min		18.08	1.91	9.96	5.81	1.31	18.99	16553.1	2030
	45 min		16.86	1.77	16.03	5.42	1.22	24.44	17748.2	4406
Syracuse, N.Y.	Demand	0.84	19.94	2.47	3.69	6.09	1.42	13.67	15411.9	816
	90 min		18.67	1.98	10.14	5.70	1.33	19.15	16456.5	2007
	45 min		17.39	1.74	16.41	5.30	1.23	24.68	17668.2	4348
Cheyenne, Wyo.	Demand	0.85	23.06	1.70	1.54	5.92	1.30	10.46	16345.5	351
	90 min		21.64	1.50	7.68	5.56	1.20	15.94	17416.0	2134
	45 min		20.09	1.69	14.01	5.16	1.11	21.97	18763.4	4658

[a]Demand defrost initiated by air pressure drop across the outdoor coil. Time - temperature defrost initiated by table specified time and liquid line temperature.

[b]Auxiliary heat required to satisfy house heating load when heat pump operating below balance point. Does not include auxiliary heat (5 kW) attributed to reverse cycle defrost.

[c]Frosting includes recovery energy following defrost plus auxiliary heat consumed due to effect of frost on heat pump balance point.

[d]APF model assume no dependence of cycling to frosting/defrosting.

[e]Heat pump yearly energy consumption including back-up heat.

heat pump annual energy consumption. The small losses due to frosting, defrosting, and supplemental resistance heat are the results of the yearly load being predominantly cooling load, as seen by the ratio of heating load to yearly load (Table 8.1).

A similar breakdown of energy portions of supplemental heat and dynamic losses for Syracuse, New York, is shown in Fig. 8.5 and listed in Table 8.1 for the test heat pump operating with a demand defrost control. Here the relationship of dynamic loss and supplemental heat energies change dramatically as compared to those in Fort Worth, Texas. The CDF is 1.65 for the test heat pump applied to house loads data for Syracuse, New York; however, despite oversizing the heat pump, the cycling losses are only 6.1% of the total annual energy consumption. A hypothetical oversizing of 15% would have resulted in cycling losses of 3.5%. The frosting-defrosting losses, being 6.2% of total yearly energy, are greater than those observed for Fort Worth, Texas. The supplemental heat accounts for 20% of the total annual energy consumed by the test heat pump. Due to the large heating load, the energy usage of supplemental resistance heat is roughly equal to the dynamic loss energy for Syracuse, New York. The results indicate that further oversizing of the heat pump would decrease supplemental heat usage and improve annual

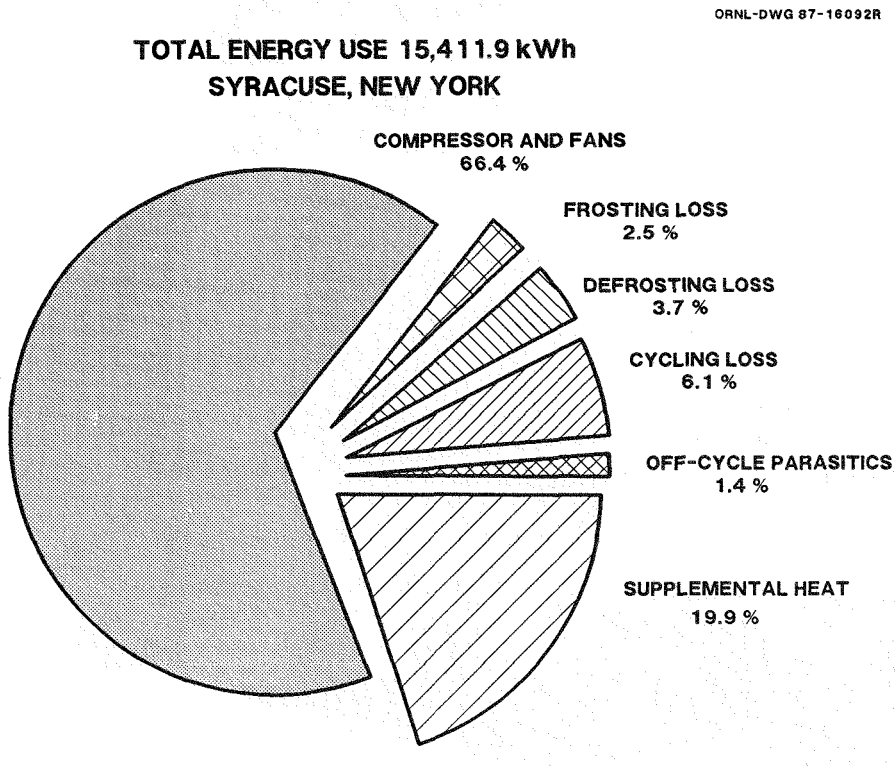

Fig. 8.5. Portions of energy as a percentage of total yearly energy for the test heat pump (with demand defrost initiator) operating in Syracuse, New York.

performance, although the amount of oversizing would need to be constrained by cooling mode comfort conditions.

8.2.2 Energy Consumption for Different Defrost Controls

The dynamic loss energy consumptions listed in Table 8.1 for the test heat pump operating with demand and time-temperature defrost controls are also displayed in Figs. 8.6 and 8.7 for Knoxville, Tennessee, and Syracuse, New York, respectively. These cities are representative

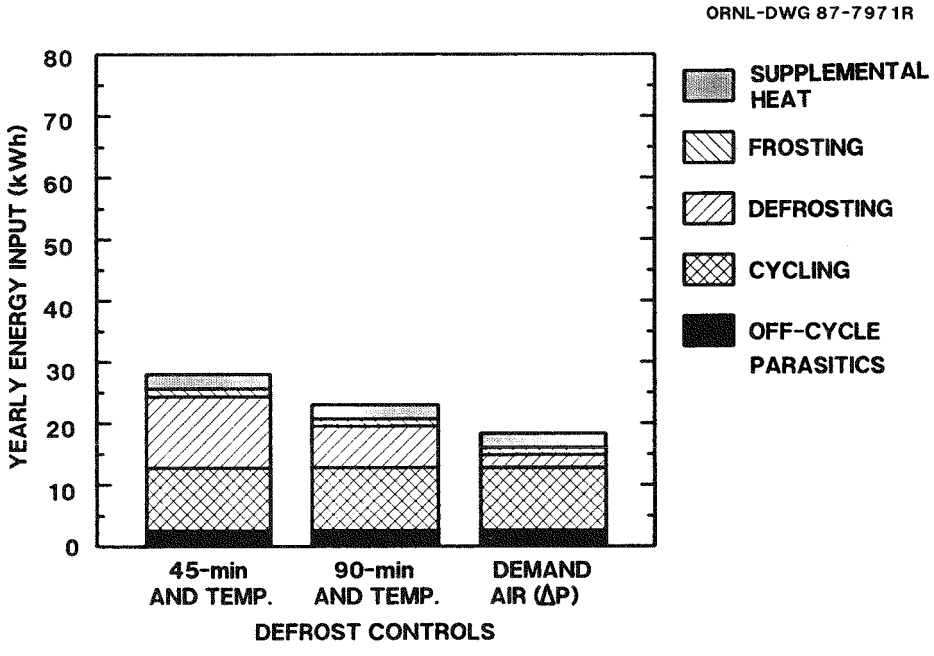

	KWH	KWH	KWH
OFF-CYCLE PARASITICS	257.5	264.6	261.5
CYCLING	1019.7	1019.1	1017.8
DEFROSTING	1153.6	671.3	205.4
FROSTING	130.8	113.4	117.7
SUPPLEMENTAL HEAT	236.9	235.2	233.4
DEFROST CONTROL	45 MIN	90 MIN	DEMAND

Fig. 8.6. Comparison of energy usage for a 9.7-kW (2 3/4 ton) heat pump using demand and time-temperature defrost controls as applied to Knoxville, Tennessee.

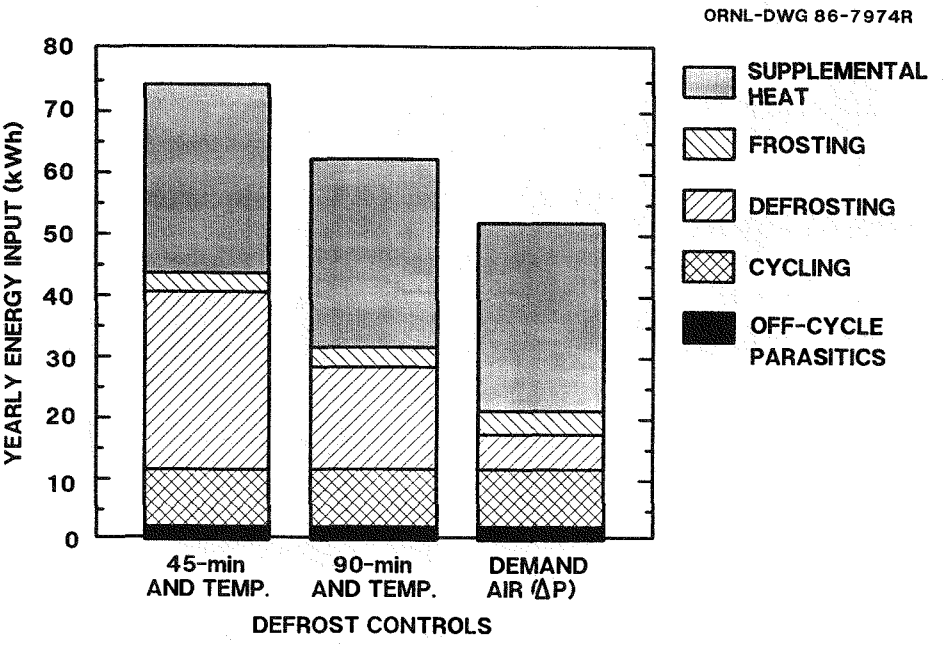

	KWH	KWH	KWH
OFF-CYCLE PARASITICS	217.3	218.9	218.8
CYCLING	936.4	938.0	938.6
DEFROSTING	2899.4	1668.7	568.7
FROSTING	307.4	325.8	380.7
SUPPLEMENTAL HEAT	3072.5	3972.4	3073.1
DEFROST CONTROL	45 MIN	90 MIN	DEMAND

Fig. 8.7. Comparison of energy for a 9.7-kW (2 3/4-ton) heat pump using demand and time-temperature defrost controls as applied to Syracuse, New York.

of climates having significant frosting-defrosting losses; the ratios of heating load to total load for Knoxville and Syracuse are 0.58 and 0.84, respectively. The seasonal analysis of frosting losses for the test heat pump operating in Knoxville showed frosting losses to be only 1.3% of total energy usage. The defrosting losses as seen in Fig. 8.6 increased as the defrosting control was changed from demand defrost control to a 45-min time and temperature defrost control. Demand defrosting contributed to 2.2% of the total annual energy, while the time-temperature defrosting using 90- and 45-min timed cycles contributed to 6.9% and 11.2%, respectively, of total annual energy.

Similar results are evident in the more severe winter climate of Syracuse, New York. Frosting of the outdoor coil contributed to nominally 2.2% of the total yearly energy consumed for the test heat pump operating in Syracuse. Demand defrosting accounted for 3.7% of total energy for the test heat pump (Fig. 8.7). Changing to the 45-min time-temperature, defrost control increased defrost energy usage to 16.4% of total energy.

The seasonal analysis results for Knoxville and Syracuse revealed the advantage of the demand defrost control in terms of total energy usage and therefore in terms of APF. As seen in Table 8.1 the difference in defrost losses for demand defrosting and 90-min time-temperature defrosting for the various listed cities was roughly 2 to 7% of total heat pump energy. The previous frost-defrost tests showed that the 90-min cycle allowed defrost operations too infrequently for ambient conditions less than 4.4°C (40°F) with relative humidities greater than 70%. Reducing the period would alleviate this problem; however, the seasonal efficiency would decrease because of the increase in defrost seasonal energy consumption discussed above. Also more frequent defrosting could increase wear on the compressor.

The seasonal analysis clearly showed the frosting-defrosting degradation to be due primarily to defrosting of the outdoor heat exchanger. Results indicate the demand defrost control yields best seasonal efficiency while maintaining system reliability under severe frosting conditions evident in Syracuse, New York, as an example.

8.2.3 Seasonal Reduction of Cycling Energy Consumption

The energy consumed due to cycling losses was nominally 8% of the total yearly energy consumption (Table 8.1). These cycling losses as calculated in the Seasonal Performance computer code are the true cycling losses unaffected by frosting-defrosting effects. Any affect of frosting and defrosting on cycling losses was charged to the frosting losses.

Previous discussion in Sect. 5.3.4 revealed potential improvement in cycling efficiency by controlling the migration of refrigerant during the off cycle. Seasonal analyses were conducted using reduced cycling data obtained for the test heat pump operating as follows:

Heating Mode:	Refrigerant isolated in the indoor coil during the off cycle and indoor blower operation extended 2 min into off cycle.
Cooling Mode:	Refrigerant isolated in the outdoor coil during the off cycle.

For cooling mode tests, the indoor blower was not extended into the off cycle as this would recirculate unwanted moisture on the evaporator coil back into the conditioned air space. Applying this cycling test data

for the test heat pump with refrigerant migration control, a comparison of seasonal energy losses was made to normal mode cycling seasonal energy losses. In Table 8.2 the yearly cycling losses are separated into cooling and heating season losses for the specified cities cited in Fig. 8.2. For each city the average cooling season and heating season percentage on-time was calculated for the 9.7-kW (2 3/4-ton) test unit having CDFs (Table 8.2). The cooling seasonal percentage on-time ranged from 30 to 40%, while the heating seasonal percentage on-time ranged from 35 to 60%. These on-times were calculated over only those times that had a load requirement.

On an annual basis, as seen in Table 8.2, cycling energy can be reduced by roughly 3 to 6% by means of a restrictor that inhibits

Table 8.2. Combined cycling and off-cycle parasitic energy consumption for the 9.7-kW (2 3/4-ton) test heat pump

Location	Cooling design factor[a]	Average On-Time		Balance point (°F)	Annual energy (% of total)	
		cooling (%)	heating (%)		Normal[b]	Migration control[c]
Fort Worth, Tex.	1.14	0.39	0.37	21.0	11.9	6.9
Atlanta, Ga.	1.41	0.34	0.40	22.5	13.0	7.4
Knoxville, Tenn.	1.43	0.30	0.39	22.0	13.7	8.1
Washington, D. C.	1.32	0.32	0.49	25.0	11.6	6.7
Portland, Ore.	1.43	0.36	0.33	26.0	16.2	9.5
Chicago, Ill.	1.44	0.34	0.58	27.0	7.6	4.4
Syracuse, N. Y.	1.65	0.34	0.57	27.0	7.5	4.5
Cheyenne, Wyo.	1.69	0.40	0.55	26.0	7.2	4.2

[a]Ratio of steady state capacity to ASHRAE design cooling load calculated at the 97.5% design day temperature.

[b]Off-cycle refrigerant migration occurs when heat pump deenergized.

[c]Refrigerant isolated in indoor coil (during off cycle) and indoor blower operation extended 2 min into off cycle, only for heating mode.

refrigerant migration during the off-cycle (i.e., no-bleed thermostatic expansion valve). These results for Fort Worth, Knoxville, and Syracuse reveal that energy savings due to reduced cycling losses are roughly half of normal mode cycling losses. Thus the use of a no-bleed type restrictor would result in energy savings of nominally 500 kWh per year. However, payback justification for the additional cost required for use of a no-bleed type restrictor is strongly dependent on regional electric rates.

8.3 HEAT PUMP ANNUAL OPERATING COSTS

The frosting, defrosting, and cycling portions of annual energy consumption need to be translated into their respective costs to determine incremental paybacks for improving heat pump efficiency. Energy costs based on electric rates taken from the federal report[19] were used to calculate annual operating costs for the test heat pump in the various cities. The electric rates are based on summer and winter costs per 2500 kWh (Table 8.3). These rates were used to calculate cost data listed in Tables 8.4 and 8.5 from the energy consumptions listed in Tables 8.1 and 8.2.

Heat pump annual operating cost, the annual energy cost of back-up heat, and cost breakdown of energy consumed by dynamic losses are listed in Table 8.4 for the test heat pump using demand and time-temperature defrost controls. The cost of energy consumed during cycling operation

Table 8.3. Typical electric rates as of January 1, 1987

Location	DOE region	Heat load ratio[a]	Cost $/2500 (kWh)	
			Winter	Summer
Fort Worth, Texas	6	0.32	122.26	173.94
Atlanta, Georgia	4	0.51	134.83	196.08
Knoxville, Tennessee	4	0.58	137.87	137.87
Washington, D.C.	3	0.67	148.41	210.03
Portland, Oregon	10	0.76	133.11	133.11
Chicago, Illinois	5	0.83	136.56	321.30
Syracuse, New York	2	0.84	157.51	157.51
Cheyenne, Wyoming	8	0.85	130.24	130.24

[a]Ratio of heating load to yearly load for a 167-m^2 (1800-ft^2) ranch style house having HUD minimum insulation.

Table 8.4 Annual cost breakdown of energy consumed by the test heat pump

City and State	Defrost control[a]	Ratio of heating load to annual load	Annual back-up heat[b] cost ($)	Annual cost[c] ($) of dynamic loss energy					Total energy cost[c] ($)
				Frosting[c]	Defrosting	Cycling[e]	Off-cycle parasitics	Dynamic loss total	
Fort Worth, Tex.	Demand	0.32	4.62	2.84	5.99	61.40	15.58	85.81	663.76
	90 min			3.02	18.360			98.36	676.29
	45 min			3.80	31.15			111.93	689.81
Atlanta, Ga.	Demand	0.51	11.96	5.52	9.83	61.82	17.72	94.89	609.77
	90 min			5.54	30.95			116.03	630.88
	45 min			6.27	53.09			138.90	653.77
Knoxville, Tenn.	Demand	0.58	12.94	6.49	11.33	56.02	14.48	88.32	514.97
	90 min			6.27	37.02			113.79	540.42
	45 min			7.21	63.62			141.33	568.01
Washington, D.C.	Demand	0.67	32.17	6.48	13.96	65.29	17.91	103.64	704.17
	90 min			8.95	51.47			143.62	744.17
	45 min			12.90	88.93			185.03	785.55
Portland, Ore.	Demand	0.76	3.49	3.34	8.16	58.56	14.32	84.38	450.84
	90 min			3.87	28.44			105.19	471.66
	45 min			4.27	53.04			130.20	496.68
Chicago, Ill.	Demand	0.83	163.44	19.53	32.69	68.86	17.90	138.98	1010.64
	90 min			17.27	90.06			194.09	1065.63
	45 min			17.26	155.41			259.43	1130.90
Syracuse, N.Y.	Demand	0.84	193.62	23.98	35.83	59.10	13.75	123.66	971.01
	90 min			20.53	105.13			198.51	1036.83
	45 min			19.37	182.67			274.89	1113.17
Cheyenne, Wyo.	Demand	0.85	196.33	14.48	13.11	50.44	10.90	88.93	851.54
	90 min			13.61	69.68			144.63	907.30
	45 min			16.52	136.95			214.81	977.50

[a]Demand defrost initiated by air pressure drop across the outdoor coil. Time - temperature defrost initiated by table specified time and liquid line temperature.

[b]Auxiliary heat required to satisfy house heating load when operating below balance point. Does not include auxiliary heat (5 kW) attributed to defrost.

[c]Costs based on winter and summer electric rates listed in Table 8.3.

[d]Frosting energy costs also includes recovery energy costs and auxiliary heat usage due to effect of frost on heat pump balance point.

[e]APF model assumes no dependence of cycling to frosting/defrosting.

Table 8.5. Annual cost breakdown of energy consumed during cycling operation. (Simulations for demand defrost control)

Location	Cooling design ratio[a]	Ratio of heating load to total load	Annual cost of energy due to cycling ($)	
			Normal[b]	Migration control[c]
Fort Worth, Tex.	1.14	0.32	77.00	44.03
Atlanta, Ga.	1.41	0.51	79.54	44.42
Knoxville, Tenn.	1.43	0.58	70.50	41.90
Washington, D.C.	1.32	0.67	83.20	44.53
Portland, Ore.	1.43	0.76	72.88	42.74
Chicago, Ill.	1.44	0.83	86.76	49.26
Syracuse, N.Y.	1.65	0.84	72.85	43.96
Cheyenne, Wyo.	1.69	0.85	61.34	35.52

[a]Ratio of steady state capacity to ASHRAE design cooling load capacity calculated at the 97.5% design day temperature.

[b]Off-cycle refrigerant migration occurs when the heat pump is deenergized.

[c]Refrigerant isolated in the outdoor coil during the off cycle. No extended indoor blower operation during cooling mode.

is given in Table 8.5 for assessing the potential cost savings realized through improved cycling efficiency.

For the cities listed in Table 8.4 having a ratio of heat load to total load less than 0.6, the cost of consumed energy for supplemental heat was less than $15 per year. For these same cities the cost of consumed dynamic loss energy was $100 per year, with cycling costs accounting for half the total. For cities such as Chicago, Syracuse, and Cheyenne, having heating load ratios greater than 0.6, the heat pump operating costs increased significantly. The cost of both supplemental heat and dynamic loss energy increased to $300 each per year. This was not the case, however, for Portland, Oregon, where it was observed that the major amount of bin hours were at outdoor ambient temperatures greater than 0°C (32°F) but less than 18.3°C (65°F), well above the heat pump balance point. A further review of the cost of energy consumed by cycling operation (Table 8.5) revealed that on an annual basis roughly $40 per year can be saved by installing a restrictor device that controls the migration of refrigerant when the heat pump cycles off.

The results shown in Tables 8.4 and 8.5 for the 9.7-kW (2 3/4-ton) test heat pump operating with a demand defrost control are displayed in Fig. 8.8 for comparison of heat pump operating costs in Fort Worth, Knoxville, and Syracuse. Total heat pump operating cost was greatest for Syracuse, New York, due to the required use of supplemental heat and

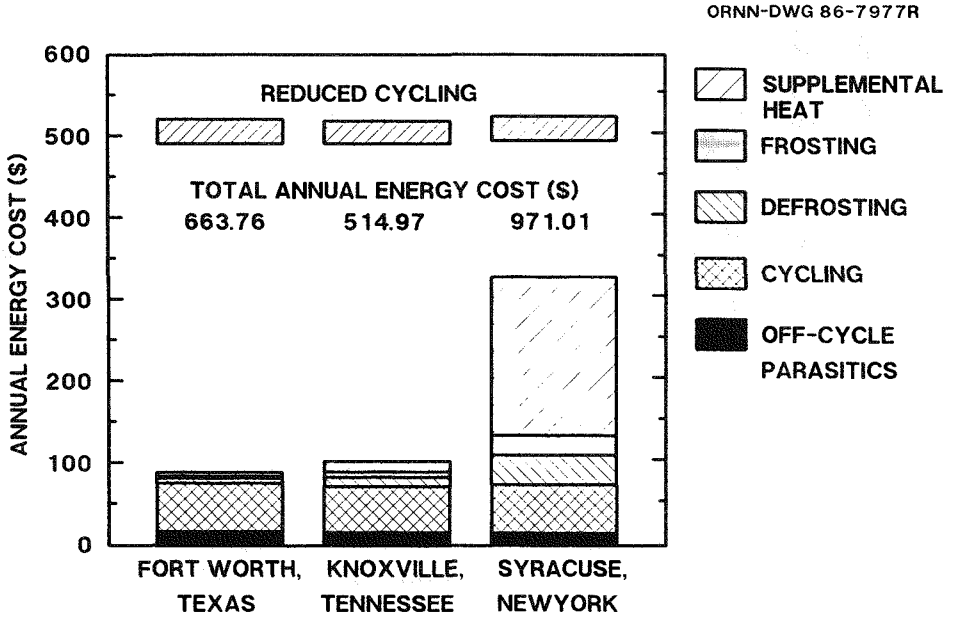

	$	$	$
OFF-CYCLE PARASITICS	15.58	14.48	13.75
CYCLING	61.40	56.02	59.10
REDUCED CYCLING	28.45	27.41	30.21
DEFROSTING	5.99	11.33	35.83
FROSTING	2.84	6.49	23.98
SUPPLEMENTAL HEAT	4.62	12.94	193.62
	FORT WORTH, TEXAS	KNOXVILLE, TENNESSEE	SYRACUSE, NEW YORK

Fig. 8.8. Yearly cost of supplemental heat and dynamic losses for a 9.7-kW (2 3/4-ton) heat pump installed in a 167-m^2 (1800-ft^2) house with HUD minimum insulation.

to the high utility rates. Knoxville has the lowest operating cost, due partly to the lower utility rates. Each bar chart in Fig. 8.8 reveals the potential savings through improved cycling efficiency. Extending the demand defrost interval for heat pump operation in Syracuse would improve payback potential to the consumer in New York. However, as previously stated, system reliability must not be compromised. Further research would be required to develop best defrost frequency in terms of cost savings, annual efficiency, and system reliability.

For comparison purposes, assuming the test heat pump operated with a 90-min time-temperature defrost control and incurred normal mode cycling losses, the 3-year payback affordable for a demand defrost initiator and a no-bleed restrictor would be as listed in Table 8.6. For Syracuse, if the 45-min rather than 90-min time-temperature defrost control was used for base of comparison, the affordable payback would increase to $427 per year. Thus in terms of a 3-year payback, the consumer could afford roughly $150 in Fort Worth and Knoxville for improved defrost and restrictor hardware. For the consumer in Syracuse the 3-year payback margin is even more attractive ($280) for the 9.7-kW (2 3/4-ton) test heat pump. These seasonal results reveal definite

Table 8.6. Cost premiums affordable for a 3-year payback of hardware usable for reducing dynamic losses

Location	Ratio of heating load to annual load	Dynamic Loss Reductions		Total Premium
		Frost-defrost[a] demand vs 90-min control	Cycling[b] no-bleed vs bleed throttle	
Fort Worth, Tex.	0.32	37.65	98.91	136.56
Atlanta, Ga.	0.51	63.42	105.36	168.78
Knoxville, Tenn.	0.58	76.41	85.80	162.21
Washington, D.C.	0.67	119.94	116.01	235.95
Portland, Ore.	0.76	62.43	90.42	152.85
Chicago, Ill.	0.83	165.33	112.50	277.83
Syracuse, N.Y.	0.84	197.55	86.67	284.22
Cheyenne, Wyo.	0.85	167.10	77.46	255.56

[a]Cost premium for reduction of frosting and defrosting losses based on demand defrost vs 90-min time and temperature initiators.

[b]Cost premium for cycling loss reduction based on control of refrigerant migration during the off cycle (heating and cooling) with 2 min delay in shutdown of indoor blower (heating only).

potential for improvement in heat pump design that would be affordable to the consumer.

8.4 AFFECTS OF HEAT PUMP SIZING ON ANNUAL PERFORMANCE FACTOR

All seasonal analyses were conducted by simply applying the 9.7-kW (2 3/4-ton) test heat pump to weather data for the various cities (Fig. 8.2). The ASHRAE design procedures imply that the heat pump should be sized to the design cooling load calculated at a design temperature that 97.5% of the time is greater than observed daily temperatures.[8] However such a sizing criterion does not always yield best APF for a given design of heat pump.

Steady state capacities and power consumptions (both heating and cooling), frosting, defrosting, and cycling capacities and power consumptions measured for the test heat pump (operating with demand defrost) were scaled to multiples or fractions of the cooling design load. It was assumed that the frosting and defrosting time intervals would be independent of size (i.e., frost accumulation proportional to coil size).

The plots of APF as functions of heat pump size (Fig. 8.9) show the 9.7-kW (2 3/4-ton) test heat pump to be close to best APF. For Fort Worth, sizing the heat pump to the design cooling load resulted in an APF of 2.13, while for the 2 3/4-ton test unit, the calculated APF was 2.11. In Knoxville, the hypothetical unit sized to cooling load resulted in an APF of 2.01; for the 9.7-kW (2 3/4-ton) test unit the APF

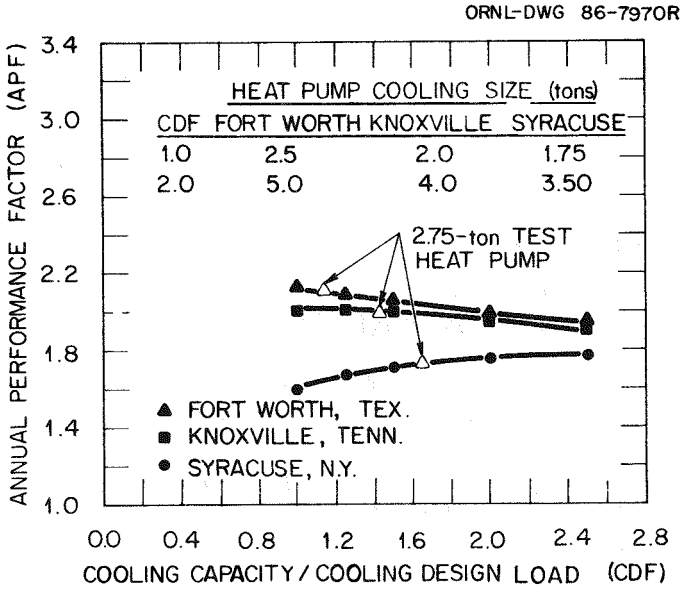

Fig. 8.9. Annual performance factor as a function of heat pump size.

was 2.0. As seen in Fig. 8.9, oversizing the test heat pump for these two cities causes a reduction of APF. This reduction occurred since the oversized heat pump will cycle more frequently, causing an increase in total annual energy consumption.

The trends of APF as a function of size for Syracuse differ from those trends for Knoxville and Fort Worth. In Syracuse, due to the higher heating load, increasing the size of the heat pump resulted in a decrease in the energy consumed by supplemental heat, although cycling losses did increase some.

8.5 COSTS AND ENERGY USAGE AS AFFECTED BY HEAT PUMP SIZING

Hypothetically sized heat pumps, having demand defrost control, were selected to the nearest quarter ton to meet the design cooling load and also to be double the design cooling load for Fort Worth, Knoxville, and Syracuse. These sizes of heat pumps listed in Fig. 8.9 were analyzed for comparison of the heat pump annual energy consumption (Fig. 8.10) and for comparison of heat pump operating costs (Fig. 8.11).

A 5-ton heat pump would use 8% more energy per year than a 2.5-ton heat pump, sized to cooling load, in Fort Worth. The increased energy consumption as seen in Fig. 8.10 is the result of increased on-off cycling. Including off-cycle parasitics, the increase in cycling energy consumption is 950 kWh per year for the 5-ton heat pump as compared with the 2.5-ton unit. In terms of additional cost this translates into $60 additional cost per year for operating the 5-ton unit in Fort Worth (Fig. 8.11).

For Knoxville, Tennessee, increasing the size of the hypothetical heat pump from 2 to 4 tons nearly doubled annual cycling energy consumption. However this increase in cycling energy usage was offset by the decrease in supplemental heat energy consumption (Fig. 8.10). Thus for Knoxville, having a heating load to annual load of 0.58, the range of sizes had slight affect on APF.

Sizing the heat pump to twice the cooling load (3.50-ton cooling capacity) for Syracuse, New York, resulted in a significant decrease in energy consumed by supplemental heat as compared with that of the 1.75-ton unit, sized to design cooling load. As evident in Fig. 8.10, the 3.5-ton unit required only 2120 kWh per year of supplemental heat; for the 1.75-ton unit roughly 6600 kWh per year of supplemental heat was needed to satisfy the house load. For this northern climate of Syracuse, the consumer would save $104 per year by selecting the 3.5-ton unit rather than the 1.75-ton unit (Fig. 8.11). However, doubling the size of the unit would also roughly double the initial cost, which would increase the payback period.

The results displayed in Figs. 8.10 and 8.11 reveal that a heat pump should be sized to cooling design load for those mild climates that are predominantly cooling load. Using this design criteria developed by

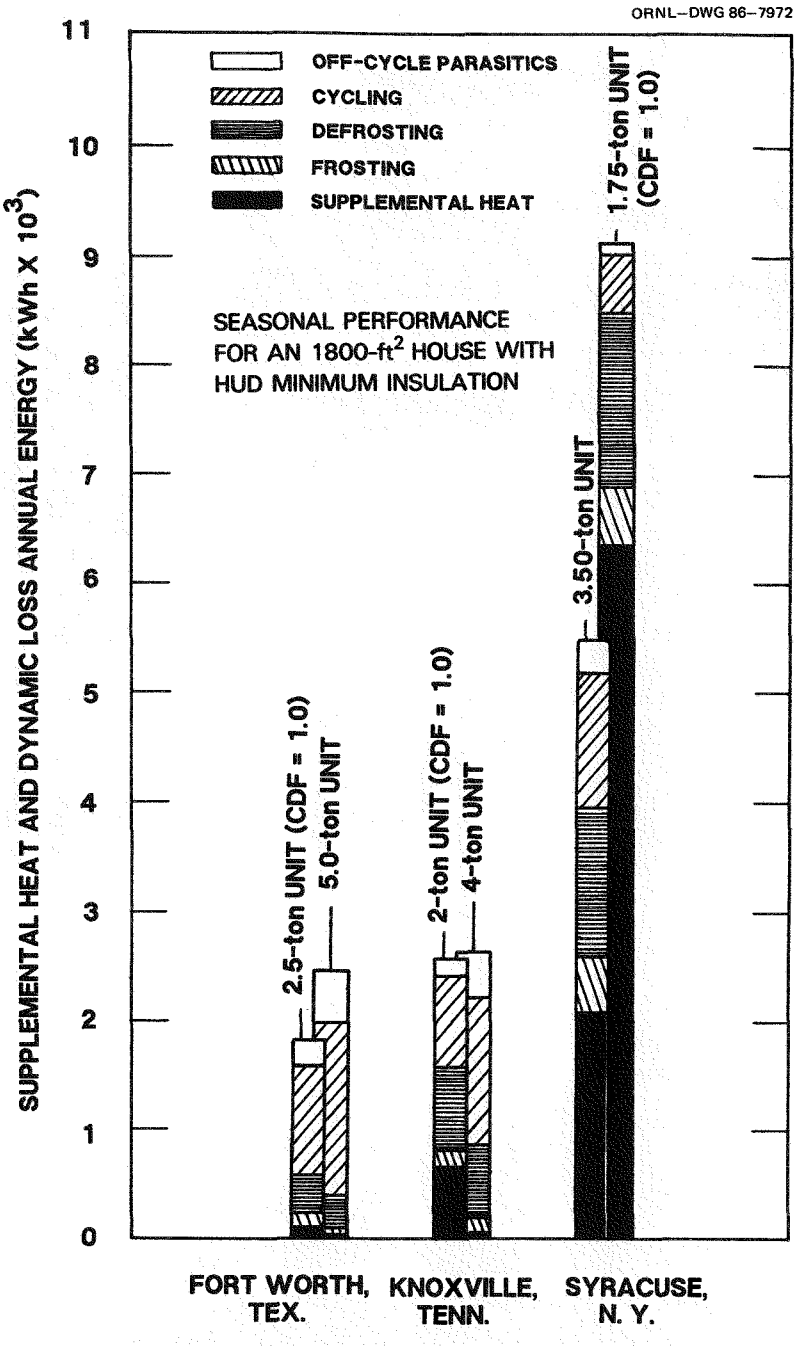

HEAT PUMP ANNUAL ENERGY USAGE (kWh)

CDF	FORT WORTH	KNOXVILLE	SYRACUSE
1.0	10,417.8	9,237.4	16,828.3
2.0	11,269.9	9,635.6	15,168.0

Fig. 8.10. Energy consumption for a heat pump sized to design cooling load as compared with that of a heat pump sized to twice the design cooling load.

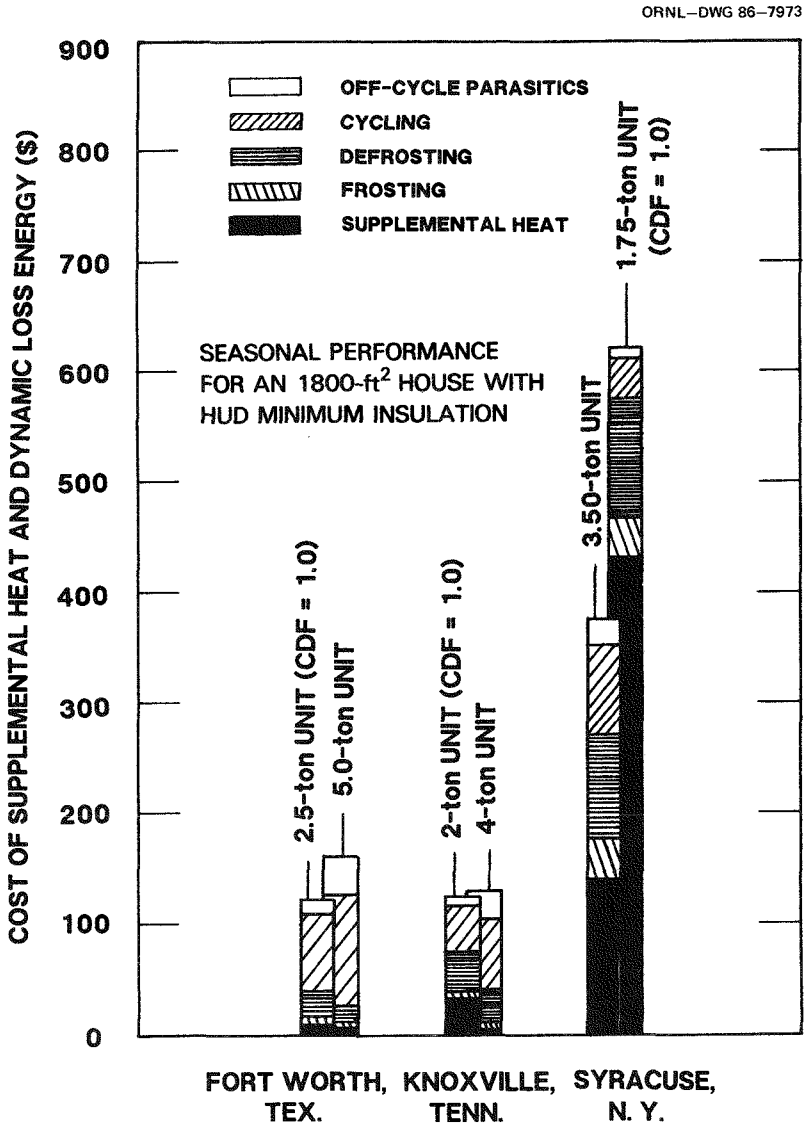

HEAT PUMP ANNUAL OPERATING COST ($)

CDF	FORT WORTH, TEXAS	KNOXVILLE, TENNESSEE	SYRACUSE, NEW YORK
1.0	654.00	509.00	1060.00
2.0	708.00	532.00	955.00

Fig. 8.11. Yearly cost breakdown for a heat pump sized to design cooling load as compared with that of a heat pump sized to twice the design cooling load.

ASHRAE, the heat pump will be sized for best APF and for summer comfort conditions. However, for the northern climates, the ASHRAE design criteria are inadequate. Data in Fig. 8.9 indicate that for northern climates (such as Syracuse, New York) the unit should be sized to near maximum APF, roughly 1.75 to 2.00 times the design cooling load. Again the oversizing should be constrained by summer comfort criteria and initial cost. Further research on the affect of heat pump oversizing on summer indoor humidity control would help establish proper heat pump sizing criteria for North American climates.

REFERENCES

1. Domingorena, A. A., *Performance Evaluation of a Low-First-Cost, Three-Ton, Air-to-Air Heat Pump in the Heating Mode*, ORNL/CON-18, Oak Ridge National Laboratory, October 1978.

2. Domingorena, A. A., *Performance Evaluation of a Selected Three-Ton Air-to-Air Heat Pump in the Heating Mode*, ORNL/CON-34, Oak Ridge National Laboratory, January 1980.

3. Miller, W. A., *Laboratory Evaluation of the Heating Capacity and Efficiency of a High-Efficiency, Air-to-Air Heat Pump with Emphasis on Frosting/Defrosting Operation*, ORNL/CON-69, Oak Ridge National Laboratory, December 1982.

4. Kelly, G. E., and Parkin, W. H., *Factors Affecting the Performance of a Residential Air-to-Air Heat Pump*, ASHAE Transactions Part 1, 1977, pp. 839-849.

5. Tanaka, N., and Yamanaka, G., *Experimental Study on the Dynamic Characteristics of a Heat Pump*, ASHRAE Transactions 88, Part 2, 1982, pp. 323-331.

6. Mulroy, W. J., and Didion, W. A., *A Laboratory Investigation of Refrigerant Migration in a Split Unit Air Conditioner*, NBSIR 83-2756, 1983, U.S. Department of Commerce, National Bureau of Standards.

7. Murphy, W. E., and Goldschmidt, V. E., *Transient Response of Air Conditioners - A Qualitative Interpretation Through a Sample Case*, ASHRAE Transactions 90, Part 1B, 1984, pp. 997-1008.

8. ASHRAE Handbook, Equipment Volume, *Unitary Heat Pumps and Packaged Terminal Heat Pumps: Equipment Design and Selection*, pp. 44.4, 1983.

9. AMCA Standard 210-67, *Test Code for Air Moving Devices*, Air Moving and Conditioning Association, Inc., 1967.

10. Miller, G. N., and Spille, R. F., *Test and Evaluation of Five Electronic Differential Pressure Transmitters*, 1979, IR-PE-63.

11. Kline, S. J., and McClintock. *Describing Uncertainties in Single-Sample Experiments*, Mech. Eng., pp. 3, January, 1953.

12. ASTM STP-15-C-1967. *Presentation of Data and ± Limits of Accuracy of an Observed Average.*

13. Mulroy, W. J., and Didion, D. A., 1985, *Refrigerant Migration in a Split-Unit Air Conditioner*, ASHRAE Transactions Part 1A, pp. 193-206.

14. Miller, W. A., *Frosting Experiments for a Heat Pump Having a One-Row Spine-Fine Outdoor Coil*, ASHRAE Transactions Vol. 90, Part 1 pp.

15. Hubert, M. C., and Benser, W. A. 1951. "Some stall and surge phenomena in axial flow compressors", Vol. 73, pp. 835.

16. Rice, C. K., Fischer, S. K., and Emerson, C. J., *The Oak Ridge Heat Pump Models: II. An Annual Performance Factor/Loads Model for Residential Air-Source Heat Pumps*, ORNL/CON-160 (in preparation).

17. Departments of the Air Force, Army, and Navy. 1978. *Engineering Weather Data*, AFM 88-29, TM5-785, NAVFAC P-89, July 1.

18. Department of Energy, *Test Procedures for Central Air Conditioners, Including Heat Pumps*, 10CFR Part 430, Federal Register, Vol. 44, No. 249, pp. 76700-76723, December 1979.

19. Department of Energy, *Typical Electric Bills*, DOE/EIA-0040(85).

Appendix A

STEADY STATE HEATING AND COOLING MODE PERFORMANCE DATA

Appendix A

STEADY STATE HEATING AND COOLING MODE PERFORMANCE DATA

Tabulation of heating-mode and cooling-mode performance data observed during steady state operation is presented in Tables A.1 and A.2, respectively. Refrigerant weight in the indoor heat exchanger was calculated by subtracting measured weight in the outdoor unit from the heat pump total charge less refrigerant in vapor and liquid lines. The refrigerant charge for these heating and cooling mode steady state tests was 5.7 kg (12.5 lb), which is 2.3 kg (5.0 lb) more than nameplate charge. The additional charge was needed due to added line lengths required for later cycling phenomena testing. This overage of charge did not affect steady state COP and capacity, because manufacturer charging criteria of superheat at inlet to the compressor for given high and low side pressures were adhered to. Outdoor airflows were monitored at times other than those listed in the tables. The location of refrigerant temperature and pressure sensors is shown in Fig. 2.1 of the main text.

Table A.1. Performance data for heating mode steady state tests

	1985 DATE					
	6/31	6/9	6/16	6/17	6/20	6/20
	Air Temperature (°F)					
Outdoor coil						
In	59.9	50.7	40.1	35.8	25.7	20.4
Out	48.9	41.5	32.6	29.2	20.7	16.2
Indoor coil						
In	69.7	70.2	70.3	70.3	70.3	69.8
Out	101.4	97.9	93.6	92.3	88.2	85.9
	Refrigerant Temperature (°F)					
Compressor						
In	47.6	30.5	22.9	19.9	12.6	8.8
Out	185.7	165.8	156.9	152.7	145.7	143.9
Reversing valve, out	181.5	160.3	150.3	145.7	137.2	134.9
Condenser						
In	167.1	147.9	137.3	132.7	122.1	118.3
Out	87.4	90.7	94.7	93.7	89.5	87.1
Liquid line vapor line HX, in	78.8	78.7	80.3	78.5	72.8	69.6
Outdoor capillary, in	75.9	71.1	70.3	68.7	63.9	61.0
Evaporator						
In	48.5	42.1	34.8	31.8	23.9	19.5
Out	40.7	33.5	25.9	22.9	15.4	11.5
Accumulator						
In	43.4	32.1	24.6	21.6	14.9	11.0
Out	44.1	30.9	23.6	20.6	13.5	9.7

Table A.1. (Continued)

	1985 DATE					
	6/31	6/9	6/16	6/17	6/20	6/20
	Refrigerant Pressures (PSIA)					
Compressor						
In	78.5	70.3	61.7	58.6	51.1	47.6
Out	240.3	221.1	204.9	200.8	187.7	181.2
Reversing valve, out	238.4	219.6	203.8	199.8	186.9	180.3
Condenser						
In	236.8	217.9	202.7	198.7	185.9	178.5
Out	234.8	216.1	200.9	196.9	184.7	177.5
Outdoor capillary, out	213.9	198.0	183.4	176.9	162.6	155.8
Evaporator						
In	97.0	87.7	77.7	73.8	64.1	59.3
Out	81.7	73.4	64.7	61.6	53.8	50.1
Accumulator, in	81.5	72.2	63.7	60.6	52.9	49.3
	Air Pressure Drop (in. H_2O)					
Indoor unit static	0.66	0.66	0.66	0.66	0.68	0.67
Outdoor coil total	0.28	0.31	0.32	0.32	0.34	0.36
	Refrigerant Weight (lb)					
Outdoor unit	1.53	2.67	3.57	3.97	4.48	5.01
Indoor coil[a]	8.49	7.37	6.49	6.09	5.58	5.05

Table A.1 (Continued)

	1985 DATE					
	6/31	6/9	6/16	6/17	6/20	6/20
			Flow Rates			
Air flow cfm						
Outdoor[b]	2,550.0	2,500.0	2,540.0	2,482.7	2,463.6	2,456.6
Indoor	1,279.5	1,262.9	1,276.5	1,278.7	1,292.9	1,298.5
Refrigerant mass flow, lb/h	451.4	413.5	340.0	319.4	261.8	233.7
			Power (W)			
Outdoor fan	265.9	272.5	272.3	272.9	280.2	282.5
Indoor blower	530.6	545.2	543.4	538.2	547.2	547.7
Compressor	2,936.0	2,674.5	2,426.3	2,497.7	2,140.0	2,028.2
			Measures of Performance			
Capacity (Btu/h)						
Refrigerant side	42,349.0	37,261.1	30,020.6	28,149.5	23,370.2	21,140.4
Air Side	41,012.7	36,575.8	30,945.3	29,020.0	24,091.2	21,194.0
COP						
Refrigerant side	3.32	3.13	2.71	2.49	2.312.17	
Air side	3.30	3.07	2.80	2.57	2.382.23	
Compressor isentropic efficiency %	53.1	53.0	50.5	47.5	48.146.7	

[a]Indoor coil refrigerant weights are calculated values.

[b]Outdoor cfm was measured separately from steady state data. Measurements of cfm were taken from the start of frosting tests conducted at similar outdoor temperatures.

Table A.2. Performance data for cooling mode steady state tests

	1985 Date		
	7/15	7/15	7/18
	Air Temperature (°F)		
Outdoor coil			
In	94.9	81.6	70.5
Out	113.5	98.6	86.2
Indoor coil			
In	81.1	81.4	81.5
Out	59.5	59.8	61.3
	Refrigerant Temperatures (°F)		
Compressor			
In	64.2	68.6	69.3
Out	218.4	209.8	200.4
Reversing valve, out	215.8	207.2	198.3
Condenser			
In	209.8	201.2	192.1
Out	103.9	89.9	77.7
Indoor capillary, in	97.5	86.1	76.7
Evaporator			
In	57.3	52.1	46.8
Out	52.2	59.0	62.9
Reversing valve			
In	56.2	63.2	65.8
Out	61.0	67.2	69.2
Accumulator, out	63.1	68.6	69.9
	Refrigerant Pressures (PSIA)		
Indoor			
Compressor			
In	94.8	85.6	77.3
Out	317.4	268.3	229.5
Condenser			
In	317.0	268.2	229.4
Out	314.3	265.8	227.3
Capillary, in	288.5	244.3	209.2
Evaporator			
In	110.8	101.5	92.9
Out	99.2	90.3	81.5

Table A.2 (Continued)

	1985 Date		
	7/15	7/15	7/18
Reversing valve			
In	98.8	87.8	80.8
Out	96.8	87.6	79.2
Air Pressure Drop (in. H_2O)			
Indoor unit static	0.82	0.82	0.80
Outdoor coil total	0.189	0.214	0.235
Refrigerant Weight (lb)			
Outdoor unit	5.38	5.57	5.95
Indoor coil[a]	4.81	4.60	4.21
Flow Rates			
Airflow, cfm			
Outdoor[b]	2,550.0	2,550.0	2,550.0
Indoor	1,285.7	1,294.3	1,303.2
Indoor condensate, lb/h	3.5	4.7	5.3
Refrigerant mass flow, lb/h	508.3	466.9	430.7
Power (W)			
Outdoor fan	244.6	246.4	249.5
Indoor blower	522.5	527.1	551.4
Compressor	3,611.2	3,100.6	2,737.9
Measures of Performance			
Capacity, Btu/h			
Refrigerant side	34,226.1	33,744.9	32,640.7
Air side	34,659.3	33,628.5	32,244.0
COP			
Refrigerant side	2.29	2.55	2.70
Air side	2.32	2.54	2.67
Compressor isentropic efficiency %	53.72	55.80	56.14

[a]Indoor coil refrigerant weights are calculated values.

[b]Outdoor coil was measured separately from steady state data. Measurements of cfm were taken from the start of frosting tests conducted at similar outdoor temperature.

Appendix B

AFFECT OF REFRIGERANT OVERCHARGE ON HEAT PUMP CYCLING EFFICIENCY

Appendix B

AFFECT OF REFRIGERANT OVERCHARGE ON HEAT PUMP CYCLING EFFICIENCY

Heating mode and cooling mode cycling tests were conducted by varying any one of the three parameters of on-time, off-time, or outdoor air temperature, while holding the other two variables fixed. The investigation of the affect of each parameter on cycling transients revealed its effect on the underlying mechanisms causing the cycling loss. Sections 5.3 and 7.2 addressed the cycling transients observed during the on and off cycle of the test heat pump. Both heating and cooling mode laboratory test results indicated that the migration of refrigerant during the off cycle resulted in an overfilling of the accumulator at start-up, which left the condenser and evaporator of the heat pump starved for refrigerant. Since the refrigerant, temporarily held in the accumulator, had to be pumped by the compressor through the oil-return hole at bottom of the U-tube, there was a time delay in establishing proper charge distribution, which caused most of the cycling loss. For these cycling tests, the heat pump was operated with a refrigerant charge of 5.7 kg (12.5 lb), which was 2.3 kg (5 lb) in excess of the manufacturers recommended amount. This overcharge was needed to fill the added lengths of refrigerant tubing necessary for instrumentation. A further study of cycling, conducted with the heat pump operating with the nameplate charge of 3.4 kg (7.5 lb) (extra line lengths removed) revealed that the refrigerant overcharge of 2.3 kg (5 lb) degraded cycling efficiency. Cycling trends for the separate tests conducted at nameplate charge and at 2.3 kg (5 lb) overcharge are similar; however, the time dependent transients and losses are less for tests at nameplate charge. The cycling test results that follow reveal the affect of the 2.3 kg (5 lb) of refrigerant overcharge on the cycling efficiency of the test heat pump.

Cycling COP is based on air-side measurements and is calculated using Eq. (1). Off-cycle crankcase heater energy is not included unless otherwise specified.

$$COP_{cyc} = \frac{Q_{on} + Q_{off}}{E_{total}} , \qquad (1)$$

where

Q_{on} = Integrated indoor coil heat output measured on the air-side during the on period,

Q_{off} = Integrated indoor coil heat output measured on the air-side during the off period,

E_{total} = Integrated energy consumption of compressor and fans during total cycle.

The part-load factor (PLF), ratio of cycling COP to steady state COP, is plotted in Fig. B.1 as a function of the load factor [defined by Eq. (2)] for heating and cooling mode cycling tests.

$$LF = \frac{Q_{cyc} + Q_{off}}{(\dot{Q}_{ss}\, T_{cyc})}, \qquad (2)$$

where

Q_{ss} = steady state capacity,

T_{cyc} = period of the on plus off cycle.

The multipoint data per curve in Fig. B.1 were reduced from cycling test data for the heat pump operating with nameplate charge and with the heat pump operating with 12.5 lb (5.7 kg) of refrigerant charge. These curves in Fig. B.1 were developed using a technique first developed by Parken and Kelly.[4] Test data per curve were reduced from cycling tests with selected on- and off-times that are implied from a thermostat model having a maximum 3 cycles per hour (CPH) at 50% on-time (on period/T_{cyc}). It is assumed that cycling rate is dominated by thermostat dynamics. Therefore each curve represents heat pump cycling COP as related to the house load and cycling rate.

The heating mode cycling efficiency for the 6-min-on, 24-min-off DOE cycling tests conducted at 8.3°C (47°F) outdoor air temperature was degraded by 10% due to the 2.3 kg (5 lb) of refrigerant overcharge

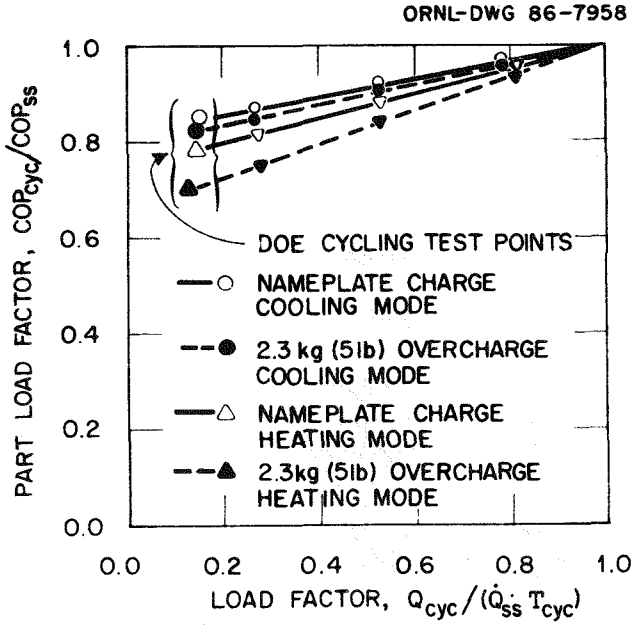

Fig. B.1. Part-load efficiency as affected by refrigerant overcharge.

(Fig. B.1). For the cooling mode tests, conducted according to DOE test procedures, the additional charge of 2.3 kg (5 lb) degraded cycling efficiency by 2.4% of PLF.

The degradation coefficients (C_D) for these cycling tests, conducted according to DOE test procedure, are listed in Table B.1. The additional charge of 2.3 kg (5 lb) caused a 10% increase in C_D for cooling mode tests and a 34% increase in C_D for heating mode tests. The cycling efficiency is degraded for both heating and cooling mode operation since the heat pump operating with 5.7 kg (12.5 lb) charge has more refrigerant circulating through the system and therefore requires more time to establish proper charge distribution at start-up. In Fig. B.2 the scaled capacity for the test heat pump operating with nameplate charge achieves steady state cooling capacity in roughly 4 min, the point at which the accumulator was visually observed purged of refrigerant. However, at the larger operating charge of 5.7 kg (12.5 lb), cooling mode steady state capacity was not attained until 10 min into compressor operation time. Similar results were also observed for heating mode tests (Fig. B.3). The heat pump operating with nameplate charge reached steady state heating capacity in roughly 4 min; an operating charge of 5.7 kg (12.5 lb) steady state capacity was achieved only after 10 min of operation. These results verify that future cycling research always should be conducted with the manufacturer specified refrigerant charge.

Table B.1. Effect of heat pump refrigerant overcharge on degradation coefficient, C_D

Refrigerant charge, lb (kg)	C_D coefficient[a]	
	Cooling mode	Heating mode
7.5 (3.4)[b]	0.185	0.249
12.5 (5.7)	0.205	0.341

[a]Coefficients calculated from cycling tests conducted according to DOE test procedures.

[b]Heat pump nameplate charge.

The results also indicate a greater degradation of cycling efficiency in heating mode as compared with cooling mode cycling degradation due to overcharging. Observed is a larger migration of refrigerant from condenser to evaporator during the off cycle of the heating mode cycling tests as compared with the cooling mode cycling tests. This migration increase is due to the larger temperature difference observed during heating mode operation. Thus at start-up, less time is required to

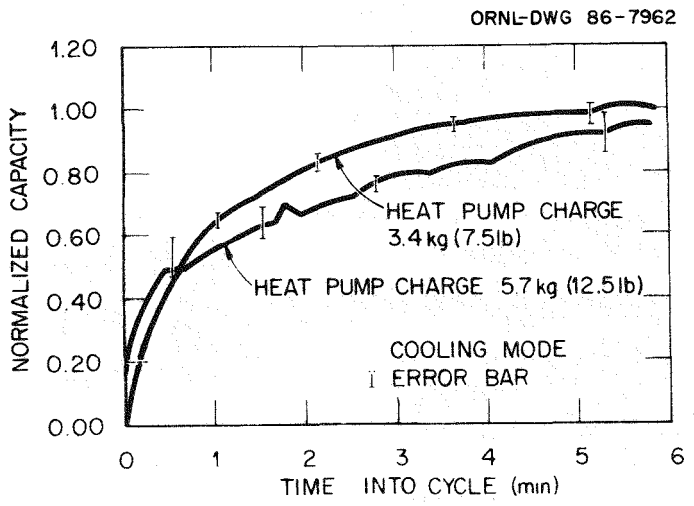

Fig. B.2. Normalized air-side capacity for cooling mode cycling tests conducted according to DOE test procedures.

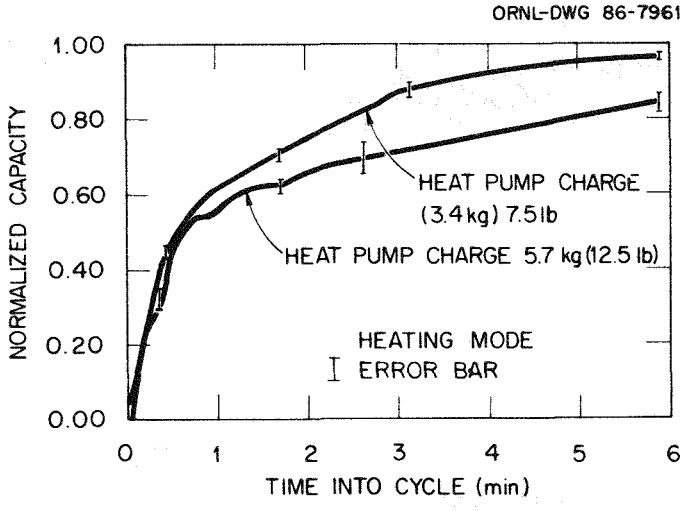

Fig. B.3. Normalized air-side capacity for heating mode cycling tests conducted according to DOE test procedures.

establish proper charge distribution in the cooling mode, because the condenser initially holds 16% of the total charge; in heating mode the condenser at start-up contains only 4% of the total refrigerant charge.

The above multipoint data per curve in Fig. B.1 were incorporated in the Seasonal Performance code to determine the seasonal effect of cycling when the heat pump was overcharged due to added liquid-line length. Performance data for the test heat pump operating with a demand defrost control were applied to loads for an 167-m^2 (1800-ft^2) ranch

style house, using weather data for Knoxville, Tennessee. Seasonal analysis results indicated that overcharging the test heat pump by 2.3 kg (5 lb) caused a 7% increase in the total annual heat pump operating energy. The heating seasonal performance factor degraded from 1.90 to 1.81 due to the additional refrigerant charge, while the seasonal energy efficiency ratio was degraded from 7.40 to 6.70. These seasonal results indicate that split system heat pumps should be installed with no more than the manufacturer minimum specified lengths of liquid and vapor lines, if possible. Otherwise the increase of refrigerant charge will cause increased cycling losses and thereby degrade annual performance of the heat pump.

Appendix C

INTEGRATED AVERAGE COPs AND CAPACITIES FOR FROST-DEFROST-RECOVERY TESTS

Appendix C

INTEGRATED AVERAGE COPs AND CAPACITIES FOR FROST-DEFROST-RECOVERY TESTS

The integrated averages of COP and capacity over the frosting, defrosting, and recovery intervals are listed in Tables C.1 through C.6 as a function of outdoor air temperature, relative humidity, and defrost control. The times of frosting and defrosting periods and the recovery time required for the heat pump to achieve 95% of steady state capacity are also included. The degradation in capacity due to frosting, reverse cycle defrosting, and recovery were calculated as follows:

$$\eta_1 = \left[1.0 - \frac{(\dot{Q}_i)(1_i)}{(\dot{Q}_{ss})(1_i)} \right] 100.0 \ ,$$

where

η_1 = % degration of capacity due to respective portion of a frost defrost, recovery test;

$\dot{Q}_i$ = integrated average capacity over inteval 1_i;

$\dot{Q}_{ss}$ = steady state capacity; and

1_i = time of respective frost, defrost, and recovery intervals.

The degradation in COP due to frosting, reverse, cycle defrost with and without 5-kW auxiliary heat and recovery were calculated as follows:

$$\eta_2 = \left[\frac{\dot{Q}_{ss} \sum_{i=1}^{n} (1_i) - \sum_{i=1}^{n} \dot{Q}_i \, 1_i}{\dot{W}_{ss} \sum_{i=1}^{n} (1_i) - \sum_{i=1}^{n} \dot{W}_i 1_i} \Big/ COP_{ss} \right] 100.0 \ ,$$

Table C.1. Integrated average capacity over frost-defrost-recovery tests for outdoor relative humidity of 60%

Outdoor temp. (°F)	Defrost control	$\dot{Q}_{ss}$ (Btu/h)	Frost		Defrost		Recovery		Δ Capacity (%)			
			Capacity (Btu/h)	Time (min)	Capacity (Btu/h)	Time (min)	Capacity (Btu/h)	Time (min)	Frost	Defrost	Recovery	Total
40	Demand	31616.9	31064.5	202.8	-5887.2	8.3	1750.6	5.8	1.63	4.55	1.19	7.37
40	90 min	31616.9	31745.4	81.4	-5991.4	3.5	19652.6	3.5	-0.35	4.71	1.54	5.90
40	45 min	31616.9	31698.8	37.0	-7339.5	4.0	19173.2	3.8	-0.31	11.02	3.31	14.02
35	Demand	29288.1	28988.0	76.2	-6346.8	7.3	15645.0	4.8	0.88	10.06	2.57	13.51
35	90 min	29288.1	29192.6	81.4	-6273.8	4.8	17646.7	4.5	0.31	6.37	2.01	8.69
35	45 min	29288.1	28985.0	37.0	-5064.0	4.5	17463.0	4.0	0.75	11.60	3.63	15.98
25	Demand	23949.5	23842.0	81.5	-10440.0	7.0	10929.6	2.5	0.40	11.05	1.49	12.94
25	90 min	23949.5	23910.0	86.6	-8127.0	6.0	13236.4	3.3	0.16	8.38	1.53	10.07
25	45 min	23949.5	23583.9	37.0	-8265.0	6.0	13189.1	3.3	1.16	17.45	3.17	21.78

Table C.2. Integrated average COP over frost-defrost-recovery tests for outdoor relative humidity of 60%

Outdoor temp. (°F)	Defrost control	COPss	COP				COP (%)				
			Frost	Defrost cooling	Defrost with I^2R heat	Recovery	Frost	FR/DEF	FR/DEF with I^2R heat	FR/DEF/REC	Total
40	Demand	2.854	2.847	0.770	0.454	1.642	0.245	3.538	3.574	.876	8.234
40	90 min	2.854	2.872	0.683	0.429	1.777	-0.645	4.108	3.711	1.149	8.323
40	45 min	2.854	2.886	0.829	0.375	1.784	-1.108	10.434	7.443	1.538	18.307
35	Demand	2.735	2.688	0.811	0.432	1.462	1.718	8.336	6.644	1.426	18.124
35	90 min	2.735	2.742	0.760	0.422	1.671	-0.262	5.597	4.770	1.323	11.428
35	45 min	2.735	2.731	0.632	0.479	1.640	0.134	10.35	8.044	1.672	20.20
25	Demand	2.379	2.377	1.303	0.266	1.037	0.084	9.962	5.769	1.051	16.87
25	90 min	2.379	2.392	1.051	0.360	1.296	-0.531	7.361	5.160	1.078	13.068
25	45 min	2.379	2.376	1.077	0.356	1.291	0.086	16.183	8.281	1.302	25.852

Table C.3. Integrated average capacity over frost-defrost-recovery tests for outdoor relative humidity of 70%

Outdoor temp. (°F)	Defrost control	$\dot{Q}_{ss}$ (Btu/h)	Frost		Defrost		Recovery		Δ Capacity (%)			
			Capacity (Btu/h)	Time (min)	Capacity (Btu/h)	Time (min)	Capacity (Btu/h)	Time (min)	Frost	Defrost	Recovery	Total
40	Demand	31616.9	31748.0	121.9	-9711.0	8.0	19994.3	4.6	-0.38	7.78	1.26	8.66
40	90 min	31616.9	32404.9	81.5	-8422.9	6.3	18596.0	4.5	-2.20	8.64	2.01	8.45
40	45 min	31616.9	32167.2	41.0	-6138.8	4.8	14042.0	3.0	-1.46	11.75	3.42	13.71
35	Demand	29288.1	28987.6	111.7	-9189.4	7.0	18984.2	5.2	0.93	7.42	1.48	9.83
35	90 min	29288.1	29191.9	81.5	-7234.5	7.3	16773.8	5.5	0.28	9.65	2.49	12.42
35	45 min	29288.1	29133.4	37.0	-6270.0	5.0	17030.0	4.8	0.42	12.97	4.29	17.68
25	Demand	23949.5	23763.3	76.0	-9900.9	7.0	8337.3	2.2	0.69	11.61	1.68	13.98
25	90 min	23949.5	23852.5	86.3	-11503.6	7.3	13648.8	2.5	0.33	11.25	1.12	12.70
25	45 min	23949.5	24124.5	41.1	-9388.8	5.0	14632.0	3.0	-0.61	14.18	2.38	15.95

Table C.4. Integrated average COP over frost-defrost-recovery tests for outdoor relative humidity of 70%

Outdoor temp. (°F)	Defrost control	COP_{ss}	COP				COP (%)				
			Frost	Defrost cooling	Defrost with I^2R heat	Recovery	Frost	FR/DEF	FR/DEF with I^2R heat	FR/DEF/REC	Total
40	Demand	2.854	2.847	1.240	0.295	1.825	0.245	6.306	5.115	0.771	12.437
40	90 min	2.854	2.928	1.000	0.341	1.712	-2.593	7.638	6.090	1.261	12.396
40	45 min	2.854	2.936	0.720	0.423	1.305	-2.873	10.722	8.195	2.032	18.076
35	Demand	2.735	2.683	1.152	0.315	1.777	1.901	6.215	4.767	0.876	13.759
35	90 min	2.735	2.721	0.908	0.395	1.595	0.512	8.299	6.472	1.353	16.636
35	45 min	2.735	2.710	0.749	0.424	1.622	0.914	12.030	8.227	1.718	22.889
25	Demand	2.379	2.358	1.261	0.288	0.805	0.883	10.172	5.964	1.177	18.196
25	90 min	2.379	2.297	1.404	0.223	1.222	4.203	9.752	5.167	0.757	19.879
25	45 min	2.379	2.291	1.110	0.301	1.328	3.699	12.736	6.347	1.135	23.917

Table C.5. Integrated average capacity over frost-defrost-recovery tests for outdoor relative humidity of 80%

Outdoor temp. (°F)	Defrost control	$\dot{Q}_{ss}$ (Btu/h)	Frost		Defrost		Recovery		Δ Capacity (%)			
			Capacity (Btu/h)	Time (min)	Capacity (Btu/h)	Time (min)	Capacity (Btu/h)	Time (min)	Frost	Defrost	Recovery	Total
40	Demand	31616.9	-	-		0.0	-	0.0	0.000	0.000	0.000	0.000
40	90 min	31616.9	34375.8	86.6	-7281.4	2.8	19230.0	3.0	-8.18	3.37	1.27	-3.18
40	45 min	31616.9	33996.8	41.3	-7249.3	2.8	19366.0	3.0	-6.64	7.21	2.55	3.12
35	Demand	29288.1	29328.3	41.2	-6360.9	6.7	16032.0	5.0	-0.11	15.42	4.28	19.59
35	90 min	29288.1										
35	45 min	29288.1	30338.4	37.0	-8420.6	6.7	15217.2	2.9	-2.86	18.46	2.95	18.55
25	Demand	23949.5	23814.7	12.5	-8226.9	4.3	11179.4	3.1	0.35	29.03	8.31	37.69
25	90 min	23949.5										
25	45 min	23949.5	24755.3	41.1	-9056.6	7.0	8430.0	2.4	-2.75	19.12	3.02	19.39

Table C.6. Integrated average COP over frost-defrost-recovery tests for outdoor relative humidity of 80%

Outdoor temp. (°F)	Defrost control	COP_{ss}	COP				COP (%)				
			Frost	Defrost cooling	Defrost with I^2R heat	Recovery	Frost	FR/DEF	FR/DEF with I^2R heat	FR/DEF/REC	Total
40	Demand	2.854	-	-	-	-	0.000	0.000	0.000	0.000	0.000
40	90 min	2.854	3.046	0.722	0.353	1.734	-6.723	3.679	3.045	1.191	1.192
40	45 min	2.854	3.002	0.716	0.354	1.755	-5.193	7.440	5.422	1.774	9.443
35	Demand	2.735	2.708	0.798	0.426	1.513	0.987	13.711	9.028	1.649	25.375
35	90 min	2.735									
35	45 min	2.735	2.802	1.074	0.345	1.426	-2.461	16.434	9.928	1.242	25.143
25	Demand	2.379	2.374	1.005	0.345	1.111	0.210	31.147	8.268	1.609	41.234
25	90 min	2.379									
25	45 min	2.379	2.464	1.1170	0.318	0.825	-3.559	18.183	8.786	1.673	25.083

where

η_2 = % degradation of COP over the frosting, defrost, and recovery portion of a frost, defrost, recovery test;

$\dot{\omega}_i$ = integrated average heat pump power draw over interval l_i; and

COP_{ss} = steady state COP.

ORNL/CON-253

INTERNAL DISTRIBUTION

1. S. J. Ball
2. V. D. Baxter
3. R. S. Carlsmith
4. F. C. Chen
5. F. A. Creswick
6. P. D. Fairchild
7. S. K. Fischer
8. M. A. Kuliasha
9. H. A. McLain
10. V. C. Mei
11-61. W. A. Miller
62. J. C. Moyers
63. D. E. Reichle
64. C. K. Rice
65. H. Perez-Blanco
66. R. E. Saylor
67. R. B. Shelton
68. T. J. Simmons
69. T. K. Stovall
70. Central Research Library
71. Document Reference Section
72-73. Laboratory Records
74. Laboratory Records-RC

EXTERNAL DISTRIBUTION

75. John J. Cuttica, Vice President of Research and Development, Gas Research Institute, 8600 W. Bryn Mawr Avenue, Chicago, Illinois 60631
76. Joseph P. Kult, Harvard University, 79 J. F. Kennedy St., Cambridge, MA 02138
77. Denton E. Morrison, Michigan State University, 201 Berkey Hall, East Lansing, MI 48824-111
78. Richard L. Perrine, Engineering and Applied Sciences, Civil Engineering Department, Engineering I, Room 2066, University of California, Los Angeles, California 90024-1593
79. John D. Ryan, U.S. Department of Energy, CE-132, FORSTL, GF-217, 1000 Independence Ave., SW, Washington DC 20585
80. Terry Statt, U.S. Department of Energy, CE-132 FORSTL GF-217, 1000 Independence Ave., SW, Washington, DC 20585
81. Office of the Assistant Manager for Energy R&D, DOE-ORO, P.O. Box 2001, Oak Ridge, Tennessee 37831-8600
82-91. OSTI, U.S. Department of Energy, P.O. Box 62, Oak Ridge, Tennessee 37831

☆U.S. GOVERNMENT PRINTING OFFICE 1989--648-119/00061